Journal of the Korean Physical Society, Vol. 73, No. 6, September 2018, pp. 747∼792 Review Articles

Mesoscopic Transport Events and the Breakdown of Fick's Law for Turbulent Fluxes

T. S. Hahm*
Department of Nuclear Engineering, Seoul National University, Seoul 08826, Korea

P. H. Diamond
Center for Astrophysics and Space Science, University of California San Diego, San Diego 92093, USA and Center for Fusion Sciences, Southwestern Institute of Physics, Chengdu 610041, China

(Received 3 August 2018)

This paper presents a pedagogical review of the physics of mesoscopic transport events and their role in the breakdown of Fick's Law for turbulent transport in magnetically confined plasma. It is now clear that the conventional picture of localized turbulence and quasi-linear calculation of fluxes fails to address and account for the phenomenology of tokamak transport. One key issue is the observed departure from the expected gyro-Bohm transport scaling. The causes of this breakdown of Fickian thinking include turbulent avalanching and pulse propagation (turbulence spreading). Both are mesoscopic transport events, and both tend to de-localize the flux–gradient relation. Turbulence spreading is the process of self-scattering and expansion of a slug or other local exciton of turbulence. Spreading is described by theoretically-motivated, phenomenological reaction–diffusion models for the turbulence activity (intensity) field, much in the spirit of Ginzburg–Landau theory. Such models imply that spreading will occur by propagation of intensity fronts. After discussing the basic theory, this paper presents several critical tests of turbulence spreading models using gyrokinetic simulation. Applications include rho-star scaling, penetration of transport barriers and core-edge coupling. Relevant experiment–theory comparisons are addressed, as well. Avalanching refers to a process whereby correlated topplings of nearby localized cells overturn sequentially and drive a burst of transport. Avalanching is a process intrinsic to systems that support a broad range of scales l between a cell size Δ and system size L, *i.e.* $\Delta < l < L$. Avalanching is also a natural way to produce transport events on scales that exceed the cell size or correlation length. Therefore, the PDF (probability distribution function) of avalanches as a function of l is a crucial quantity, necessary for predicting confinement in a system like ITER, with a very large-scale separation between L and Δ. Avalanching emerged from the theory of self-organized criticality but is a more general phenomenon. The paper traces the intellectual prehistory of avalanching through the advent of self-organized criticality. Special focus is devoted to reduced continuum models of avalanching. The physics of avalanching in confined plasma is discussed in detail, via several multi-faceted comparisons to flux-driven fluid and gyrokinetic simulations. The dominance of bursty, large transport events in the flux is identified. Evidence for avalanching in basic and confinement experiments is summarized. The paper concludes with sections on selected special topics, a discussion of the relation between turbulence spreading and avalanching, and a list of possible future directions. Throughout the paper, an effort is made to set fusion theory and phenomenology in the context of ideas discussed in the broader scientific community.

PACS numbers: 52.25.Fi, 52.30.Gz, 52.35.Mw, 52.35.Ra, 05.40.Fb, 05.65.+b
Keywords: Self-organization, Turbulence spreading, Avalanches, Entrainment, Mesoscopic transport, Intermittency, Non-local transport, Self-organized criticality, Magnetically confined plasma, Transport events, Fluctuation front propagation
DOI: 10.3938/jkps.73.747

*E-mail: tshahm@snu.ac.kr

CONTENTS

I. INTRODUCTION

"Life always has a fat tail."
- Eugene Fama

"All models are wrong. Some are useful."
- George Box

The quest for fusion energy forces us to confront many challenges. Most prominent of these are how to maintain macroscopic stability and control micro-turbulence along with the non-classical transport it produces. The goals of understanding, predicting and controlling turbulent transport remain important pursuits in the magnetic fusion theory program. The long-standing hope of calculating energy confinement time ($\tau_{\rm E}$) scaling has expanded to include grappling with momentum and particle transport, multi-scale processes involving energetic particles and scrape-off layer(SOL)-core coupling, to name just a few problems. The challenge now is to predict profiles and their evolution. Considerable resources continue to be expended on the pursuit of these topics. Observers from other scientific communities might naturally ask the (*good*) question: 'After more than fifty years, why hasn't the problem been solved? After all, the turbulence in confinement devices is not particularly strong!' A possible answer to this question is that turbulence in confinement devices:

i) is present on a broad range of scales l, where $\rho_i \leq l \leq a$ (at least), even for weak excitation. The physics of mesoscales $\rho_i \ll l < a$ presents a significant challenge! Here, ρ_i is an ion Larmor radius, and a is the system size.

ii) exhibits a rich variety of local and global bifurcations and transition, which are highly dynamic nonlinear phenomena. Most notable of these is the transition from a low to a high confinement regime (L→H transition) [1], leading to the formation of an edge transport barrier and the preferred route to improvement of confinement relative to L-mode.

iii) appears to hover naturally at Kubo number ∼1. Here, Ku $\sim \tilde{v}_\perp \tau_c/\Delta_c$, where $\tilde{v}_\perp$ is a typical fluctuation velocity, and τ_c is a correlation time and Δ_c is the correlation scale. Thus, the system lies somewhere between regimes where stochastic (Ku < 1) and coherent (Ku > 1) approaches are useful.

At the same time, the intellectual foundations of the approach to turbulence and transport in confinement devices remain based upon the thinking of the 1960s and '70s, namely: slowly evolving profiles leading to linear instability that drives local evolution and saturation, all yielding "the answer" as a local, usually quasi-linear, flux in the form of a generalized Fick's Law. In particular, such a Fickian formulation links fluxes to profile gradients by effective transport coefficients, which are, in

Fig. 1. (Color online) Spreading of a turbulent spot.

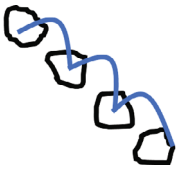

Fig. 2. (Color online) Cartoon of an avalanche.

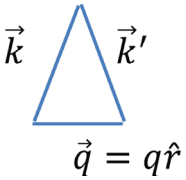

Fig. 3. (Color online) Thin, nearly isosceles triad.

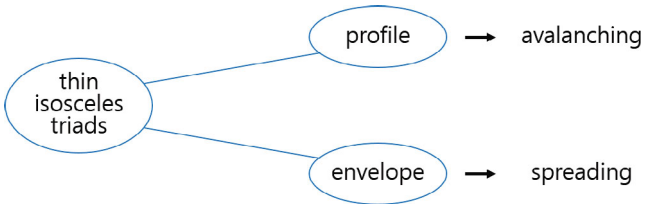

Fig. 4. (Color online) Couplings which result in spreading and avalanching.

turn, also functionals of the local turbulence intensity and gradient. Such a formulation is attractive to many, on account of intellectual inertia (*i.e.* it is simple and familiar) and its compatibility with easy-to-use transport analysis tools used in data interpretation. However, this approach not only 'bewitches the intelligence of the physicist by the means of data analysis' (after L. Wittgenstein, *Philosophical Investigations* (1953)), it also is simply *wrong*, as discussed herein.

In this paper, we present a short review of the physics underlying the breakdown of Fick's law for turbulent transport in magnetically confined plasmas. The focus is on nonlinear patterns arising from dynamics on mesoscales, which emerge from spatially inhomogeneous nonlinear interactions. The pattern formation processes discussed are:

i) *Turbulence spreading*, or entrainment, whereby nonlinear coupling of fluctuation energy redistributes the turbulence intensity field away from the regions where it is excited, usually by linear growth. The key point is that mesoscopic inhomogeneity of the fluctuation envelope (scales l such that $\rho_i < l < a$) produces a flux of turbulence energy. The prototypical turbulence spreading problem is that of calculating the spatio-temporal evolution of a turbulent slug or spot (Fig. 1). This includes the well-known problem posed by Loitsyansky [2]. Turbulence spreading lends itself to description by reaction–diffusion models, from which hybrid (*i.e.* mesoscopic) space–time scales naturally emerge.

ii) *Avalanching*, whereby transport events are formed by the correlated, sequential overturning or firing of localized cells or modes (Fig. 2). Transport due to avalanching is intrinsically "concentrated" in limited parts of the probability measure and yields a flux probability distribution function that has a fat tail. The fat tail of interest is a power law (self-similarity!). A high Kurtosis of the PDF is one possible symptom of a fat tail. The prototypical avalanching system is that of the sandpile, with local-gradient-dependent toppling rules and a clear disparity between the scale of an individual cell ($\sim$ few ρ_i), the scale of avalanche ($\sim l$) and the system size ($\sim a$). Once again, the inequality $\rho_i < l < a$ appears! Avalanching lends itself to description by nonlinear fronts and dissipative structures, like turbulent bores.

Not surprisingly, the two processes of turbulence spreading and avalanching are closely related, though conceptually distinct. In reality, the two processes interact and work together, because both result from *nonlinear* radial propagation of excitation. Indeed, both result from three-mode/triad interactions, in which one leg of the triad is mesoscopic (Fig. 3). For turbulence spreading, coupling occurs via the turbulence intensity field and works by spatial scattering due to nonlinear interaction. The mesoscopic leg of the triad reflects the envelope scale. Most models of spreading involve nonlinear intensity diffusion, familiar from $K-\epsilon$ models of turbulence. For avalanching, coupling occurs via the mean gradient and works by overturning of neighboring cells. The mesoscopic leg of the triad reflects a profile corrugation. The simplest avalanche model is a generalized Burgers equation, where shocks correspond to avalanches. The fact that spreading and avalanching both emerge from thin, nearly isosceles triads suggests that the two processes are deeply interconnected and inseparable (Fig. 4). Finally, we note here that the critical role of mesoscopics is already appreciated as a consequence of the important role of zonal flows in the self-regulation of drift wave turbulence [3]. Spreading and avalanching are a step beyond the zonal flow, in that these mesoscopic excitations enhance, rather than regulate, transport and are directly linked to the spatio-temporal propagation of turbulence energy.

Of course, we must face the two questions of:

i) Why is this topic important — especially to magnetic fusion?

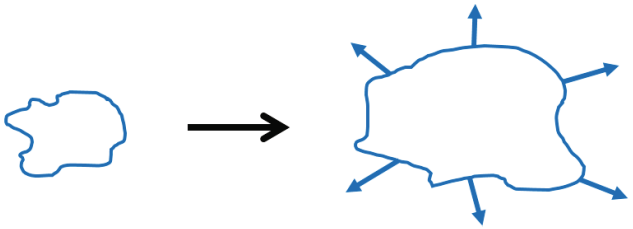

Fig. 5. (Color online) Spreading of turbulent spot.

ii) Why is it interesting — especially to physicists, mathematicians and engineers concerned with the science and technology of pattern formation?

Regarding the first question, spreading and avalanching are central to understanding the origins of the breaking of gyro-Bohm scaling. Recall that in drift wave turbulence, a mixing length estimate of the effective diffusivity is $D \sim v_* l$, where v_* is the diamagnetic velocity and l is characteristic scale. As $\rho_i < l < a$, one might expect D to range from $D \sim v_* \rho_i \sim (\rho_i/a)\rho_i v_{Ti}$ for gyro-Bohm, to $v_* a \sim \rho_i v_{Ti} \sim D_{\rm B}$ for Bohm. Estimates of the mixing length based on mode structure point to $l \sim \rho_i$ so $D \sim \rho_* D_{\rm B}$, where $\rho_* = \rho_i/a$. However, experiments generally indicate $D \sim \rho_*^\alpha D_{\rm B}$, with $\alpha < 1$ ($\alpha \sim 0.6{-}0.7$), which suggests that gyro-Bohm scaling is broken. This finding poses a challenging question: How does an ensemble of fluctuations with $\Delta \sim$ few ρ_i manage to produce transport with an effective mixing length $l_x \sim \rho_i^\alpha a^{1-\alpha}$, with $\alpha < 1$? A natural candidate for the breakdown of gyro-Bohm scaling is the formation of intermittent mesoscale transport events, either by spreading or avalanching or both. Such bursty collective excitations are formed by brief interactions among the underlying fluctuations. Understanding the breakdown of gyro-Bohm scaling is critical to the successful prediction of confinement and performance.

Mesoscopic transport events play a role in limiting the effectiveness of transport barriers (TBs). Such barriers include ITBs (internal TB), ETBs (edge TB) and magnetic islands. ITBs offer a route to improved performance. However, penetration of turbulence and avalanches through ITBs is predicted and observed, suggesting that mesoscopic processes may limit their effectiveness. Likewise, magnetic islands associated with neoclassical tearing modes (NTM) impose significant constraints on tokamak plasma energy content. As NTM evolution is determined by the multi-scale interaction of turbulent transport and MHD dynamics, it's not surprising that turbulence spreading through the island is an important issue. Similarly, turbulence spreading from the SOL into the pedestal has been suggested [4] as a player in the H→L back transition.

We hasten to add that mesoscopic transport events are intrinsically interesting, as well as important to the fusion program. One of the classic fundamental problems in turbulence is that of describing the spreading of a turbulent spot [5] (Fig. 5). Indeed, this problem is arguably the spatial counterpart of the Kolmogorov cascade problem but describes spatial evolution on envelope scales, as well as local cascading to dissipation. The Loitsyansky problem [2,6,7] of how the energy of a slug of turbulent fluid decays is closely related. Yves Pomeau [8,9] and others have pioneered the use of reaction–diffusion models to describe the subcritical onset of turbulent flow in a pipe as a process in which localized slugs of turbulence grow, spread and ultimately overlap, leading to global transition. This work is an excellent example of the use of the reaction–diffusion model approach to spatially complex turbulence problems. Similarly, the concept of the avalanche is ubiquitous in the theory of complex systems, particularly in self-organized criticality. Bores, traffic jams and flood waves all have much in common with avalanches [10]. Indeed, we view the avalanche as the concrete realization of the more general idea of an intermittent, propagating front. This is an important class of dissipative structures, and the study of avalanches in fusion plasmas has much to offer the broader scientific community.

In this paper, we review the theory of mesoscopic transport events, and focus on turbulence spreading and avalanching. We give an overview of the basic reaction–diffusion modelling of spreading, with emphasis on the physics of intensity front formation and propagation. The implications of spreading for interpreting key simulations are discussed. Special emphasis is devoted to the implications of spreading for ρ_* scalings, for the permeability of transport barriers and for the effect of NTM-generated magnetic islands on turbulence. We review the origin of the concept of an avalanche by tracing the development of the theory of self-organized criticality and place the avalanche as an intermittent excitation, which emerges in interaction-dominated systems. Special emphasis is devoted to continuum models of avalanching dynamics. We then give a thorough discussion of avalanching and profile self-organization in confined plasmas, primarily from the perspective of simulations. Basic features of avalanches are discussed, as are the statistics of transport events and the Hurst exponent. We present an overview of the evidence for avalanching in experiments. The review concludes with descriptions of advanced topics and open questions for further discussion. There, we focus on the interaction of spreading and avalanching, and on the microphysics of the avalanche process.

The organization of this paper follows the detailed table of contents.

II. TURBULENCE SPREADING

1. Introduction to turbulence spreading

As mentioned before, bulk of transport research in magnetic fusion energy (MFE) community still relies on

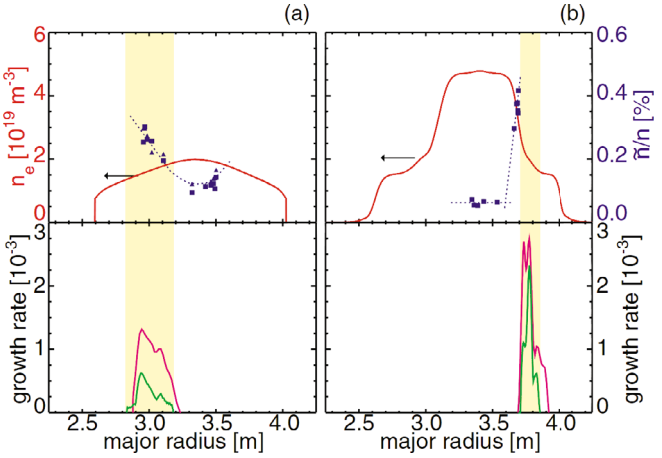

Fig. 6. (Color online) Inferred density fluctuation level (blue) and the plasma density profile (red) in the target plasma (a) and in the internal transport barrier plasma (b) compared to the calculated linear growth rate (bottom) using the comprehensive kinetic stability code FULL without rotation (purple) and with rotation (green). The calculated linear growth rate is only plotted in the region where there are reflectometer measurements. (Reproduced with permission from Ref. [12]. Copyright 2005 by the American Physical Society.)

the local theory paradigm at a conceptual level. The local gradient (in radius) acts as an expansion-free energy source for linear instabilities, which grow in time until nonlinearly saturated, locally. Therefore the resulting turbulent transport depends on the local gradients and can be described by a generalized Fick's law with effective transport coefficients. However, evidence from experiments and simulations has been accumulating that cannot be understood in the context of the local theory. Plasma transport is often found to significantly exceed the level expected from neoclassical theory based on Coulomb collisions in the region of very weak gradients, where linear modes are estimated to be stable [11]. One can speculate as to why turbulence exists in that region (despite local linear stability) and contributes to anomalous transport. Indeed, non-zero fluctuations and anomalous transport have been observed in the linearly stable region of JT-60U reversed shear plasma, as shown in Fig. 6 [12]. In addition, strong turbulence exists in the scrape-off-layer (SOL) region where the radial gradients of profiles are very weak. Aforementioned examples all indicate serious limitations of a turbulent transport model based solely on local linear stability. Furthermore, comparisons between local nonlinear simulations and experimental measurements have indicated that the simulations considerably under-predict the turbulence and transport level at minor around $0.8 \leq r/a \leq 0.9$. This is called the short-fall problem in no man's land.

These issues all indicate that the local plasma transport level cannot always be accounted for by the local excitation rate of turbulence and quasilinear approaches. Therefore, it is quite natural to consider the possibility that turbulence at one radial region can spread into another region with weaker linear excitation. Although the theoretical possibility of radial propagation of turbulence in tokamaks has been investigated since at least 1994 [13], the majority of transport modeling activity in MFE to date is still based on local models. In this section, we describe simple theories, nonlinear simulations (mostly gyrokinetic) and MFE-relevant applications of turbulence spreading. For simplicity, we focus on turbulence spreading and fluctuation front propagation only, without considering profile evolution and avalanches in this section. These are discussed in Sec. III.

2. Simple nonlinear model of turbulence spreading

In this section, we study the simplest, nontrivial model of turbulence spreading that evolves the intensity field on mesoscales. This reaction-nonlinear diffusion model describes the spatio-temporal propagation of a patch of turbulence from a region where it is locally excited to a region of weaker excitation or even local damping. A single model equation for the local turbulence intensity, $I(x,t)$, which includes the effects of local linear growth and damping, spatially local nonlinear coupling to dissipation and spatial scattering of turbulence energy induced by nonlinear coupling is [14]:

$$\frac{\partial I}{\partial t} = \frac{\partial}{\partial x}\chi(I)\frac{\partial I}{\partial x} + \gamma(x)I - \alpha I^{1+\beta}. \quad (1)$$

The terms on the right-hand side correspond to nonlinear spatial scattering [*i.e.* typically $\chi(I) \sim \chi_0 I^\beta$, where $\beta = 1$ for weak turbulence and $\beta = 1/2$ for strong turbulence], linear growth and damping and local nonlinear decay, respectively. Here α is a nonlinear coupling coefficient. Note that α and χ_0 can be functions of radius. The local nonlinear decay term can lead to a saturation of I via coupling to smaller scales due to local mixing in x. By modifying γ and introducing another field, zonal flow and mean E × B flow shear effects may be introduced. For $\beta = 1$, the local saturation level $I(x) \simeq (\gamma(x)/\alpha)^{1/\beta}$ corresponds to the time-honored "mixing length rule".

The crucial nonlinear effect of spatial scattering is captured in the nonlinear diffusion term (the first term on the RHS). This term appears naturally if one treats the nonlinear coupling in $\mathbf{k}$ space and nonlinear scattering in x on an equal footing by using a multi-scale closure of the E × B nonlinearity, which treats both mode ($\mathbf{k}$) and envelope scales, *i.e.* $\boldsymbol{\nabla} \to i\mathbf{k} + \partial_x$, so that [15]:

$$\sum_{\mathbf{k}'}(\mathbf{k}\cdot\mathbf{k}'\times\mathbf{b})^2 R_{\mathbf{k},\mathbf{k}'} I_{\mathbf{k}'} I_{\mathbf{k}} \to -\frac{\partial}{\partial x} D_x \frac{\partial}{\partial x} I_{\mathbf{k}} + k_\perp^2 D_{\mathbf{k}} I_{\mathbf{k}}. \quad (2)$$

Here, $R_{\mathbf{k},\mathbf{k}'}$ is a resonance function determining the effective correlation time, $D_x = \sum_{\mathbf{k}'} R_{\mathbf{k},\mathbf{k}'} |\delta \mathbf{v}_{\mathrm{E},\mathbf{k}'}|^2$ and $D_{\mathbf{k}} = \sum_{\mathbf{k}'} (\mathbf{k}\cdot\mathbf{k}'\times\hat{\mathbf{z}})^2 R_{\mathbf{k},\mathbf{k}'} |\delta \mathbf{v}_{\mathrm{E}\mathbf{k}'}|^2$.

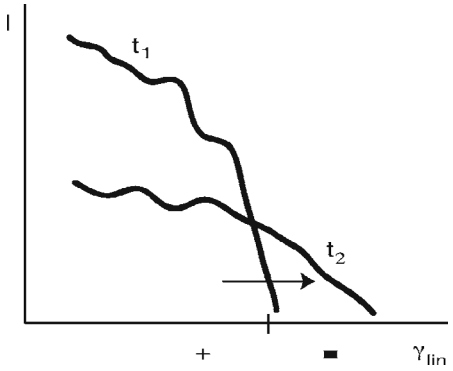

Fig. 7. A cartoon illustrating that the integrated fluctuation intensity in a region of extent $2\Delta x$ about a point x [*i.e.* $\int_{x-\Delta x}^{x+\Delta x} I(x')dx'$] can grow, *even for negative* $\gamma(x)$, as long as $\chi(I)\partial I/\partial x|_{x-\Delta x}^{x+\Delta x}$ is *sufficiently large*. Alternatively, I can decrease, *even for positive* $\gamma(x)$, should $\chi(I)\partial I/\partial x|_{x-\Delta x}^{x+\Delta x}$ be *sufficiently negative*. (Reproduced with permission from Ref. [22], AIP Publishing.)

This equation can be derived from a Fokker–Planck-type analysis of the evolution of the turbulence intensity field in space (*i.e.* assuming a random walk by intensity, with a step size equal to the turbulence integral scale or correlation length and a time step equal to the correlation time) [16]. For that, the assumption that the second moment of the spreading PDF is finite (*i.e.* $\int(\Delta x)^2 P(\Delta x)d(\Delta x) < \infty$) is required. This may not be the case, especially if $P(\Delta x)$ is a power law. The random walk yields the nonlinear diffusion term, while local evolution is described by the growth and nonlinear decay terms. In this respect, the model equation is similar to a type of $K-\epsilon$ model [17,18] (more accurately, a K model) for the turbulence intensity field. $K-\epsilon$ models are used heavily in subgrid-scale modeling. In addition, this equation can also be derived from an application of quasilinear theory to the wave-kinetic equation, as described in Ref. [16]. Possible extensions of the model include the additional equations for other fields [19] and contributions to dynamics such as zonal flows which feed back on I [20]. Spreading models that incorporate fractional kinetic models of scattering have been discussed in Ref. [21].

Note that the above equation manifests the crucial effect of spatial coupling in the nonlinear diffusion term. This implies that the integrated fluctuation intensity in a region of extent $2\Delta x$ about a point x [*i.e.*, $\int_{x-\Delta x}^{x+\Delta x} I(x')dx'$] can grow, *even for negative* $\gamma(x)$, as long as $\chi(I)\partial I/\partial x|_{x-\Delta x}^{x+\Delta x}$ is *sufficiently large*. Alternatively, I can decrease, *even for positive* $\gamma(x)$, should $\chi(I)\partial I/\partial x|_{x-\Delta x}^{x+\Delta x}$ be *sufficiently negative*. Thus, the *profile* of fluctuation intensity is crucial to its spatiotemporal evolution, as illustrated in Fig. 7. This notion can be further quantified by arguing by analogy to the resistive tearing instability theory [23]. Integrating Eq. (1) in radius as described above, we obtain

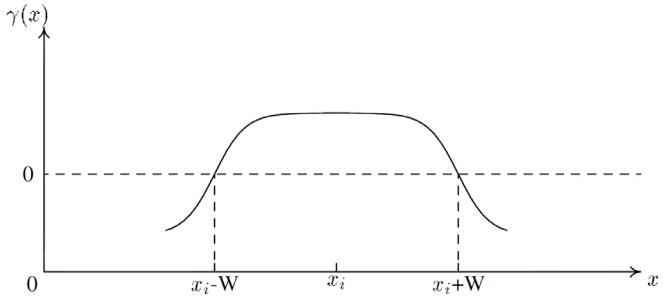

Fig. 8. Local excitation rate, $\gamma(x)$, as a function of radius. (Reproduced with permission from Ref. [14]. Copyright 2004 IOP Publishing.)

$$\frac{\partial}{\partial t}\int_{x-\Delta x}^{x+\Delta x} dx'\, I(x',t) = \Delta'(I)I(x,t) + \int_{x-\Delta x}^{x+\Delta x} dx'\,[\gamma(x')I - \alpha I^{1+\beta}]. \quad (3)$$

Here, $\Delta'(I) \equiv \chi_0(\partial/\partial x)I^\beta|_{x-\Delta x}^{x+\Delta x}$ characterizes the net flux of turbulence [16] into (out of) $[x-\Delta x, x+\Delta x]$ via a net jump in the slope of fluctuation intensity. We recall that the classical tearing mode stability parameter Δ', which characterizes the free energy in the equilibrium current gradient, is defined as a jump in the slope of perturbed flux function across the resistive layer [23]. Equation (3) clearly indicates that the *sign* of Δ' plays a crucial role in the growth of turbulence intensity. Finally, note that even if a region is locally unstable, excitation by spreading can exceed excitation by local instability.

Focusing on the weak turbulence regime with $\beta = 1$ that has been reported by nonlinear gyrokinetic simulations, we first review the local solution. In the absence of the nonlinear radial diffusion, we can integrate Eq. (1) in time with an initial profile $I(x,0) < \gamma(x)/\alpha$ to obtain a solution. In the region $\gamma > 0$, I initially grows exponentially with a linear growth rate $\gamma(x)$ and then saturates at a finite level given by $\gamma(x)/\alpha$. However, in the region where $\gamma < 0$, this local solution predicts that the fluctuation vanishes ($I \to 0$).

A. Turbulence spreading into the linearly stable zone

Now, we study in detail how the nonlinear diffusion term in Eq. (1) allows fluctuations to spread into a zone where $\gamma < 0$. In the region where $\gamma(x) < 0$, it is expected that $I \ll 1$. Then, the last two terms on the right-hand side become subdominant. Equation (1) simplifies to the following nonlinear partial differential equation, which is also known as the modified porous medium equation [5]. The key element here is diffusion proportional to the field

being diffused. This system supports finite speed *fronts*.

$$\frac{\partial}{\partial t} I_0 = \frac{\partial}{\partial x}\left(\chi_0 I_0 \frac{\partial}{\partial x} I_0\right). \tag{4}$$

We consider a smooth radially varying linear excitation rate profile $\gamma(x)$. As shown in Fig. 8, $\gamma > 0$ in the middle for $|x - x_i| < W$, and x_i is the position where $\gamma(x)$ is maximum.

Then, γ decreases monotonically towards the axis and the edge, becoming 0 at $x = x_i - W$ and at $x = x_i + W$, and negative for $|x - x_i| > W$. In this section, we consider the case where the background pressure and $\gamma(x)$ do not change in time. This is an oversimplification, but it makes comparisons with the fixed gradient gyrokinetic simulations easier [24, 25]. Furthermore, it illustrates the point that turbulence spreading is not an artefect of global simulations, as originally argued by some local simulation practitioners. For more challenging problems such as the formation of transport barriers, where the disparity in timescales becomes less obvious, one needs to extend the theory to a multifield nonlinear system [18, 26–29], in which evolutions of $\mathbf{E} \times \mathbf{B}$ flows and the pressure gradient are included [30]. This will be discussed in Sec. III and IV. For an initial profile of I_0,

$$I_0(x, 0) = \frac{\epsilon}{W}\left(1 - \frac{(x - x_i)^2}{W^2}\right) H(W - |x - x_i|),$$

Eq. (4) has an exact solution [5]:

$$I_0(x, t) = \frac{\epsilon}{(6\epsilon\chi_0 t + W^3)^{1/3}}\left(1 - \frac{(x - x_i)^2}{(6\epsilon\chi_0 t + W^3)^{2/3}}\right) \times H\left((6\epsilon\chi_0 t + W^3)^{1/3} - |x - x_i|\right), \tag{5}$$

where ϵ is the volume-integrated intensity, H is a Heaviside function. Equation (5) shows that in the absence of linear or nonlinear damping (the second term and the third term on the right-hand side of Eq. (1)), a fluctuation front at $x = x_i + (W^3 + 6\epsilon\chi_0 t)^{1/3}$ will propagate beyond $x_0 \equiv x_i + W$ indefinitely. (The same comment applies to another front at $x = x_i - W$, which propagates to the left.)

We note that the short time behaviour of propagation can be characterized by $(x - x_0)_{\rm front} \sim U_x t$ after expanding in $(x - x_0)_{\rm front}/W$, with $U_x = 2\epsilon\chi_0/W^2$. This apparent ballistic behaviour in the short term is mainly a consequence of the fact that $\Delta x \ll W$. It is not difficult to derive from other theoretical considerations. It is obvious that the expression for U_x from the nonlinear diffusion theory described here is qualitatively different from the radial group velocity of a drift wave. This is one of the signatures that distinguishes the nonlinear diffusion theory from the other models, which heavily rely on the specific properties of the linear drift wave dispersion relation [13] or on nonlinear enhancement of dispersion [31] in the four-mode system consisting of drift wave eigenmodes and zonal flows [32]. Theories of spreading involving coupling to zonal flows must include the additional channel for energy loss introduced by zonal flow damping. The fluctuation front ultimately ceases to propagate if the fluctuation energy flux due to radial propagation into the linearly stable zone is balanced by dissipation (Fig. 9). First, we consider the case where the linear damping near the propagation front ($\gamma(x) \simeq -|\gamma'|(x - x_0)$) is strong enough to play a dominant role in limiting the radial spreading. The scaling for Δx can be obtained by balancing the time required for linearly damping the fluctuation at $x = x_0 + \Delta x$, *i.e.*, $T_{\rm damp} \sim 1/(|\gamma'|\Delta x)$, against the time required for the front to propagate a distance Δx, *i.e.*, $T_{\rm prop} \simeq \Delta x/U_x$. The resulting scaling with respect to the damping rate ($\Delta x \propto |\gamma'|^{-1/2}$) is weaker than that based on a heuristic argument derived from linear toroidal coupling, $\Delta x \propto |\gamma|^{-1}$ [33]. The front stops propagating when the width of spreading, Δx satisfies the condition

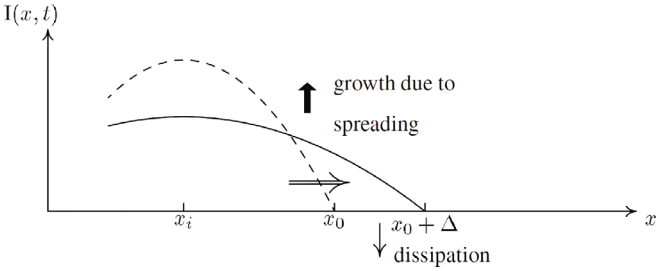

Fig. 9. Fluctuation front ceases to propagate if the fluctuation energy flux due to radial propagation is balanced by dissipation. (Reproduced with permission from Ref. [14]. Copyright 2004 IOP Publishing.)

$$\frac{\partial}{\partial T}\int_{x_0}^{x_0+\Delta x} dx\, I_0(x, T) = -\int_{x_0}^{x_0+\Delta x} dx\, \gamma(x, T) I_0(x, T), \tag{6}$$

which yields the expression for the width or extent of the radial spreading, Δx:

$$\Delta x \simeq 2\sqrt{3}\left(\frac{\epsilon\chi_0}{|\gamma'|}\right)^{1/2}\frac{1}{W}. \tag{7}$$

As expected, higher fluctuation intensity in a linearly unstable zone (ϵ) enhances the radial spreading, while strong linear damping reduces it. As discussed before [14], simple relations $\gamma \sim \Delta'(I)/\Delta x$ and $\gamma_{\rm prop} \sim U_x/\Delta x$ elucidate the physical meaning of $\Delta'(I)$ as a measure of influx of turbulence intensity into a radial layer of width $2\Delta x$. It is also instructive to note again the similarity with tearing mode theory, which predicts $\gamma \propto \eta^{3/5}\Delta'^{4/5}$ and the resistive layer width $\Delta x \propto \eta^{2/5}\Delta'^{1/5}$, which satisfies $\gamma \propto \Delta'\eta/\Delta x$. The magnetic flux is destroyed across the resistive layer at a rate proportional to $\eta\Delta'$.

A familiar example of a characteristic scale that is determined by a similar consideration is the Kolmogorov

dissipation scale in fluid turbulence. The energy transfer rate of an eddy with a size "l" in the inertial range toward higher-k region due to nonlinear interaction is given by the eddy turn-over rate, which scales as $\epsilon^{1/3}/l^{2/3}$, where "ϵ" is the energy input rate. On the other hand, the energy drain at the high-k region due to the viscous dissipation occurs at a rate "ν/l^2". By balancing these two rates, the Kolmogorov dissipation scale is obtained:

$$k_{\rm d} \sim l_{\rm d}^{-1} \sim (\epsilon/\nu^3)^{1/4}. \tag{8}$$

We recall $\Delta x \sim (\epsilon/|\gamma'|)^{1/2}$ from Eq. (7). This shows that the inertial range extends down to "$k_{\rm d}$" and its fractional power depends on the energy input rate ϵ and the dissipation ν are similar to those in Eq. (7), although the values are not identical. Of course, Δx measures spreading penetration in space, while $k_{\rm d}$ measures spreading in scale.

These simple observations in this subsection nicely illustrate the failure of the conventional local saturation paradigm [34], and strongly support the argument that propagation of turbulence is a crucial, fundamental problem in understanding confinement scalings for fusion devices in which growth and damping rate profiles vary rapidly in space. This conclusion remains valid when profile evolution is allowed in simulations, as will be discussed in Sec. III.2.

B. Turbulence front propagation in the linearly unstable zone

It is also of practical interest to know how a patch of turbulence propagates radially after local nonlinear saturation. We can make analytic progress by considering the profiles of $\gamma(x)$, $\alpha(x)$, and $\chi_0(x)$, which are constant in radius. Equation (1) for $\beta = 1$ is obviously a variant of the well-known Fisher–KPP (Kolmogoroff–Petrovsky–Piscounoff) equation for logistic-limited epidemic propagation [35,36], with nonlinear diffusion when $\gamma > 0$. It is a subclass of a reaction–diffusion-type equation that has the following form in one-dimension.

$$\frac{\partial}{\partial t}C(x,t) = R(C(x,t)) + D\frac{\partial^2}{\partial x^2}C(x,t), \tag{9}$$

Here, C is the concentration field, and R is the reaction rate. It is well known that the Fisher–KPP equation exhibits a *ballistically propagating front* solution.

After non-dimensionalizing Eq. (1) by $x \to (\alpha/2\chi_0)^{1/2}x$, $t \to \gamma t$ and $I \to (\alpha/\gamma)I$, we can rewrite Eq. (1) as

$$\frac{\partial}{\partial t}I - \frac{1}{4}\frac{\partial^2}{\partial x^2}I^2 - I(1-I) = 0. \tag{10}$$

It has been shown in Ref. [16] that the following similarity solution exists as $t \to \infty$, and a numerical solution is shown in Fig. 10.

$$I(x,t) = f(t)\left(1 - e^{-|x-d(t)|} - e^{-|x+d(t)|}\right). \tag{11}$$

This describes a bounded localized solution with an extent $2d(t)$ and two expanding fronts, propagating in opposite directions at speed $d(t)$. In Eq. (11), $d(t)$ and $f(t)$ satisfy

$$d'(t) - \frac{1}{2} + 2e^{-d(t)}\frac{\cosh^{-1}\left(e^{d(t)}/2\right)}{\sqrt{-4+e^{2d(t)}}} = 0 \tag{12}$$

and

$$f(t) = \frac{1}{1-4e^{-2d(t)}} - 4\frac{e^{d(t)}\cosh^{-1}\left(e^{d(t)}/2\right)}{(-4+e^{2d(t)})^{3/2}}. \tag{13}$$

From this, an implicit solution for $d(t)$ follows,

$$\sinh\left[2\cosh^{-1}\left(e^{d(t)}/2\right)\right] - 2\cosh^{-1}\left(e^{d(t)}/2\right) = e^t. \tag{14}$$

This equation yields a simple long-term asymptotic solution

$$d(t) = t/2 \quad (\text{as } t \to \infty). \tag{15}$$

By restoring proper physical dimensions, we obtain

$$d(t) = \sqrt{\gamma^2\chi_0/2\alpha}\; t, \tag{16}$$

i.e. the front velocity is simply given by $U_x = \sqrt{\gamma^2\chi_0/2\alpha}$. This solution indicates that the dynamics of $I(x,t)$ developing from a localized source of turbulence evolves in two steps. First, there is a rapid growth to local saturation at $I = \gamma/\alpha$. Second, the value $I = \gamma/\alpha$ defines an effective value of the intensity-dependent fluctuation diffusion $\chi = \chi_0 I = \chi_0\gamma/\alpha$. A classic Fisher–KPP front with velocity $U_x = \sqrt{\gamma\chi/2}$ is known as the solution for the reaction–diffusion equation given above. There, γ should be interpreted as a reaction rate constant. In the context of our MFE problem, this structure is a consequence of the spatial coupling induced by a combination of local turbulence growth (with linear growth rate γ) and the effective nonlinear diffusion ($\chi = \chi_0\gamma/\alpha$). This front propagation on a hybrid time scale (a geometric mean of a microscopic turbulence rate and a transport rate for macroscopic profile evolution) is a prime example of a mesoscale phenomenon that is lost in a local or quasi-local model. It is crucial to note that the front of turbulence intensity can propagate ballistically (*i.e.* $x_{\rm front} = U_x t$), even in the absence of toroidicity-induced coupling of neighboring poloidal harmonics. Therefore, the rapid propagation should be considered as a more general consequence of the nonlinear dynamics. Since the scaling of U_x from Ref. [16] is drastically different from that expected based on linear toroidal coupling [13], and typically faster, gyrokinetic simulations with the varying linear drive can provide crucial information on the dominant mechanism responsible for turbulence spreading. These studies will be discussed in Sec. II.4.

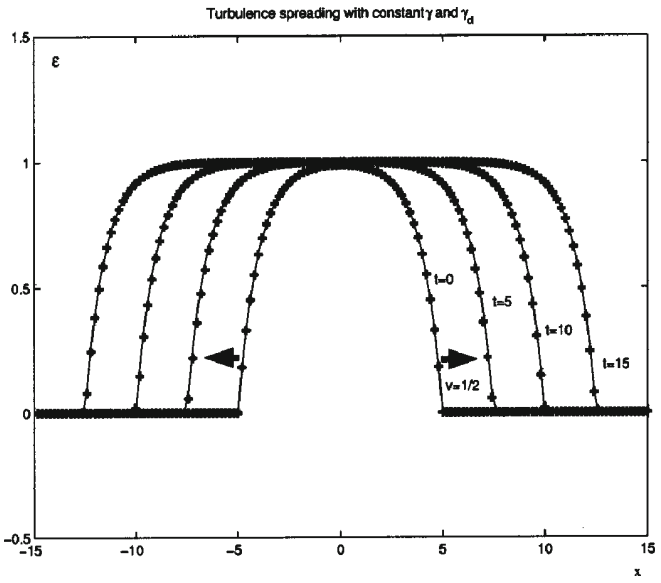

Fig. 10. Constant velocity expansion for the cases $\gamma =$ const and $\alpha =$ const. The numerical simulation represented by the dots is in excellent agreement with the asymptotic analytical solution represented by the solid lines. Even more complex initial conditions approach the same asymptotic solution. (Reproduced with permission from Ref. [16], AIP Publishing.)

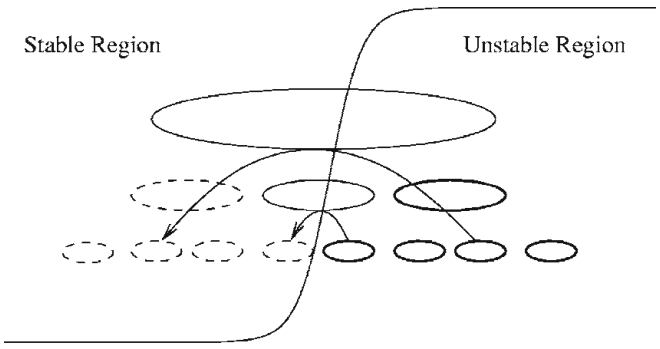

Fig. 11. Spreading can occur via nonlinear mode couplings. Both the inverse cascade and forward cascade (usually of different quantities) are important for the spreading to be significant. The inverse cascade of energy in the unstable region may result in radially elongated convective cells that spread the internal energy very effectively. The internal energy then cascades forward and is damped in the stable region. If the nonlinear transfer rate is faster than the damping rate, turbulence can accumulate in the stable region. (Reproduced with permission from Ref. [43], AIP Publishing.)

Various extensions of Eq. (1) have been studied. First, within the context of the one-field model, the effect of radial group velocity can be incorporated by the addition of a convective term $v_{gx}\partial I/\partial x$ to Eq. (1) [16]. This can also be derived from a Fokker–Planck theory and straightforwardly introduced as radial convection of the fluctuation field. It could also be considered as a simple way of approximating the effect of toroidicity-induced coupling of neighboring poloidal harmonics. Pioneering numerical simulations have reported that the toroidal coupling leads to a ballistic propagation of the fluctuation front, as expected [13]. Generalizations of Eq. (1) to multi-field models allow investigations of the heat pulse [29,37, 38] and of the ITB formation [39], and more recently of the bistable dynamics due to corrugation of mean profile [40]. More details of these studies will be discussed in Sec. III.1.

A key aspect of Fisher fronts is that they are intrinsically *uni-stable* and *super-critical*. $\gamma > 0$ is required for ballistic propagation. Fisher fronts decay exponentially in locally damped regions. This in turn begs the question of what is the role of spreading in a system that is already unstable?! One possible resolution (noted above) is that intensity influx by spreading exceeds the rate of local growth. Another is that the system is *bistable*, and thus pathways to *subcritical* excitation are in play. To this end, we note that recent experimental studies from LHD have indeed observed hysteresis in both the flux-gradient relation and the flux–fluctuation intensity relation [41]. It is important to note that the plasmas for this experiment were routine L-mode discharges, with no detectable transport barriers. Both of these findings are suggestive of bistability, and thus subcriticality. In turn, this suggests spreading into subcritical regions of bistable systems as an important process for redistribution of turbulence intensity. In a subcritical system, a finite amplitude slug could propagate by triggering progressive local growth — rather like an avalanche. Studies of spreading in bistable systems are ongoing [42].

At this point, a critical reading considers two related questions:

i) Noting that the theoretical description of turbulence spreading is based on phenomenological single-field, reaction–diffusion equations, can a systematic theory of turbulence spreading be developed in the vein of statistical closure theory?

ii) What is the role of the zonal flow in turbulence spreading?

Reference [43] answer question (i) in the affirmative and illuminate some aspects of question (ii). Although a lengthy discussion of this technical work is beyond the scope of this reviewe, here, we discuss the basic concepts and principal results.

Gurcan *et al.* (2006) explore the interplay between nonlinear mode couplings (in **k** space) and spreading in real space, in the context of the Hasegawa–Wakatani model. Recall that fluctuation energy in that model is composed of both kinetic and internal contributions. Typically, kinetic energy tends to be transferred to large scale (as in a 2-D inverse cascade), while internal energy scatters to small scales (as in a forward cascade). Thus, the large fluid cells produced by inverse cascade can effectively spread turbulence, especially the internal energy.

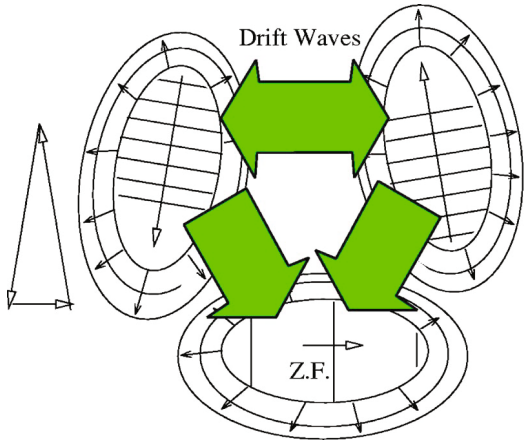

Fig. 12. (Color online) Cartoon of the two-scale direct interaction between a zonal flow and two drift waves of equal and opposite poloidal wave numbers. Drift waves spread one another as well as the zonal flow. Zonal flow allows that to happen only by completing the triad, *i.e.* permitting interaction. Notice that there are many other triangles completed by many other **k**s. In fact, when one of the legs is not a zonal flow, all the legs contribute to spreading, unlike the zonal flow, which gets a free ride. (Reproduced with permission from Ref. [43], AIP Publishing.)

This interaction of transfer and spreading is described in Fig. 11.

The intuitive picture described above is supported by a two-scale Direct Interaction Approximation analysis (which neglects the dynamical evolution of n,ϕ cross-correlation). The upshot is two coupled reaction–diffusion equations for K, the kinetic energy density ($\sim \langle(\nabla\phi)^2\rangle$), and N, the internal energy density ($\sim \langle(\tilde{n}/n_0)^2\rangle$). These reduce properly to the simpler models discussed earlier in this paper. An interesting conclusion of this analysis is that the spreading of internal energy tends to 'lead' the spreading of kinetic energy. This is plausible, as internal energy N behaves in a way that is similar to the mean square passive scalar concentration $\langle\tilde{c}^2\rangle$, and so will be mixed. Kinetic energy, however, will be concentrated in large long-lived cells.

The analysis also addresses the interesting question of zonal flow effects on spreading. The key point is, of course, that zonal flow energy is tightly coupled to turbulence energy and cannot spread independently of it. Indeed, it is the *sum* of drift wave and zonal flow energies that spreads. This is illustrated in Fig. 12. The bottom line, then, is not surprising — zonal flows are *not* the predominant agents of spreading. This conclusion takes issue with other contemporary studies.

Several interesting questions are raised by this paper and remain topics for further study. One is the effect of zonal flow damping on spreading. Another is how effectively turbulence–GAM interaction can spread turbulence. Note that GAMs can propagate independently. A third is spreading via multi-scale interaction — *i.e.* could turbulence spread through a barrier by being converted to electron scales by shearing, spread, and then re-convert to ion scales on the other side? There are many possibilities for further research here!

3. Effects on confinement scaling

Transport scaling with respect to the device size is not only an outstanding practical issue for extrapolation to larger fusion reactors in the future, but also a scientific challenge for which a deeper and more thorough understanding is required. Most present day tokamaks have exhibited that ion thermal transport scaling is closer to Bohm rather than gyro-Bohm scaling. Here, the Bohm scaling for a diffusivity "χ" is given by $\chi_{\rm B} \propto cT_i/|e|B$ without an explicit dependence on the machine size given by a minor radius "a". On the other hand, the gyro-Bohm diffusivity scales like $\chi_{\rm gB} \propto (\rho_i/a)(cT_i/|e|B)$, where ρ_i is the thermal ion gyroradius. Gyro-Bohm scaling implies that bigger is better — *i.e.* as the plasma size gets bigger, the transport coefficient gets smaller.

Experimental findings of transport scaling closer to Bohm [13, 44, 45] are not easy to reconcile with the observed density fluctuation characteristics [45, 46] of tokamaks. Typical turbulence eddy size was found to be roughly on the order of several ion gyroradii, *i.e.* $l_{\rm eddy} \propto \rho_i$. Then, either from dimensional analysis or a radially local theory, one is led to gyro-Bohm scaling,

$$\chi \propto \frac{l_{\rm eddy}^2}{\tau} \propto \frac{\rho_i}{a}\frac{cT_i}{|e|B}, \tag{17}$$

where the characteristic temporal scale for a random walk τ is given by the inverse of the diamagnetic frequency $\omega_{*pi} = k_\theta \rho_i v_{Ti}/L_p \propto v_{Ti}/L_p$, for $k_\theta \propto \rho_i^{-1}$, as observed from fluctuation measurements.

Nonlinear gyrokinetic simulations since late '90s also reported that the eddy size scales with the ion gyroradius [47, 48]. Most nonlinear gyrokinetic simulations mentioned in this review are based on the electrostatic nonlinear ion gyrokinetic formalisms in toroidal geometry [49,50] with adiabatic (Boltzmann) electrons unless specified otherwise. Earlier global simulation results which reported the dominance of radially elongated eddies — the radial size of which increased with the device size — were misleading. This was due to improper, non-self-consistent treatment of self-generated zonal flows and relatively small simulation domain sizes.

Turbulence spreading is a prime candidate for reconciliation of this microscopic turbulence eddy size and transport scaling that deviates significantly from gyro-Bohm scaling. In this subsection, we briefly review a prediction of the transport scaling based on the simple nonlinear diffusion model described in Sec. II.2.A. The nonlinear gyrokinetic simulation results, which are in broad agreement with it are also reviewed. While the radial spreading of turbulence has been widely observed in early global

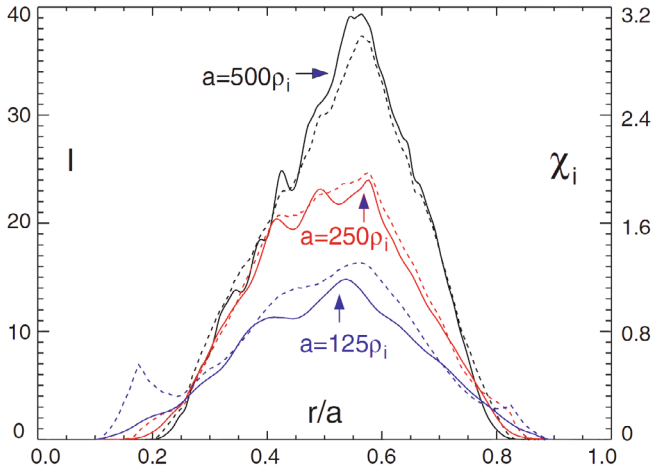

Fig. 13. (Color online) Fluctuation intensity profiles (I in solid lines) and ion thermal diffusivity (χ_i in dotted lines) from GTC simulations, both in gyro-Bohm units after nonlinear saturation for $a/\rho_i = 125$, 250 and 500. As the system size gets larger, the extent of radial spreading of turbulence into the linearly stable zone gets narrower relative to the system size. It scales with the ion gyroradius $\sim 25\rho_i$. (Reproduced with permission from Ref. [55], AIP Publishing.)

nonlinear simulations [13, 24, 51–54], its relation to the turbulent transport scaling was not been addressed until 2002 [25]. In Eq. (5), we assumed that the radial profile envelope of the fluctuation just after a "local" nonlinear saturation is given by $I_0(x, 0)$. Then, the ion thermal diffusivity from the local nonlinear saturation (in the absence of spreading) is given by $\chi_{i0} = \chi_0 I_0$, and should scale according to the gyro-Bohm. A self-similar solution (Eq. (5)) of the nonlinear diffusion equation exhibits that in the absence of dissipation, fluctuation front penetration into the linearly stable zone by a radial width Δx reduces the peak fluctuation intensity at $x = x_i$ to

$$I_0(x_i, T) = \frac{I_0(x_i, 0)}{1 + \Delta x/W}. \tag{18}$$

Since we are considering the regime where $\chi_i \propto I$, we obtain

$$\chi_i = \frac{\chi_{i0}}{1 + \Delta x/W}, \tag{19}$$

where χ_{i0} is the ion thermal diffusivity in the absence of the radial spreading of turbulence.

Having established a relation between the radial turbulence spreading depth and transport scaling in Eq. (19), we discuss observations from global nonlinear gyrokinetic simulations and possible relevance of the theoretical predictions to these simulations [25, 55]. Simulation parameters used in Refs. [14, 55] are based on those from Ref. [56], which uses a simple characterization of a typical DIII-D H-mode core plasma. A system size ($a/\rho_i = (\rho_*)^{-1}$) scan is then carried out with other dimensionless parameters fixed with a radial variation of ITG included. The peak value of R/L_{T_i} is 6.9, which is well above marginality. Towards the axis and the edge, the gradient is weaker. Detailed two-point correlation analysis of simulation data shows that the correlation length of fluctuations scales with ion gyroradius, $l_{\rm eddy} \simeq 7\rho_i$, and these are invariant with respect to the system size. In the nonlinear phase of simulations, fluctuations spread radially. The radial extent of spreading is approximately $25\rho_i$ or $3-4$ radial correlation lengths, in each direction. Interestingly, it is independent of the system size, as inferred from Fig. 13 [55]. Using the values of $W, \epsilon, \chi_0, \gamma'$ and α from simulations, the predicted scalings and values of Δx given in Eq. (7) have been estimated as described in Ref. [14]. For the values estimated in Ref. [14], Eq. (7) yields $\Delta x \simeq 18\rho_i$, which is in the range of fluctuation spreading observed in our simulation ($\Delta x \simeq 25\rho_i$). This is despite the simplicity of the nonlinear diffusion model. If we use the value of Δx from the simulation, Eq. (19), which is based on the simple one-dimensional nonlinear diffusion theory, is in agreement with the scaling trend observed in the simulations [25].

According to the nonlinear diffusion model, the deviation of transport scaling from the gyro-Bohm is quantified by the $\Delta x/W$ factor in Eq. (19). Here, W is the half-width of the zone of strong linear instability. In GTC simulations [25,55], $(\rho_*)^{-1} = a/\rho_i$ was varied from 125 to 500 for a fixed value of $W/a \simeq 0.25$. It was found from simulations that $\Delta \simeq 25\rho_i$, independent of the system size a. From this, the Bohm to gyro-Bohm transition observed in Ref. [25] has been matched by taking $\Delta x/W \simeq 25\rho_i/0.25a \simeq 100\rho_*$ in Eq. (19).

Recognizing its importance for extrapolations from the present day tokamak to ITER and larger fusion reactors, transport scaling with respect to the system size has been further investigated [57] using different gyrokinetic codes (ORB5 [58] and GENE [59]) employing different numerical methods. These studies included a scan of W/a, in addition to the ρ_*-scan. The authors noted that $\rho_{*,\rm eff} = \rho_i/2W$, rather than ρ_*, is the key dimensionless quantity that quantifies the deviation from the gyro-Bohm scaling. This conclusion further supports the prediction of Eq. (19) from the nonlinear diffusion model.

There have also been other gyrokinetic simulations using GYRO [60] and GS2 [61] codes addressing this problem [62]. They reported a convergence of $\chi/\chi_{\rm gB}$ to a value considerably smaller than that from the GTC result as $(\rho_*)^{-1} \to \infty$. However, most of the difference can be attributed to different model equilibria employed in different simulations [55,57,63]. For the same equilibrium, the results from ORB5 and GENE [57] agree with that of GTC [25]. A way to incorporate some of turbulence spreading effects into transport modeling has also been described [64].

It is also of scientific and practical interest to know how turbulence spreading depends on magnetic shear $\hat{s} = d\ln q/d\ln r$ and safety factor q. Detailed numerical experiments using a gyrokinetic code GKPSP [65]

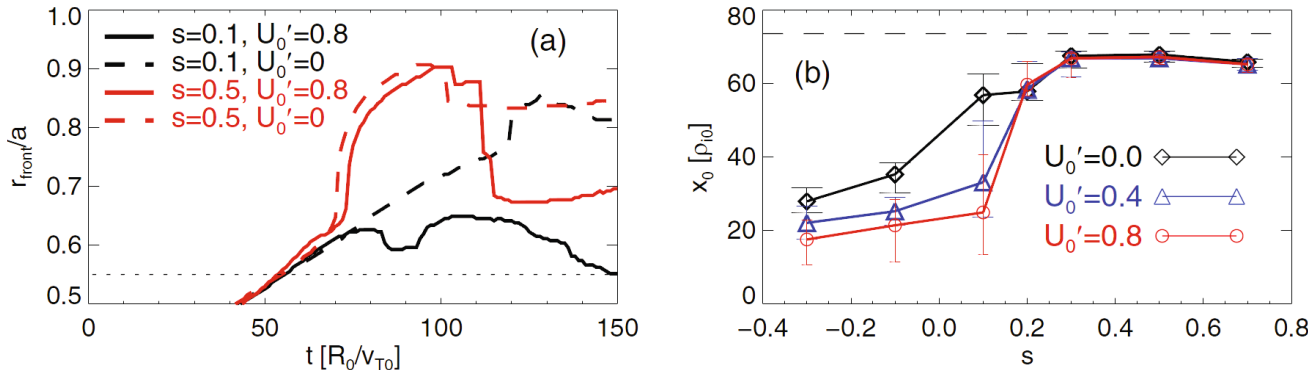

Fig. 14. (Color online) (a) Position of the front of turbulence intensity profile in time for difference s and $U_0^{'}$. The dotted, horizontal line indicates the location of the rotation shear. (b) Penetration depth x_0 as a function of s for difference $U_0^{'}$. These are from GKPSP simulations. (Reproduced with permission from Ref. [67]. Copyright 2015 IAEA, Vienna.)

and their analyses have shown that turbulence spreading is strongly affected by $\hat{s}$ but not by q itself. Turbulence spreading is most efficient at a modest value of positive magnetic shear $\hat{s} \sim 0.5$. On the one hand, it drops for higher $\hat{s}$ values due to a decrease of the mode correlation length. On the other hand, for low magnetic shear ($\hat{s} < 0.3$), the mode correlation length is long, similar to that for the modest positive magnetic shear case ($\hat{s} \sim 0.5$). However, the *time* required for the nonlinear interactions to scatter fluctuation energy into the stable region actually increases. This increase in the characteristic interaction time has a stronger impact on spreading than the increase of the mode correlation length. Consequently, the overall spreading efficiency drops for low magnetic shear [66].

Results from an ensuing study for a wider range of $\hat{s}$ (including negative magnetic shear) and with toroidal flow shear are summarized in Fig. 14. A key result is that suppression of turbulence spreading by toroidal flow shear is only effective for low magnetic shear [67]. Spatio-temporal evolution of turbulence intensity front and the penetration depth from simulations for different values of toroidal flow shear and magnetic shear are illustrated in Fig. 14. The parametric dependence of the spreading-induced transport on toroidal flow shear and magnetic shear is similar to experimental results on JET [68].

While the prediction based on turbulence spreading is in broad agreement with the aforementioned gradient-driven global simulations, both simulations and theory assumed that the mean profiles are fixed in time. We will discuss more recent results from flux-driven simulations and physics of avalanches in Sec. III.1.

4. Role of turbulence spreading in edge-core coupling

Fusion researchers frequently divide the tokamak into three zones: a central sawtoothing zone, a middle confinement zone often called a "core" zone (usually stiff) and an "edge" or "pedestal" zone. Frequently, the edge zone — specifically, the pedestal height — has been used as a boundary condition for core transport modeling. In this subsection, we show that strong edge turbulence in L-mode plasmas can easily spread into the core, where local turbulence is relatively weak. This phenomenon blurs the traditionally assumed distinction between the "core" and "edge", as some profiles from experiments indicate [69]. Instead, it suggests that the boundary between the two is rather ill-defined in L-mode plasmas. It also identifies one element of the global profile readjustment that follows the L→H transition [70,71] — namely, the reduction of turbulence in the core — which originates at the edge. Application of turbulence spreading has helped elucidate the dynamical connection between the core and edge, and the physics of the core–edge interface zone, sometimes called "no man's land".

A series of numerical experiments has been performed to study the inward propagation [22] of turbulence from the L-mode edge into the core and elucidate physics associated with it using GTC code [47]. This propagation generates a connection zone between the edge and core, which may be considered as a symptom of the oft referred-to as "nonlocality phenomena". Simple cases have been investigated using an ion temperature gradient that increases rapidly with increasing r to study the inward spreading of edge turbulence toward the core. The possibility of edge turbulence influencing core turbulence has been discussed previously [13,72].

All gyrokinetic simulations reported here use representative Cyclone parameters of tokamak plasmas [56] at $r/a = 0.5$. The temperature gradient profile mainly consists of two regions: a "core region" from $r/a = 0.2$ to 0.5, and an "edge region" from $r/a = 0.5$ to 0.8 and a gradual decrease to much smaller values toward $r/a = 0.1$ and $r/a = 0.9$. Electrostatic fluctuations with adiabatic electron response are used in the simulations discussed in this section. While this simple ITG turbulence is not rigorously valid as an edge turbulence model, it *can* elucidate dynamics of inward turbulence spread-

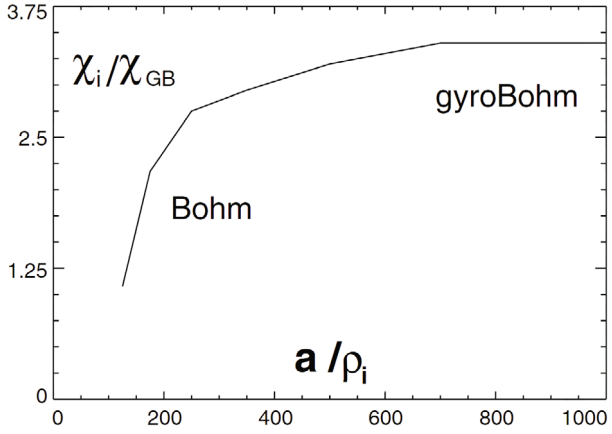

Fig. 15. Ion heat conductivity in gyroBohm unit vs tokamak minor radius in ion gyroradius unit from global nonlinear gyrokinetic simulations. (Reproduced with permission from Ref. [25]. Copyright 2002 by the American Physical Society.)

ing.

In the case summarized in Figs. 16, $R/L_{T_i} = 6.9$ in the core, which is above the effective critical gradient in the presence of zonal flows $R/L_{\rm crit} = 6.0$. The value of the ion temperature gradient at the edge has been doubled to model the stronger gradient at the tokamak edge. This two-step feature for the ion temperature gradient make comparisons with previous core simulations [55,73] and with an analytic model [16] readily feasible. Figure 16 shows the spatiotemporal evolution of the ITG turbulence envelope for the first case with $R/L_{T_i} = 6.9$ in the core. The initial growth in the edge region with $R/L_{T_i} = 13.8$ and a higher linear growth rate is apparent from Figs. 16(a) and 16(b). By the time the edge turbulence saturates at $t \sim 200 L_{T_i}/c_s$, turbulence spreading toward the core is already well in progress. The turbulence spreading can be characterized by nearly ballistic ($\sim t$) turbulence spreading of the front with a velocity $U_x \simeq 2.6(\rho_i/R)c_s$. The time-average value of fluctuation intensity during the last 1/3 of the simulation duration at $r = 0.4a$ (core) is $I \sim 36.5(\rho_i/a)^2$, which is about 60% above the value $I \sim 22.0(\rho_i/a)^2$, given by the core-only simulation with a maximum gradient $R/L_{T_i} = 6.9$ [55]. In this case, the influx of edge turbulence energy from the edge into the core is comparable to the local growth of core turbulence.

We note that a numerical solution of Eq. (1) using the parameters in the simulations (the case with $R/L_{T_i} = 6.9$ at the core) shows a spatiotemporal evolution of turbulence patches (Fig. 17), which is very similar to the simulation results shown in Fig. 16. Since the scaling of U_x from nonlinear diffusion theory (which increases with I and γ) is drastically different from the expectations based on linear toroidal coupling [13], numerical experiments with the R/L_{T_i} scan provide crucial information on the dominant mechanism responsible for turbulence spreading. The front propagation velocity changed

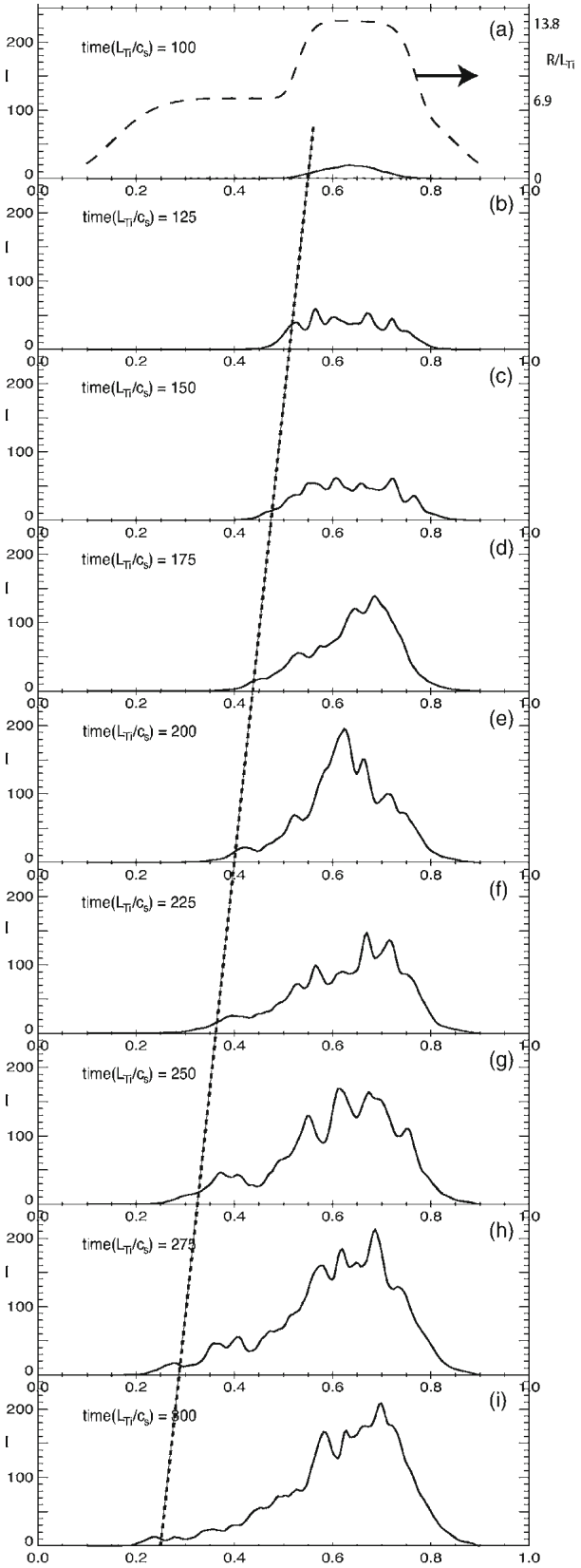

Fig. 16. Spatiotemporal evolution of the turbulence intensity from GTC simulation for $R/L_{T_i} = 6.9$ in the core and 13.8 in the edge. (Reproduced with permission from Ref. [22], AIP Publishing.)

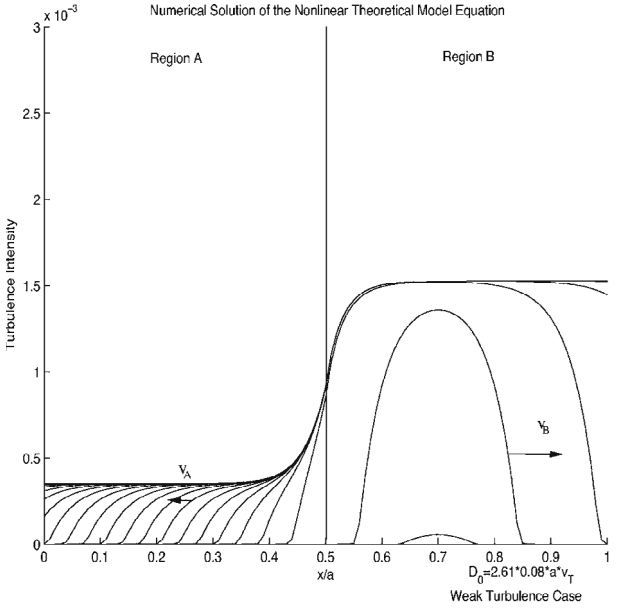

Fig. 17. Spatiotemporal evolution of the turbulence intensity from a numerical solution of Eq. (1) using the parameters used for GTC simulation in Fig. 16. (Reproduced with permission from Ref. [22], AIP Publishing.)

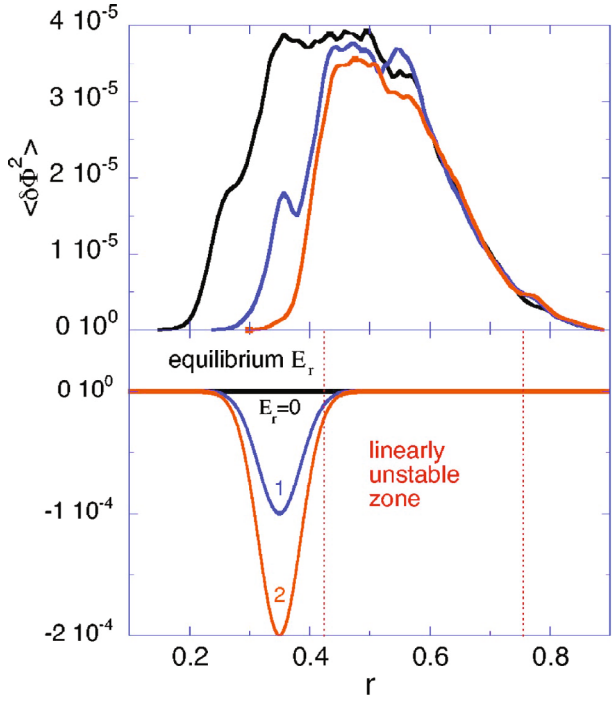

Fig. 18. (Color online) The radial extent of turbulence spreading of steady state fluctuation intensity from GTS simulations is illustrated (upper panel) for three E_r wells (lower panel) with varying depth located next to the unstable ITG source region. (Reproduced with permission from Ref. [77], AIP Publishing.)

significantly from $U_x \simeq 2.1\rho_i c_s/R$ to $U_x \simeq 2.6\rho_i c_s/R$, to $U_x \simeq 4.2\rho_i c_s/R$ as we increased the core gradient from $R/L_{T_i} = 6.1$, to $R/L_{T_i} = 6.9$ to $R/L_{T_i} = 9.0$. The simulation results (which scale approximately like $U_x \propto (R/L_{T_i})^{1.9}$) agree better with the scalings from a nonlinear diffusion model [14,16] than those from linear toroidal coupling $U_x \propto \rho_i c_s/R$.

Ongoing work on edge–core coupling suggests that SOL→core spreading may explain the "shortfall" problem frequently encountered in δf simulations. A key element here is the suggestion that SOL asymmetry induces SOL flows which are unstable to parallel shear flow instability (PSFI) . Such shear-driven fluctuations in turn energize edge turbulence, which ultimately penetrates to no-man's land. This non-local process may ultimately resolve the Short-Fall problem. Ongoing work has yet to address the link between SOL flow reversals and core intrinsic rotation reversals [74].

5. Relation to transport barrier dynamics

As mentioned in Sec. II.1, a non-negligible level of density fluctuations has been observed in the region of flat pressure profile, which is located deeper inside (smaller minor radius side) an internal transport barrier [12]. Moreover, all the known microinstabilities are estimated to be locally stable in that region, according to the comprehensive microstability code FULL calculations [75]. Therefore, this result is difficult to reconcile within the context of local theory. It has been demonstrated in Sec. II.2 that turbulence can spread into the linearly stable regions. Reference [16] has addressed a possibility of turbulence tunneling through locally stable regions of finite radial extent (*i.e.* "gaps" in the linear growth rate profile). The nonlinear diffusion equation (Eq. (1)) has been solved for various piece-wise constant $\gamma(x)$ profiles containing the gaps. It was concluded that the tunneling occurs when the "skin depth" (extent of turbulence spreading to the stable zone) exceeds the radial gap width.

An outstanding question is whether turbulence originated from farther outside (larger minor radius side) of an internal transport barrier (ITB) can propagate through the barrier. Recognizing that a narrow E × B flow shear layer is an important common feature of the transport barriers [76], a number of numerical experiments have been performed using the gyrokinetic tokamak simulation (GTS) code [77]. An E × B flow shear layer is placed next to the linearly unstable zone, as shown in the lower panel of Fig. 18, to represent a transport barrier. There, an electric field well of the following form has been used:

$$E_r = -\frac{d\Phi_0}{dr} = -E_0 \exp\left[-\left(\frac{r-r_c}{\Delta r}\right)^2\right], \qquad (20)$$

which is centered at radius $R_c = 0.35$. The E × B shearing rate is varied by changing the depth E_0. The shearing

rate is defined by [78]

$$\omega_{\rm E} = \frac{(RB_\theta)^2}{B}\frac{\partial}{\partial\Psi}\left(\frac{E_r}{RB_\theta}\right), \tag{21}$$

where B and B_θ are the total and poloidal magnetic field strengths, and Ψ is the poloidal magnetic flux.

Three numerical experiments with different E_r-well depth were carried out. The radial profiles of turbulence intensity $\langle\delta\Phi^2\rangle$ at saturation are plotted and compared in the upper panel of Fig. 18, which shows that the extent of the turbulence spreading decreases with increasing E × B shear. In the case of no E × B shear layer ($E_0 = 0$), turbulence spreads widely to fill up a large area of the stable zones in both directions. The radial extent of the turbulence fluctuation spreading in the inward direction is about $25\rho_i$. As a consequence, significant heat transport is driven not only in the ITG source region but is also observed all the way to a radial location $25\rho_i$ inside the source region. As a moderate radial electric field well is imposed ($E_0 = 1$), with a maximum E × B shearing rate $\omega_{\rm E}^{\rm max} = 0.13c_s/a$, it is observed that the inward spreading is partially blocked. In this case, the radial width of the fluctuation spreading is reduced to about $12\rho_i$. As the applied E_r well becomes deeper, the blocking of the turbulence propagation becomes more effective. As illustrated in Fig. 18, the inward spreading is almost completed blocked for $\omega_{\rm E}^{\rm max} = 0.26c_s/a$ ($E_0 = 2$).

In addition, by analyzing the spatio-temporal evolution of the turbulence propagation front through the E × B shear layer, it has been observed that both the local front propagation speed and the local fluctuation intensity decrease significantly in the region of the strong E × B shear. This correlation between propagation speed and fluctuation intensity is consistent with the predictions of the nonlinear diffusion model of turbulence spreading [14] and shows that the E × B shear is the key quantity for control of turbulence spreading by transport barriers.

Reversed magnetic shear is also known to reduce turbulence in many circumstances and to lead to ITB formation. Numerical experiments addressing turbulence spreading through the $q_{\rm min}$ region have been also performed [79, 80]. It has been observed that turbulence spreading persists in the region of reversed shear where local turbulence excitation is negligible, although no systematic parameter scan and analyses have been attempted. Finally, inward turbulence spreading of electron temperature fluctuation has been observed from a BOUT++ fluid simulation of H-mode pedestal collapse [81]. The spreading stops at the position where the radial turbulent correlation length is shorter than the distance between the rational surfaces.

6. Turbulence spreading through a magnetic island

Turbulence spreading through a magnetic island is an issue of both scientific and fusion-relevant, practical interest. Multi-scale fluid simulations, including both electrostatic microturbulence and magnetic islands, developed from the tearing instability have demonstrated the possibility of spreading through an island. These are visible from figures showing the radial extent of microturbulence, which gets broader in the presence of magnetic islands. However, not much discussion of underlying physical mechanisms has been given until recently. In the case of double tearing modes near $q_{\rm min}$ surface of RS plasmas, the Maxwell stress from magnetic perturbations have been observed to reduce zonal flows and enhance the magnetic island, which in turn allows turbulence spreading by the flux surface breaking [82,83]. Global gyrokinetic simulations investigating turbulent transport near a magnetic island (in a plasma with normal magnetic shear) [84,85] report more detailed nonlinear evolution exhibiting turbulence spreading. Nonlinear mode coupling produces large-scale turbulence, in particular shear flows near the magnetic island. Those large-scale modes are responsible for the residual transport level and incomplete flattening of the electron temperature profile inside the island [84]. Furthermore, high transport in a region of low temperature gradient just outside of the island X-point can be understood by turbulence spreading across the X-point. This turbulence spreading has been described as convective rather than diffusive [85]. Shear flows have been observed at the boundary of a magnetic island from LHD experiment [86].

A qualitatively similar result has been reported from a KSTAR experiment in Ref. [87]. Generation of poloidal vortex flow near magnetic island and its role in regulating turbulence spreading into a magnetic island have been observed. More definite evidence of fast spreading of turbulence from the X-point to the O-point of a magnetic island has recently been reported by Ida *et al.* (2018) [88]. By using modulated electron cyclotron heating (ECH), repetitive electron heat pulses were injected into a magnetic island produced by a nonaxisymmetric magnetic field perturbation coil in DIII-D plasma. Consequent response of the density fluctuations, $\delta n/n_0$ and the T_e are measured by BES and ECE, respectively, at both X-point and O-point regions of a $(m, n) = (2, 1)$ island. It has been observed that the change in T_e precedes the change in $\delta n/n_0$ at the X-point, while the change in $\delta n/n_0$ precedes the change in T_e at the O-point. This result indicates that the density fluctuation δn propagates from the X-point by turbulence spreading before the T_e heat pulse propagates into the O-point of the magnetic island. However, electron heat transport near the X-point can be enhanced by the stochastic field lines. Modulation of turbulent δT_e and δn_e by an $(m, n) = (1, 1)$ magnetic island from an internal kink mode has been observed in core plasma of the HL-2A tokamak [89]. At the inner half region of the island, the level of $\langle\delta T_e^2\rangle$ measured by ECEI is higher than that of the outer-half, despite almost zero local T_e gradient. This has been attributed to the turbulence spreading from outside the island (but at smaller local minor radius region) into the O-point of

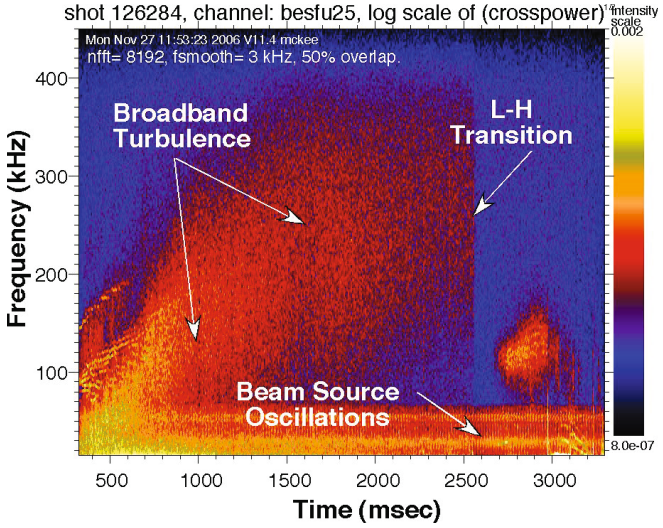

Fig. 19. (Color online) Spectrogram of measured density fluctuations at $r/a = 0.65$ showing evolution of the turbulent density fluctuations. (Reproduced with permission from Ref. [92]. Copyright 2007 by the Japan Society of Plasma Science and Nuclear Fusion Research.)

the island where the T_e profile is flat.

7. Experimental evidence for turbulence spreading

Plasma transport is often found to be anomalous in the region of very weak pressure gradient where linear instabilities are estimated to all be stable [11]. Non-zero fluctuations and anomalous transport have been observed in the linearly stable zone of a JT-60U reversed shear plasma, as shown in Fig. 6 [12]. These puzzling results can be reconciled by considering the possibility of nonlocal effects, specifically turbulence spreading. While this is a plausible scenario, more direct evidence of turbulence spreading would require measurements of spatio-temporal evolution of fluctuations propagating from the linearly unstable zone to the linearly stable zone. These have been demonstrated in various aforementioned numerical experiments [77,79,80]. An example is shown in Fig. 18.

Measurement of turbulence spreading in experiment is much more challenging since in steady state, one ends up observing the consequence (net result) of various mechanisms, including local nonlinear saturation and nonlocal effects. This difficulty can be overcome by considering plasmas immediately after the transport barrier formation or its destruction [90, 91]. Supporting evidence of turbulence spreading from experiments can be found from a quasi-local beam emission spectroscopy (BES) measurements of density fluctuation at core before, during and after H-mode transition and formation of edge transport barrier (ETB) of DIII-D tokamak

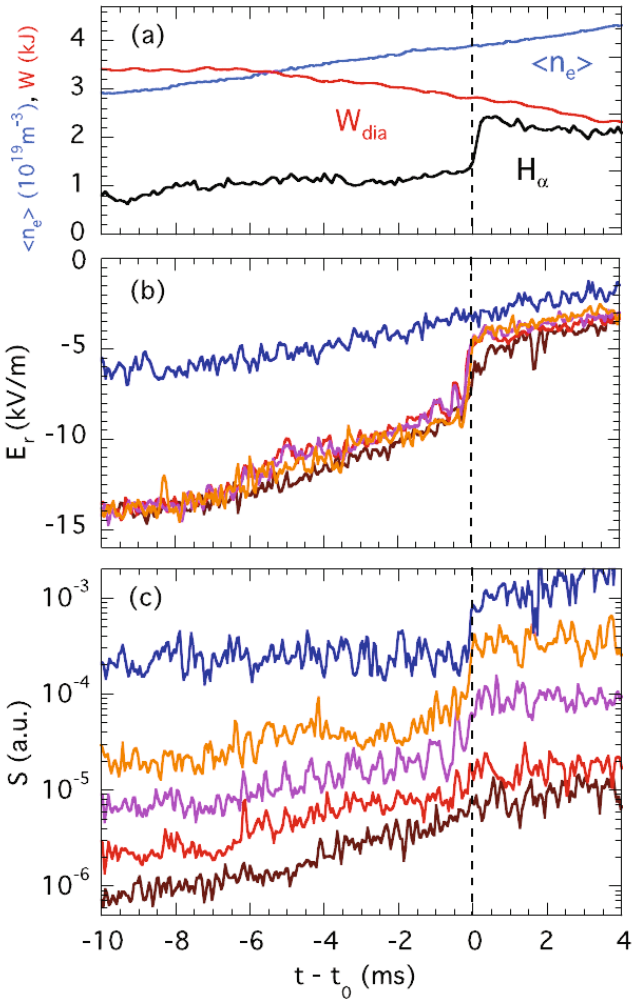

Fig. 20. (Color online) (a) The time evolution of line-averaged plasma density, plasma energy content and H_α signal, (b) E_r and (c) density fluctuation level measured at radial positions adjacent to the E_r-shear; from top to bottom, $\rho - \rho_{\rm shear} = +0.01, -0.01, -0.03, -0.06$ and -0.07. The vertical line indicates the time of the H to L back transition. (Reproduced with permission from Ref. [93]. Copyright 2011 IAEA, Vienna.)

[92]. As shown in Fig. 19, the fluctuation level at core ($r/a \simeq 0.65$) drops in a short timescale (shorter than the transport timescale) after the H-mode transition at the edge ($r/a \geq 0.95$). This cannot be explained by local stability-based theory or modeling.

Another experimental result supporting the turbulence spreading has been reported by the TJ-II stellarator [93]. Both radial electric field and density fluctuation were measured before, during and after the H to L back transition at different radial positions adjacent to the E × B shear layer in the H-mode phase. During H-mode phase, strong E_r-shear layer exists, as shown in Fig. 20(a) and the turbulence is appreciable only outside of that layer, as shown in Fig. 20(b). As the E_r-shear begins to decrease prior to the H to L back transition, the

Fig. 21. (Color online) Sandpile (Reproduced with permission from Ref. [94].)

turbulence at inner radial positions increases on a similar timescale. This happens before the abrupt increase of H_α signal, implying a local increase in particle flux and the pedestal collapse, as shown in Fig. 20(c). These experimental results are consistent with a turbulence spreading mechanism that is inhibited by the strong E × B shearing rate in H-mode [77]. More experimental evidence of turbulence spreading near magnetic islands have already been mentioned in Sec. II.6.

III. AVALANCHES

1. Self-Organized-Criticality (SOC) as a model for plasma transport

This section deals with self-organized criticality (hereafter SOC, broadly interpreted) and *avalanching*. Fundamental to the SOC concept is a system — such as the prototypical sandpile — with a significant disparity in scales between that of a basic element or cell, Δ, and that of the system L. Obviously, $\Delta/L \ll 1$ bears a correspondance to $\rho_* \ll 1$, which is characteristic of all relevant regimes of magnetic confinement. SOC's relax by transport events or *avalanches*, in which some number of cells sequentially discharge or overturn, producing a transient flux. Such 'overturning' is an equivalent word for 'fluctuation'. Hence, avalanches imply extended, collective fluctuation events, which necessarily result in turbulence spreading. Thus, avalanches and SOC are germane to this review. Later, we will compare and contrast the closely related phenomena of turbulence spreading and avalanching.

In this section, we review basic aspects of SOC, with emphasis on aspects relevant to magnetic confinement. This review consists of subsections on:

i) What is SOC, and what does it mean?

ii) A brief intellectual prehistory of SOC

iii) Basic model paradigms: piles, avalanches, hydrodynamic models

iv) SOC in magnetic fusion energy (MFE) plasmas, with emphasis on avalanching

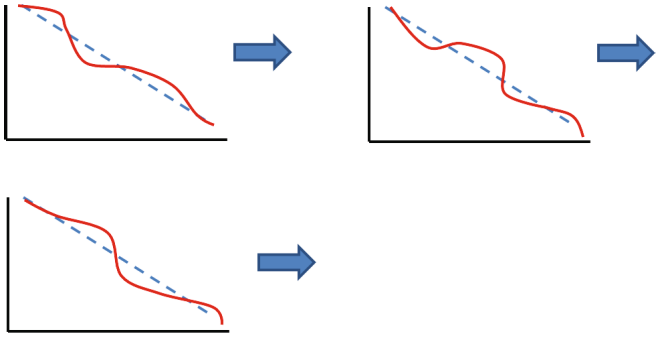

Fig. 22. (Color online) Multiple, metastable states (Reproduced with permission from Ref. [94].)

v) Some further discussion of avalanche physics

This discussion is tightly focused, and thus necessarily is incomplete. In particular, we do not deal with applications outside MFE.

A. What is SOC, and what does it mean?

Following a *constructive* approach, a SOC is defined as *a slowly driven, interaction-dominated threshold* system. A classic example is the sandpile (Fig. 21). A *phenomenological* definition of a SOC is a *system exhibiting self-similarity* (*i.e. power law scaling*) *without tuning*. Systems exhibiting $1/f$ or flicker/shot noise are of special interest. Elaborating on the elements of these definitions:

- *Interaction dominated* means many degrees-of-freedom (*i.e.* cells or modes), with the dynamics determined by DOF (degrees of freedom) interaction or coupling.

- *Tthreshold* and *slow drive* refers to a local "switch-on" criterion for excitation. This implies a large number of accessible, meta-stable, slowly evolving configurations, as shown by the cartoon in Fig. 22. Proximity to a SOC state suggests local rigidity of the configuration (*i.e.* profile). Such rigidity is consistent with time-honored MFE notions of 'stiffness', 'profile resiliency', 'profile consistency' etc. One major issue is understanding quantitatively the precise difference between the SOC state and the marginal state (the state defined by the overturning threshold). In general, these two are not the same. *Slow drive uncovers* the threshold, and ensemble of metastable states. Strong drive buries the threshold, as it does not allow time for relaxation between metastable configuration times. The inevitable question of 'How strong is strong?' is met with the inevitable answer of 'It depends' — specifically on the mixing/toppling rules, box size, fueling rate, etc. These naturally define the scaling

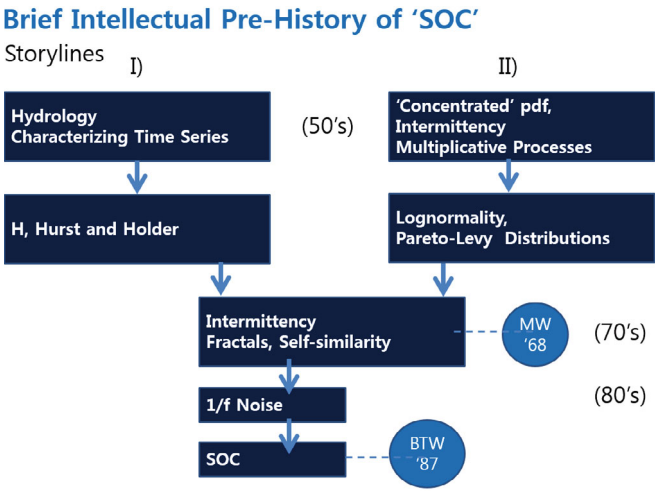

Fig. 23. (Color online) Brief Intellectual Prehistory of 'SOC' (Reproduced with permission from Ref. [101].)

of the flux with deviation from criticality - *i.e.* the critical exponent for the system.

- *Power law scaling* reflects that SOC phenomena are intrinsically self-similar, reflecting the absence of scale on the range $\Delta < l < L$. SOC is intimately related to Zipf's Law [95], *i.e.* the probability of an event (*i.e.* transport event) $P(E) \sim 1/\Delta(E)$, where Δ is the size. Another signature of SOC is $1/f$ noise, *i.e.* $S(f) \sim 1/f$, where f is frequency and S is the spectral density.

B. Intellectual prehistory of SOC

The SOC concept emerged from the merger and development of two story lines. The first, with its origins in hydrology from the work of Harold Hurst [96–98], focused on characterizing dynamics based on time series. The second emerged from the effort to characterize the non-Gaussian statistics of 'concentrated' intervals of activity, which (usually) emerge from multiplicative processes. Names prominent in this line include that of the polymath Wilfredo Pareto and the mathematician Paul Levy. The two lines merged with the development of the fractal theory of intermittency by Benoit Mandelbrot [99] and others. This then drove attempts to understand, and realize in a physical context, phenomena of $1/f$ noise. SOC emerged as an outgrowth of that, in the classic paper of Bak, Tang and Wiesenfeld in 1987 [100]. This guide to the prehistory of SOC is summarized in Fig. 23.

The effort to characterize the physical nature of events described by time series records originated in the work of Harold E. Hurst [96–98], who was a hydrological engineer, active in the design and construction of the Aswan

Fig. 24. (Color online) Flow-and-reservoir problem. (Reproduced with permission from Ref. [101].)

Noah, Joseph, and Operational Hydrology

BENOIT B. MANDELBROT

JAMES R. WALLIS

International Business Machines Research Center
Yorktown Heights, New York 10598

Dedicated to Harold Edwin Hurst

Abstract. By 'Noah Effect' we designate the observation that extreme precipitation can be very extreme indeed, and by 'Joseph Effect' the finding that a long period of unusual (high or low) precipitation can be extremely long. Current models of statistical hydrology cannot account for either effect and must be superseded. As a replacement, 'self-similar' models appear very promising. They account particularly well for the remarkable empirical observations of Harold Edwin Hurst. The present paper introduces and summarizes a series of investigations on self-similar operational hydrology. (Key words: Statistics; synthesis; time series)

Fig. 25. Abstract of the paper "Noah, Joseph and Operational Hydrology". (Reproduced with permission from Ref. [102]. Copyright 1968 American Geophysical Union.)

High Dam in Egypt. This project required a statistical characterization of Nile flow and discharge, so as to understand and predict the time variation of the dam's reservoir content. The Nile flow was highly variable, and predictive modelling required meticulous observation. The goal was to ensure the dam's reservoir would be sufficient to prevent flooding and dam overflow in years of heavy rain. A cartoon of the flow-and-reservoir problem is given in Fig. 24. Readers from the MFE community will note the close analogy between this problem and that of pedestal relaxation, *i.e.*

sources	$\leftrightarrow$	heating
river	$\leftrightarrow$	core heat flux
reservoir	$\leftrightarrow$	edge pedestal (in H-mode)
dam	$\leftrightarrow$	edge transport barrier
discharge	$\leftrightarrow$	loss to SOL, etc

Hurst successfully used a combination of careful record-keeping and analysis. The Aswan High Dam has operated without problems to this day. Interestingly, although it has been surpassed in size (by a considerable margin) by the Three Gorges Dam and others, the *reservoir* of the Aswan High Dam remains the largest such reservoir in the world. Evidently, Hurst took a conservative (and successful) approach.

In a classic paper entitled "Noah, Joseph and Operational Hydrology" (dedicated to Hurst), Mandelbrot and Wallis set forth a generalized approach to time series analysis by exploiting self-similar models [102]. The abstract of that paper is reproduced in Fig. 25.

The focus was on how to address strongly non-Gaussian phenomena, such as 'Noah' events (*i.e.* rare,

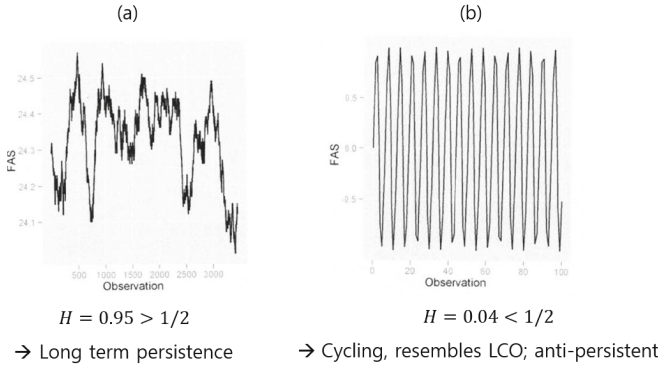

Fig. 26. H measures memory in dynamics [103].

large events, named after the great Biblical flood) and the 'Joseph effect' (*i.e.* periods of prolonged duration of the same conditions, such as a surplus of flood, or a famine). The upshot was a generalization of the random walk scaling, familiar Brownian motion, by means of H, the Hurst (and Holder) exponent.

Specifically, the Hurst exponent (named for Harold Hurst, above) is defined as the expected value $E\{\ \}$ of the squared deviation of a time series $B(t)$ in a time interval T. Thus, H is defined by

$$E\{[B_H(t+T) - B_H(t)]^2\} = T^{2H}. \tag{22}$$

Thus, $H = 1/2$ corresponds to the familiar random walk, which occurs in Brownian motion. However, H ranges between $0 \leq H \leq 1$, where for:

a) $1/2 < H < 1$,
the dynamics manifest a sustained memory, and positive correlation in time. $1/2 < H < 1$ suggests long-term persistence, as encountered in the Joseph and Noah effects.

b) $0 < H < 1/2$,
the dynamics exhibit rapid switching between high and low values, suggestive of temporal anti-correlation.

Thus, *H is a measure of the memory in the dynamics.* Some examples are shown in Figs. 26(a) and (b). Figure 26(a) shows the graph of a series with $H = 0.95 > 1/2$. Long-term persistence is evident, and so is long-term memory. Figure 26(b) shows the graph of a series with $H = 0.04 < 1/2$. This series exhibits rapidly cycling and anti-persistent dynamics, which resemble a limit cycle oscillation (LCO).

In the context of practical problems, the Hurst exponent is determined by *R/S Analysis.* R/S analysis seeks to compare the range (R) of cumulative deviations to the standard (S) deviation, in order to determine H. The approach of R/S analysis somewhat resembles that used to determine the Gini coefficient in economics. Recall the Gini coefficient measures the concentration of wealth in the population. A high Gini coefficient means that the nation's wealth is concentrated in a small fraction of the population. Specifically, if one has a stationary time series $x_1, x_2, \ldots x_n$, then H is defined by

a) $c\, n^H = E\{R(n)/S(n)\}$.
Here $R(n)$ is the *range* of the first n values. Thus,

b) $R(n) = \max(z_1, \ldots z_n) - \min(z_1, \ldots z_n)$,
where the z's are the cumulative deviations from the mean.

$S(n)$ is the standard deviation from the mean for the series of n elements. It is also worth mentioning that H is related to the fractal dimension D of the time series, where $1 < D < 2$ and $D = 2 - H$. H is also related to the frequency spectrum of the variation

$$\langle (\Delta B)^2 \rangle_\omega \sim \omega^{-\alpha}, \tag{23}$$

where $\alpha = 2H - 1$. Thus $H = 1/2$ (Brownian motion) gives a white noise spectrum, while $H = 1$ gives $1/f$ noise. The $1/f$ noise issue is central to SOC. More generally, since higher-order moments reveal intermittency, one can define a higher-order Hurst exponent, similar to higher-order structure functions or moments in turbulence.

The other line threading the prehistory of SOC (in addition to the above mentioned Hurst exponent as a measures of persistence in dynamics) is that of intermittency associated with multiplicative processes. This is self-evident: Sandpile toppling events are clearly multiplicative. Here, we give some introductory discussion of multiplicative processes and $1/f$ noise.

Additive processes obey the Central Limit Theorem and exhibit Gaussian statistics. These can be described by Fokker–Planck theory (*i.e.* the second moment of their pdf converges, etc.) and are, in Mandelbrot's words, 'mildly' random. All is well, but they are boring. *Multiplicative* processes, such as avalanching, are more interesting, because they are *wild.* A simple example of a wild multiplicative process is:

$$\begin{aligned} X &= \prod_{i=1}^{N} x_i, \quad \text{where } x_i = 0 \text{ or } 2, \\ &\quad \text{each with probability } p = 1/2. \\ &= x_1 x_2 \ldots x_N. \end{aligned} \tag{24}$$

Then,

a) $\langle X \rangle = 1$,

b) $\langle X^2 \rangle = 2^N$,

the point being that $X = 0$, unless all $x_j = 2$. Then $X = 2^N$ with probability $p = 2^{-N}$. This multiplicative process is *wild*, because it is *strongly intermittent.* All the non-zero probability is concentrated in one outcome. This basically defines *intermittency* as the concentration of probability in a limited set of events. 'Noah' (*i.e.* large) and 'Joseph' (*i.e.* persistent) events are intrinsically intermittent.

Multiplicative processes must be characterized. This brings us to the *lognormal distribution.* The lognormal follows from the fact that in a multiplicative process, the *logs* are additive, *i.e.*

a) $X = \prod_{i=1}^{N} x_i$, so

b) $\log X = \log x_1 + \log x_2 + \cdots + \log x_N$.

Applying the Central Limit Theorem to the sum of logs yields the *lognormal distribution*

$$F(\log X) = \frac{1}{(2\pi\sigma^2)^{1/2}} \exp\left[-\frac{(\log X - \overline{\log X})^2}{2\sigma^2}\right]. \quad (25)$$

Here, we tacitly assume the variance exists. If not, a power law distribution (following Pareto-Levy) results.

The lognormal distribution, Zipf's Law (*i.e.* $P(\Delta) \sim 1/\Delta$, where $\Delta \sim$ event / element size) and $1/f$ noise are all related. If, for a lognormal distribution, we are concerned with the probability that $x/\overline{x}$ lies within $d(x/\overline{x})$ at $x/\overline{x}$, then

$$P(x/\overline{x}) = P(\log x)\frac{d\log x}{dx} = g(x/\overline{x})d(x/\overline{x}). \quad (26)$$

Now $\log g = -\log P +$ corrections, so

$$P = 1/(x/\overline{x}), \quad (27)$$

recovering Zipf's law [95]. Indeed, Montroll [104] has shown that a lognormal is well approximated by a power law $P \sim 1/x$ (Zipf's Law) over a finite range. As multiplicative processes are related to the trend of Zipf's Law, we can then ask what of $1/f$ noise?

Regarding Zipf's Law and $1/f$ noise, these are related but different. Zipf's Law states that the probability of an event of size ΔB, $P(\Delta B) \sim 1/|\Delta B|$, while for $1/f$ noise, the frequency spectrum of ΔB, $\langle(\Delta B)^2\rangle \sim 1/\omega$. Both embody the rarity of large events and ubiquity of small events, suggestive of intermittency phenomena. Both exhibit self-similarity. $1/f$ noise is linked to the Hurst exponent, for $H \to 1$. $1/f$ noise – frequently called flicker or shot noise – is ubiquitous and has been suggested as a 'universal' phenomena. As late as the '80s, it remained very mysterious. It is *not* easy to recover $1/f$ noise. In the usual approach to the question of a frequency spectrum with nonlinear interactions,

$$\langle\phi(t_1)\phi(t_2)\rangle = |\hat{\phi}|^2 \exp\left[-|\tau|/\tau_c\right], \quad (28)$$

$$S(\omega) = \frac{1/\tau_c}{\omega^2 + 1/\tau_c^2} \sim \frac{1}{\omega^2}, \quad (29)$$

so τ_c imposes a scale, but $1/f$ is manifestly scale free!? This suggests that standard methods applied to the case of a conserved order parameter might recover scale invariant frequency spectra. A different, interesting approach was first suggested by Montroll, who proposed consideration of an ensemble of random processes, each

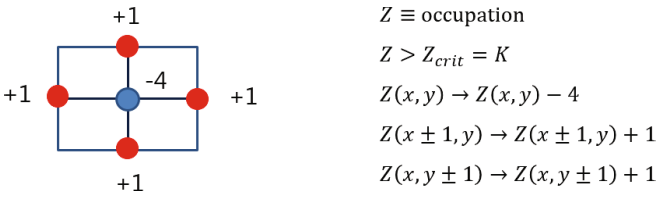

Fig. 27. (Color online) BTW - 2D cellular automota model. (Reproduced with permission from Ref. [94].)

with its own self-correlation time τ_c, which is probabilistically distributed. Then:

$$S(\omega)_{\text{eff}} = \int_{\tau_{c_1}}^{\tau_{c_2}} P(\tau_c) S_{\tau_c}(\omega) d\tau_c. \quad (30)$$

Demanding that $P(\tau_c)$ be scale invariant, *i.e.*, $P(\tau_c) = d\tau_c/\tau_c$, then

$$S(\omega) = \frac{\tan^{-1}(\omega/\tau_c)}{\omega}\Big|_{\tau_{c_1}}^{\tau_{c_2}} \sim \frac{1}{\omega}, \quad (31)$$

which recovers $1/f$ noise. But, one may ask: What does this little model **mean**, in terms of physics? And what is the deeper, more general significance of shot noise? Circa the mid-1980s, there was a need for a simple, intuitive model that captured 'Noah' and 'Joseph' effects in non-Brownian random processes ($H \to 1$), and displayed $1/f$ noise.

C. To SOC

Bak, Tang and Wiesenfeld (BTW) (1987) suggested such a model in their noted paper of 1987 [100] with the amazingly concise abstract, now with over 7,000 citations. The key elements of this paper, motivated by the ubiquity and challenge of scale invariant $1/f$ noise, were:

- Spatially-extended excitations or *avalanches.* Indeed, a statistical ensemble of collective excitations or avalanches is intrinsic to SOC.
- Evolution to self-organized critical structures of states that are 'barely stable'. Note that while the concept of 'marginal stability' has appeared, the SOC state need not be the same as the linearly marginal state. Likewise, the SOC state is *dynamic.*
- The combination of *dynamical* minimal stability and spatial scaling leads to a power law for temporal fluctuations.
- Noise propagates through the scaling clusters by means of a "domino" effect that upsets the minimally stable states. This refers to space–time propagation of avalanching events.

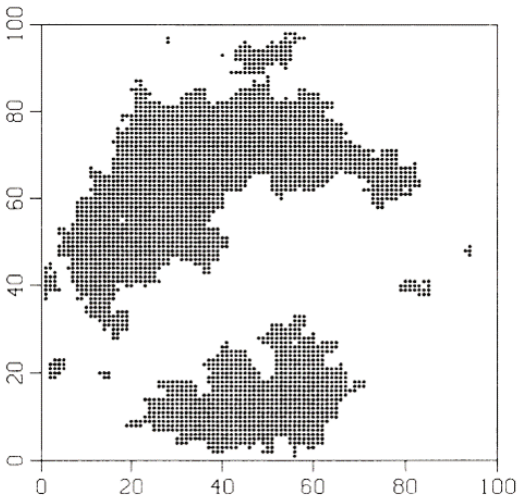

Fig. 28. SOC state of minimally stable clusters, for a 100 × 100 array. (Reproduced with permission from Ref. [100]. Copyright 1987 by the American Physical Society.)

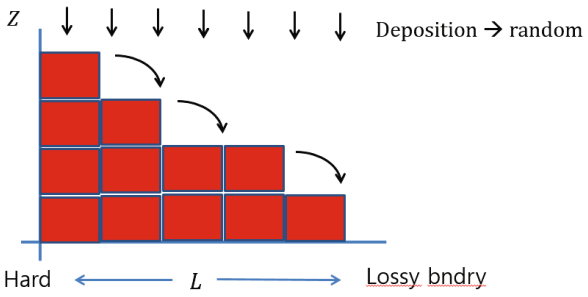

Fig. 29. (Color online) The Classic - Kadanoff *et al.* '89 1D driven lossy cellular automata. (Reproduced with permission from Ref. [94].)

- The critical point in the dynamical systems studied here is an attractor reached by starting far from equilibrium. Thus, we see that noise is essential to *probe* the dynamic state.

To realize collective avalanching, BTW proposed a 2-D cellular automata model described in Fig. 27. This yielded self-organized clusters of the form shown in Fig. 28. These "clusters" are sets of points, which could be reached from the toppling of a single site rather like percolation clusters. *The SOC state was that with the minimally stable clusters.* The cluster size distribution $D(s) \sim s^{-\alpha}$, $\alpha \sim 0.98$, recovered Zipf's law, to high accuracy.

BTW (1987) is notable in the context of fusion physics for introducing the concept of the *avalanche*, a collective yet stochastic exciton formed by the sequential toppling or overturning of neighboring sites of localized cells. The avalanche is intrinsically *mesoscopic*, with scale $\Delta < l < L$, without a characteristic length (such as a linear eigenmode width or a mixing length in MFE) imposed by the system. An avalanche combines profile

$$\text{If} \begin{cases} Z_i - Z_{i+1} > \Delta Z_{crit} \\ Z_{i+1} \rightarrow Z_{i+1} + N \\ Z_i \rightarrow Z_i - N \\ \text{Etc.} \end{cases}$$

Fig. 30. (Color online) Toppling rules of the Kadanoff *et al.* 1989 model. (Reproduced with permission from Ref. [94].)

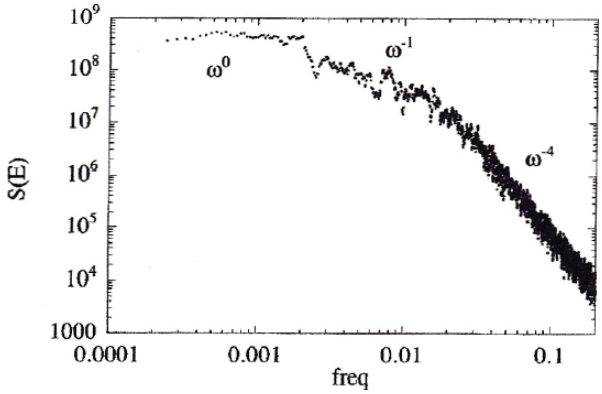

Fig. 31. Power spectrum of overturnings $\langle(\Delta Z)^2\rangle_\omega$. (Reproduced with permission from Ref. [105], AIP Publishing.)

relaxation, transport and fluctuations (*i.e.* the local toppings). Thus, the avalanche is both a stochastic *transport event* and a *turbulence spreading pulse*, and thus takes center stage in this review. In particular, it seems intrinsically impossible to separate avalanching and turbulence spreading.

The 'classic' sandpile cellular automata model was proposed by Leo Kadanoff and collaborators in 1989 [105] (Fig. 29). The idea is simple: $N \sim L/\Delta$ cells — where $N \gg 1$, L is the system size and Δ is the cell size — fill a box with a hard boundary on one end and a loss boundary on the other end. Grains are randomly sprinkled onto the pile. Toppling rules, *i.e.*, Fig. 30, determine when cell overturning occurs. This model is clearly closely analogous to turbulent transport in tokamaks, as summarized by Table 1.

The prototypical open sandpile model of Kadanoff – hereafter referred to as the sandpile model – exhibits some generic trends. The power spectrum of overturnings $\langle(\Delta Z)^2\rangle_\omega = S(\omega)$ manifests three ranges:

- $S(\omega) \sim \omega^{(0)}$ — large events, or 'Noah events'. These events have most of the power, and are the slowest. These are global transport events.

- An intermediate range, with $S(\omega) \sim 1/\omega$. This $1/f$ range is interaction dominated. Here, events are self-similar. The $1/f$ range is one of overlapping and interacting avalanches.

- A small-scale, high frequency range where the

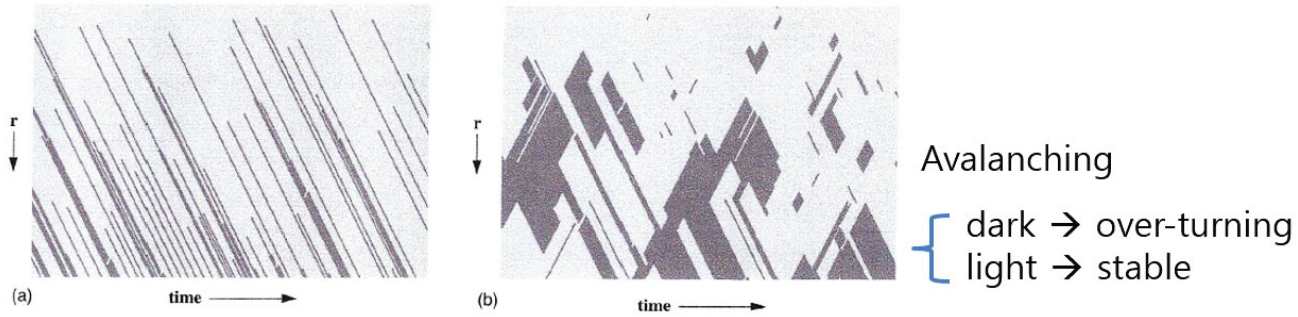

Fig. 32. (Color online) Space–time evolution of avalanching (a) in the bulk and (b) near the boundary. (Reproduced with permission from Ref. [105], AIP Publishing.)

avalanche interactions are with themselves without much overlapping. The power spectrum is shown in Fig. 31.

Space–time evolution of avalanching is shown in Fig. 32. Figure 32(a) shows outward-propagating avalanches in the bulk of the pile. Figure 32(b) shows outward and inward propagation near the pile boundary. Figure 33 shows the time history of total pile grain content. Note the effect of infrequent but large discharge events: one shortly before $t \sim 10^7$ is especially striking.

It is interesting to compare the SOC and the marginal profiles which need *not* be the same! Here the marginal profile is determined by the toppling rule (critical gradient), working inward from the outer boundary, where $Z = 0$ is imposed. Note that the SOC profile is below the marginal profile and approaches it at the edge. For increased fueling (*i.e.* higher $N_{\rm dep}$), the SOC profile slope can exceed that of the marginal profile at the boundary. Indeed, if the toppling rule is bistable, a transport bifurcation can occur at the boundary [107, 108]. This gives a simple understanding of why the L-H transition occurs at the outer boundary, and provides a more universal and robust mechanism than ion-orbit loss-based arguments.

- *Hydrodynamic Models*

By now, it should be evident that SOC is intimately connected to self-similar transfer, cascades, *etc.* — all notions rooted in the long-established phenomenology of fluid turbulence. This observation begs the question: Can the discrete cellular automata (CA) pile and the fluid picture be linked in a continuum, hydrodynamic model of SOC evolution? Such a model would be of considerable use for applications to MFE. To this end, the C in SOC stands for 'criticality'. And the textbook paradigm of (externally tunable) criticality is the mean field theory of magnetism. This theory, a classic developed by Ginzburg and Landau, is based fundamentally on symmetry principles. So, can such an approach be developed here?

Yes, it can by a model first proposed by Hwa and Kardar [109], and further developed by Diamond and Hahm [110], which evolves an order parameter $\delta P = P - P_{\rm SOC}$, *the local excess or deficit of a profile density* P *relative to the SOC profile density* $P_{\rm SOC}$. The situation is shown in Fig. 34, where the dashed line is the SOC profile, the solid line is the full profile, and both excesses and deficits are manifested. If the dynamic is conservative, then δP, the order parameter, should satisfy

$$\partial_t \delta P + \partial_x \Gamma(\delta P) - D_0 \partial_x^2 \delta P = \tilde{S}. \qquad (32)$$

This is a conservation equation that includes a flux $\Gamma(\delta P)$ (to be determined), background diffusion and a source $\tilde{S}$. Equation (32) is a simple hydrodynamic equation that states that δP is conserved, up to sources and boundary losses. In higher dimensions, $\partial_x \to \partial_\perp$ and $\partial_\parallel$, and $D_{\perp 0}\nabla_\perp^2$ and $D_{\parallel 0}\partial_\parallel^2$ enter. The key question is: how can the form of $\Gamma(\delta P)$ be constrained?! This is done by employing the *Principle* of *Joint Reflection Symmetry,* summarized in Fig. 35. The key point is that *blobs,* with $\delta P > 0$ should move down-gradient, to the right. *Voids* with $\delta P < 0$, should move up-gradient, to the left. The Joint Reflection Symmetry Principle states that if one flips the pile orientation, then voids should move

Table 1. Closely related concepts between the sandpile transport model and a turbulent transport model. (Reproduced with permission from Ref. [106], AIP Publishing.)

Turbulent transport in toroidal plasmas	Sandpile model
Localized fluctuation (eddy)	Grid site (cell)
Local turbulence mechanism:	*Automata rules:*
Critical gradient for local instability	Critical sandpile slope (Z_{crit})
Local eddy-induced transport	Number of grains moved if unstable (N_f)
Total energy/particle content	Total number of grains (total mass)
Heating noise/background fluctuations	Random rain of grains
Energy/particle flux	Sand flux
Mean temperature/density profiles	Average slope of sandpile
Transport event	Avalanche
Sheared electric field	Sheared flow (sheared wind)

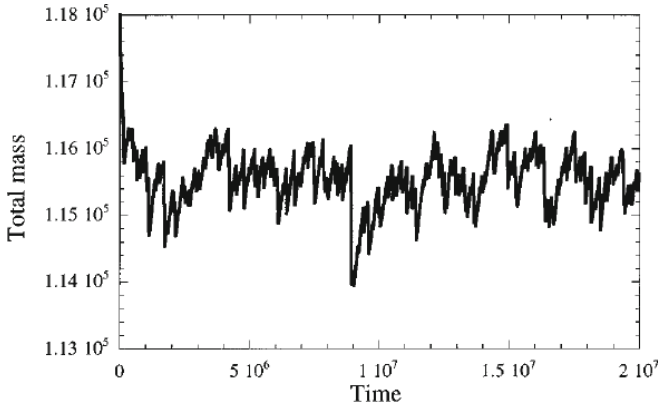

Fig. 33. Time history of total grain content. (Reproduced with permission from Ref. [105], AIP Publishing.)

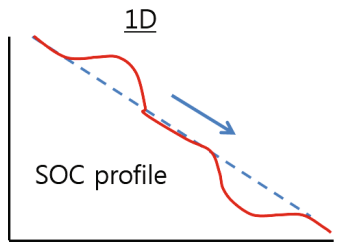

Fig. 34. (Color online) Local excess and deficit of a profile density relative to the SOC profile. (Reproduced with permission from Ref. [94].)

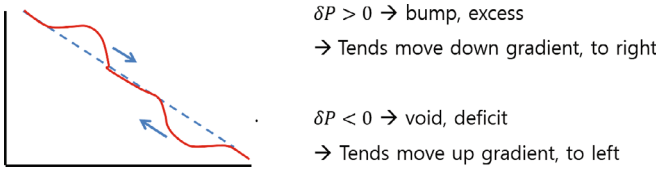

Fig. 35. (Color online) Summary of Joint Reflection Symmetry. (Reproduced with permission from Ref. [94].)

right and blobs left. This is equivalent to requiring that $\Gamma(\delta P)$ be unchanged under $x \to -x$ and $\delta P \to -\delta P$. This forces considerable simplification of $\Gamma(\delta P)$. Specifically, a general $\Gamma(\delta P)$ can be expanded in the following form

$$\Gamma(\delta P) = \sum_{m,n,q,r,\alpha} \{A_n(\delta P)^n + B_m(\partial_x \delta P)^m + D_\alpha(\partial_x^2 \delta P)^\alpha + C_{q,r}(\delta P)^q(\partial_x \delta P)^r + \cdots\}. \quad (33)$$

The lowest-order, smoothest $\Gamma(\delta P)$ (*i.e.* least sensitive to fine scales) that satisfies JRS is

$$\Gamma(\delta P) = \alpha \delta P^2 - D\partial_x \delta P, \quad (34)$$

where α and D are coefficients. Note only even powers of δP and even combinations of ∂_x and δP survive. Thus, Eq. (32) reduces to

$$\partial_t \delta P + \partial_x(\alpha \delta P^2 - D\partial_x \delta P) = \tilde{S} \quad (35)$$

— a noisey Burgers equation, where D and D_0 are combined into a single coefficient. Absent noise, this model, of course, has shock solutions, so 'avalanches' are realized here as shocks, shock trains and ultimately shock turbulence. Avalanche turbulence is then modelled as shock turbulence, a system studied quite intensively.

The physics of this simple hydrodynamic model requires some discussion to appreciate. First, note the heuristic correspondence

$$\alpha \delta P^2 \leftrightarrow -\chi\left[\sigma\left(\frac{|\nabla P|}{P} - \frac{1}{L_{p,\mathrm{crit}}}\right)\theta\left[\frac{|\nabla P|}{P} - \frac{1}{L_{p,\mathrm{crit}}}\right]\right]\nabla P, \quad (36)$$

suggesting that the nonlinear flux $\alpha\delta P^2$ can be thought of as a surrogate for a Fickian flux $\Gamma_p = -\chi\nabla P$, with (thermal) diffusivity χ proportional to deviation from marginality ($\sigma(|\nabla P|/P - 1/L_{p,\mathrm{crit}})$), with a threshold on-switch $\theta(|\nabla P|/P - 1/L_{p,\mathrm{crit}})$. For instance, see Ref. [29]. In this light, the $\Gamma \sim \alpha\delta P^2$ form tacitly relates the fluctuation intensity to δP, so $I \sim \delta P$ and $\Gamma \sim I\delta P \sim \delta P^2$. This shows that blob and void motion encodes the turbulence pulse dynamics (*i.e.* spreading) associated with evolution of the profile near (self-organized) criticality. Alternatively, from the perspective of conservative advection, we can write for δP, $\partial_t \delta P + \partial_x(V\delta P) - D_0\partial_x^2\delta P = \tilde{s}$. Thus, we see that joint reflection symmetry effectively takes $V \sim \alpha\delta P$, so bigger perturbations go faster, ultimately overtaking and swallowing smaller ones. This trend is reminiscent of the evolution of bubble competition in Rayleigh–Taylor turbulence [111] or coagulation in colloids (Smoluchowski) [112], where a larger, faster structure overtakes and ingests a smaller one. Such a process may be thought of as an "inverse cascade", of sorts. Finally, bandpassed low frequency δP, *i.e.* $\delta P(\omega < \omega_c) \to \langle \delta P \rangle_{\mathrm{low}}$, may be viewed as representing corrugations produced by the self-organization process.

The model developed here can be extended straightforwardly to higher dimensions. An important class of extensions of this model is produced by the introduction of a time delay, as advocated by Kosuga *et al.* [113,114]. This extension builds on intuition developed from the theory of traffic flow and flood waves. The key point is that a time delay between flow or flux and δP can lead to effectively negative diffusion and thus the onset of *jamming instability*. Such jams are proposed as the origin of corrugations, staircases and other quasi-periodic nonlinear structures. Nonlinear analysis of the jamming dynamics is required.

Given the similarity of the model to the noisy Burgers system, it is natural to ask about 'avalanche turbulence'. Analyses indicate that, as a consequence of the conserved

order parameter δP, slow modes result in an infrared divergent turbulent diffusivity. Since $\delta l^2 \sim \gamma_T \delta t$, with $\gamma_T \sim 1/\delta l$, this implies $\delta l \sim \delta t$, *i.e.* ballistic scaling of the response. Such trends suggest persistence, *i.e.* Hurst exponent $H \to 1$. Note that the infrared trends recover self-similarity and non-diffusive scaling. Finally, observe that while this model says much about SOC dynamics, it does not predict the SOC profile.

An interesting complementary approach to the construction of a continuum model exhibiting SOC behavior was proposed by Gil and Sornette (1996) [115]. This approach is notable in that it evolves an order parameter S, which then determines the profile $h(x)$. Here, the fundamental equations are:

$$\frac{\partial S}{\partial t} = \chi \left\{ \mu S + \beta S^3 - S^5 \right\}, \tag{37a}$$

$$\frac{\partial h}{\partial t} = -\frac{\partial F}{\partial x}\left(S, \frac{\partial h}{\partial x}\right) + \Phi, \tag{37b}$$

$$F\left(S, \frac{\partial h}{\partial x}\right) = -\alpha S^2 \frac{\partial h}{\partial x}. \tag{37c}$$

Eq. (37b) is effectively a continuity equation for $h(x)$, the occupation of the pile at x. Here, F is a gradient-dependent flux, and Φ is excitation (*i.e.* fueling, noise). The flux F is defined in Eq. (37c). In this light, S^2 emerges as equivalent to an effective *fluctuation intensity.* Thus, in the Gil–Sornette model, the fluctuation intensity is the order parameter that determines the profile $h(x)$. S evolves according to Eq. (37a). There, $\mu = [(\partial h/\partial x)^2 - (\partial h/\partial x)_c^2]$, which (with $\chi > 0$) represents local linear growth/damping for locally super/sub critical gradients. Here, β can be > 0 or < 0. The interesting case is $\beta > 0$, which can induce local *subcritical instability* for $\mu < 0$. Indeed $\beta > 0$ brings both bistability and hysteresis, both essential elements of 'stick-slip' dynamics associated with SOC evolution. In the Gil–Sornette model, metastable states play a central role in SOC. Interestingly, the order parameter equation is *local*, with site-to-site coupling entering only through the $h(x)$ dependence of μ. The Gil–Sornette model determines $h(x)$, not only the dynamics of fluctuations around it. This comes at the price of more *abinitio* inputs.

An interesting prediction of the model is the pdf of flux amplitudes at the outer boundary, shown in Fig. 36. Note $P(J) \sim M^{-\delta}$, where $\delta \sim 0.7$ and M is the avalanche mass. For large J, note a single characteristic flux scale emerges. This corresponds to the limit where the system discharges via synchronized firing of all the local (nonlinear) oscillators. Such behavior may be relevant to pedestal limit cycle oscillation (LCO) phenomena recently observed on DIII-D [116].

All told, the Gil–Sornette model offers an interesting perspective on why SOC dynamics is generic in nature — and in the transport phenomenology of magnetized plasmas, in particular. *The key is that SOC emerges as a consequence of spatio-temporal coupling of local first-order transitions.* Of course, a spatially-coupled

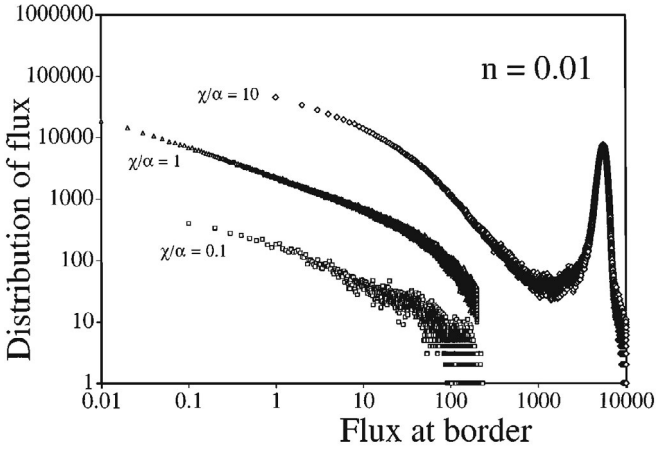

Fig. 36. Distribution $P(J)$ of flux amplitudes at the outer border. (Reproduced with permission from Ref. [115]. Copyright 1996 by the American Physical Society.)

sequence of first-order transport bifurcations defines a complex flux landscape [18, 117] and encodes the complex dynamics of transport. The outcome of this coupling of relaxation oscillators produces spontaneous self-organization by scale-invariant avalanches.

Several interesting extensions of the Gil–Sornette model suggest themselves, as a consequence of issues of relevance to MFE. One is to introduce some elementary spatial coupling of the local order parameter $S(x)$, such as

$$\frac{\partial S}{\partial t} = \text{as before} + \partial_x \Gamma(S, \partial_x S).$$

This is simply the incorporation of turbulence spreading. The critical comparison is that of the spreading length vs. relevant scales in the avalanche distribution. A second extension is to consider two order parameters S_1 and S_2, coupled via the profile (with different parameters). This is a natural way to approach multi-scale dynamics and SOC.

Continuum models are a pivotal element of SOC theory, as they connect the SOC world to the realm of turbulence and transport, and so enable better analysis and understanding.

2. Avalanching and SOC Phenomena in MFE — An Overview

In this section, more direct applications of avalanching and SOC to MFE transport physics are presented. The focus is primarily on simulations and experiments relevant to confinement in relatively simple regimes. The aim is to uncover and understand basic trends in relevant contexts. This section is organized into three subsections:

i) The Sheared Sandpile,

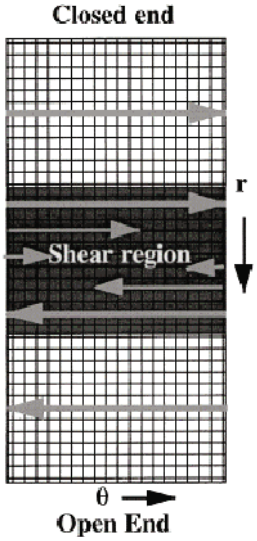

Fig. 37. Sheared sandpile. (Reproduced with permission from Ref. [106], AIP Publishing.)

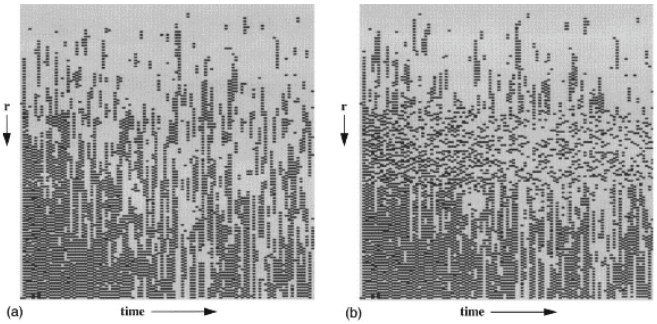

Fig. 38. Effects of shearing on avalanches. (Reproduced with permission from Ref. [106], AIP Publishing.)

ii) Beyond the Box - simulation studies of avalanching, and

iii) Hunting for H (Hurst) in L-mode — fluctuation studies in 'boring' plasmas.

A. The Sheared Sandpile

The sheared sandpile is a natural extension of the elementary sandpile. The model is a 2-D box, periodic in y (θ), with an open and closed end in x (r), as usual. A sheared cross-pile flow in y is specified within a finite layer, *i.e.* $V_y = V_y(x)$ for $a < x < b$. CA rules for toppling in r are as usual, and do not (or, at least, need not) depend on the shearing motion in y. Thus, this model does not incorporate trivial linear shear stabilizing effects, though such details can surely be added. Figure 37 shows the sheared sandpile [106].

Shear is imposed in a finite region as shown, with shear velocity increment $\Delta V \sim V'\Delta$. Figure 38 shows the effects of shearing on avalanches. Figure 38(a) represents avalanching in the absence of shear. Every 50th step is shown. Note the radially-extended and *correlated* regions of overturning activity. These correspond to zones of ongoing avalanching. Figure 38(b) shows the effect of shearing. Note that overturning persists in the region of the shear layer, *i.e. local 'instability' persists, but avalanche coherence in radius is clearly broken.* The latter is evident from Fig. 38(b). There, the avalanches appear as if they have been run through a multi-bladed guillotine. This conclusion is further supported by examination of Fig. 39, which compares the frequency spectra of overturnings with and without the shear layer. Switching on the shear results in a *decrease* — by nearly an order of magnitude — in the power in the lowest frequencies, which correspond to 'Noah' events, *i.e.* large-scale discharges of the pile. At the same time, the very highest frequency power content *increases.* Thus, shearing tends to suppress the largest discharge events, which carry most of the flux. A plot of the *effective* diffusivity in Fig. 40, obtained from grain balance (akin to power balance), shows that $D_{\rm eff}$ decreases rapidly with increasing shear velocity increment ΔV.

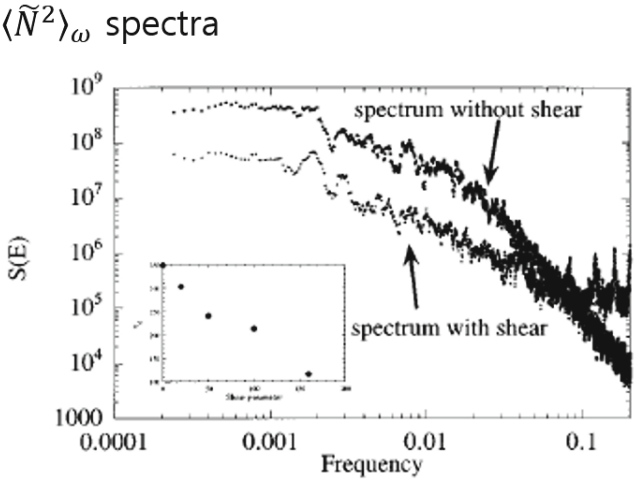

Fig. 39. Frequency spectra of overturnings with and without the shear layer. (Reproduced with permission from Ref. [106], AIP Publishing.)

Several other sandpile model extensions oriented toward MFE applications, especially transport barrier physics, have been developed. One class of these is the so-called 'bistable sandpile,' which uses bistable toppling rules to study the process of barrier build-up as a sequence of local transport bifurcations. The formation of an edge pedestal, which builds inward from the edge, is observed. The pedestal is triggered at the outer pile boundary, as that is the point where the local gradient is steepest (emerging naturally in a pile model, as noted above), and so is the point where the transport bifurcation is triggered. Adding additional physics, such as ambient diffusion and an upper hard profile gradient limit

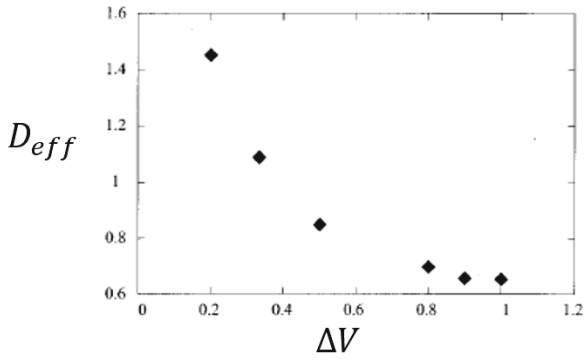

Fig. 40. Dependence of effective diffusivity on shearing. (Reproduced with permission from Ref. [106], AIP Publishing.)

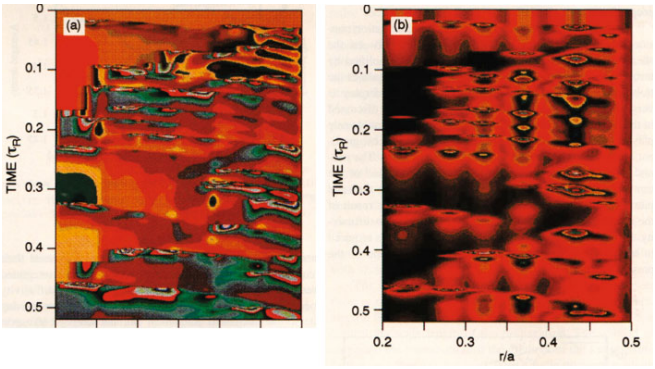

Fig. 41. (Color online) Pressure contours and potential contours showing avalanches. (Reproduced with permission from Ref. [119], AIP Publishing.)

(from MHD stability), recovers cyclic relaxation events, reminiscent of edge-localized modes (ELMs) [107,108].

The bistable sandpile class of models has been used for the exploration of practical questions, such as ELM mitigation. In particular, T. Rhee *et al.* [118] explored ELM mitigation by supersonic molecular beam injection (SMBI). Bistable sandpile model studies indicate that grain injection into the pedestal can break up avalanches, and thus reduce the size of global pedestal discharges, which resemble ELMs. The model studies also identified a 'sweet spot' — a deposition point and deposition size — that is optimal for ELM mitigation. The optimal depth prediction is in semi-quantitative agreement with experimental results.

B. Beyond the Box — Simulation Studies in MFE

At this point, a reader from MFE will surely be thinking: "Why don't these guys think outside the (sand)box and do 'real science'?" Thus, we discuss continuum simulations. A classic series of basic simulations of flux-driven resistive interchange turbulence were presented by

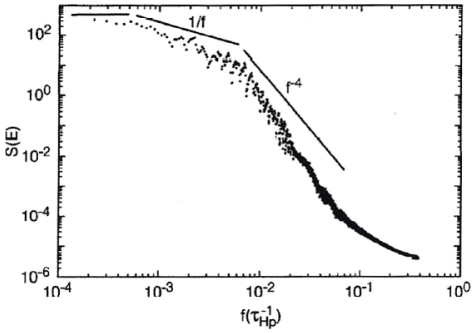

Fig. 42. Frequency spectrum of the simulation. (Reproduced with permission from Ref. [119], AIP Publishing.)

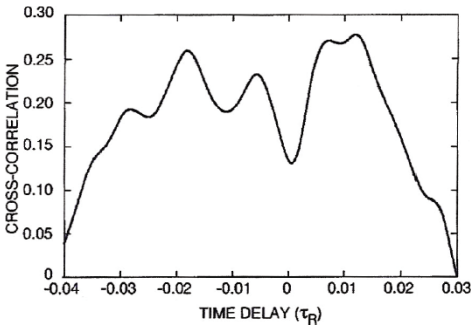

Fig. 43. Cross-correlation of low-frequency modulation. (Reproduced with permission from Ref. [119], AIP Publishing.)

Carreras *et al.* [119]. These defined several key elements of relevant simulation approach, including:

i) Flux drive in which the gradient is allowed to evolve dynamically on fast time scales. To this end, note that ultimately $V_{\rm avalanche} \leq V_*$.

ii) A source profile, including noise, *i.e.* $S_0 = S(r)+\tilde{S}$.

iii) A local stability threshold, set by ∇P, field line bending and collisional viscosity, and thermal diffusivity.

iv) Reynolds stress-driven flows opposed by viscosity.

The results of this study include the clear identification of avalanches, as shown in Fig. 41. Figure 41(b) shows contours of $(e\phi/T)_{\rm rms}$, with mode localization at resonant surfaces clearly evident. However, the pressure contours in Fig. 41(a) show events propagating in radius (note the slopes!) over time. These indicate *avalanches.* These emerge in δP and may be thought of as intermittent collective transport events. Comparison of Figs. 41(a) and (b) shows that such events involve the collective intersections of several modes. Figure 42 shows the frequency spectrum $\langle (e\phi/T)^2 \rangle_\omega$. A $1/f$ region appears and also occurs in the frequency decomposition of the flux $\langle \tilde{v}_r \tilde{p} \rangle_\omega$. This trend is reminiscent of the 'toy' sandpile model. Further evidence for the existence and

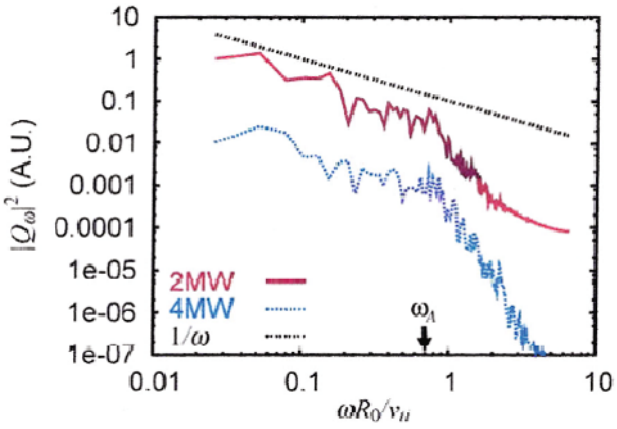

Fig. 44. (Color online) Frequency spectrum of the heat flux from gyrokinetic simulation. (Reproduced with permission from Ref. [126]. Copyright 2009 IAEA, Vienna.)

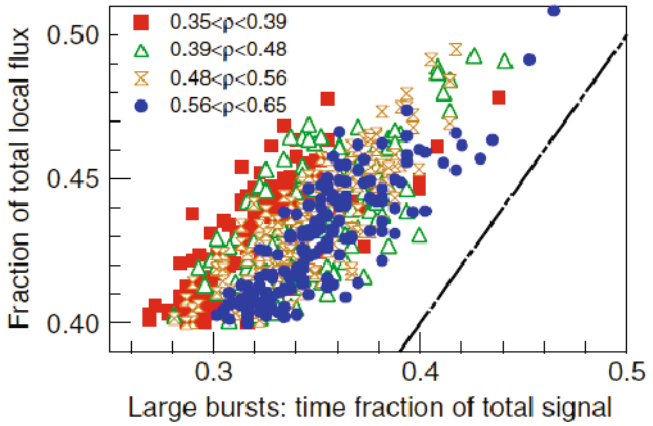

Fig. 45. (Color online) Fraction of the local radial turbulent heat flux carried out by a certain fraction of the largest scale bursts (GYSELA data [130]). Each point represents one specific radial location. The colours distinguish four radial domains. The considered time-series ranges from $\omega_{c0}t = 56,000$ to $\omega_{c0}t = 163,000$. (Reproduced with permission from Ref. [130]. Copyright 2011 IAEA, Vienna.)

dynamics of avalanches appears in the cross-correlation of low frequency modulations, as shown in Fig. 43. Note the existence of two peaks, one with negative time delay and one with a positive time delay. This may suggest the co-existence of both incoming and outgoing avalanches. Studies with the resistive interchange model also indicate that shear flow can truncate avalanches, as in the case of the sheared sandpile. Finally, note that avalanching was most prominent near marginality, as defined by the parameters S, γ, D_0, χ_0, and system size and structure.

While reduced fluid simulations are perfectly adequate for exploring the basic physics of avalanching and spreading [106,119–123], and considerable analytic progress has been made in explicit calculation of momentum flux PDF [124], the focus of computational studies shifted to gyrokinetics. After all, *real* men do gyrokinetics [125]! To address avalanche physics in a meaningful way, gyrokinetic simulations should be flux-driven and full-f [126–129]. In practice, this limits studies to ITG turbulence, perhaps with flow coupling. Some key results are shown and discussed here.

Basic results from nonlinear gyrokinetic simulations closely track those of early, simpler fluid studies. Figure 44 from Ref. [126] shows the frequency spectrum of the heat flux, which exhibits the usual three ranges of ω^0, ω^{-1} and $\omega^{-\alpha}$, $\alpha \gg 1$. Figure 45 from Ref. [130] demonstrates that avalanching does indeed 'matter' — large bursts carry $0.4 \rightarrow 0.5$ of the total local flux. Here 'large' means 0.3 - 0.5 of the total flux. Interestingly, the distribution of flux excursion and $\tilde{v}_r$ demonstrate contrasting symmetries. Figure 46 from Ref. [131] shows the PDF of $\delta Q/Q$ and $\delta v_{\mathrm{E},r}/\langle \delta v_{\mathrm{E},r} \rangle_{\mathrm{rms}}$. Note the former is clearly asymmetric, skewed and with a tail for large positive $\delta Q/Q$. This suggests that large events carry a significant fraction of the heat flux, in accord with Fig. 45. However, the PDF of $\delta v_{\mathrm{E},r}/\langle \delta v_{\mathrm{E},r} \rangle_{\mathrm{rms}}$ is symmetric and has tails that are only slightly fattened. Notably, the autocorrelation of the electrostatic potential or density fluctuations often exhibits two distinctive radial scales. In addition to the microscale $l_c \sim 5 - 8\rho_s$ of the local turbulence, which is observed in most simulations [132,133] and experiments [45,46], there exists a structure indicative of the mesoscale activity associated with the transport events. This co-existence of two different characteristic radial scales of turbulence has been reported in various contexts from both experiments [12, 134] and simulations [55,135–137].

One of the important features that distinguishes results of FD (flux-driven) simulations from those of GD (gradient-driven) simulations is that a significant amount of heat flux is carried by large-scale transport events (which are bursty in time). Consequently, the instantaneous heat flux can significantly exceed the time average value, and it can lead to a transient local decrease of the radial gradient of pressure below a critical value. Results from GT5D gyrokinetic simulations [126] are shown in Fig. 47. Both Q_i and R/L_{T_i} vary in time with a significant but temporary deviation from their average values respectively. In particular, R/L_{T_i} can stay at a subcritical value for a substantial time.

In MFE systems, transport occurs in multiple channels, though one usually carries the driving flux. FD gyrokinetic simulations addressing physics of intrinsic rotation profile formation have been performed using XGC1 and GYSELA codes [138]. Both simulations exhibit coupling and interplay between avalanching transport of ion heat, transport of toroidal momentum and turbulence spreading. Despite differences in computational methods, profiles used and simulation parameters, simulations from both codes report that avalanches of positive heat flux, which propagate either outwards or inwards, are correlated with avalanches of (negative) toroidal momentum flux, so that the outward transport of heat and

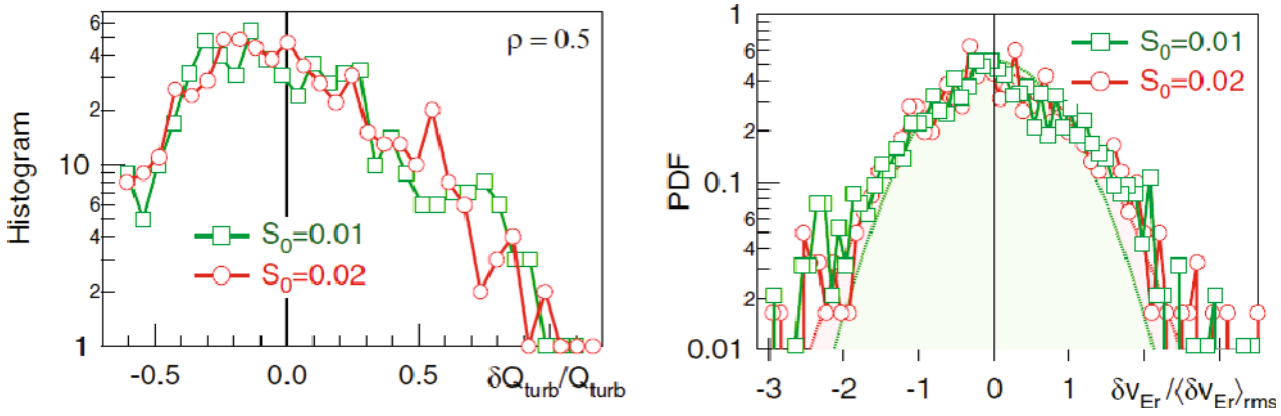

Fig. 46. (Color online) (Left) histogram of the turbulent heat flux $Q_{\rm turb}$ at $\rho = 0.5$ for two magnitudes of the source ($\rho_* = 1/64$). $\delta Q_{\rm turb}$ stands for the difference between $Q_{\rm turb}$ and its time average, taken over the entire non-linear saturation phase. (Right) Corresponding PDF of the fluctuations of the radial component of the electric drift. (Reproduced with permission from Ref. [131]. Copyright 2010 IAEA, Vienna.)

inward transport of momentum are correlated and mediated by propagating fluctuation intensity fronts. In addition, PDFs of the (outward) heat flux and the (inward) momentum flux exhibit large tails, $Q > 0$ for heat and $\Pi < 0$ for momentum.

In XGC1 simulations, a steep ion temperature gradient is maintained at the edge, and turbulence intensity increases as a function of minor radius. Therefore, turbulence spreading is inward. The momentum flux is also inward, because it is generated by the turbulence-driven residual stress [139, 140] at the edge, where symmetry breaking is strongest. Momentum flux towards the core gradually strengthens the intrinsic rotation profile in the co-current direction. On the other hand, the ion heat flux is outward. The PDFs of the heat flux $Q = \langle \delta T_i \delta v_r \rangle$, the *negative* of the momentum flux $\langle \delta u_\phi \delta v_r \rangle$ and the turbulence intensity $\langle (|e|\delta\phi/T_e)^2 \rangle$ are very similar, if they are normalized to the standard deviation, as shown in Fig. 7 of Ref. [138]. The detailed spatio-temporal evolution of various quantities of interest is plotted in Fig. 13 of Ref. [138]. This indicates that avalanches transport heat outward. Such bursts of heat flux can induce a transient local increase in the edge fluctuation level, which in turn relaxes by the inward propagation of intensity pulses associated with turbulence spreading [141]. Consequently, the fluctuation intensity fronts produce fronts of residual stress that drive the intrinsic torque. This results in toroidal flow profile evolution.

Unlike XGC1 simulations, in which a steep gradient is maintained near the outer boundary, the profiles used in the GYSELA simulations lead to active turbulence throughout the simulation domain ($0.12 \leq r/a \leq 0.8$). The ρ_* values used in the simulations are 1/298 and 1/512 for XGC1 and GYSELA respectively. The GYSELA simulations exhibit both inward and outward propagation of momentum flux, but always outward flux surface-averaged heat transport. PDFs of heat and momentum fluxes exhibit significant tails, representing large-scale avalanches. This is shown in Fig. 48. The dominance of large-scale transport events can be quantified by the high kurtosis of the PDF, which is defined as

$$\text{Kurtosis}(f) = \frac{\langle (f - \overline{f})^4 \rangle}{\langle (f - \overline{f})^2 \rangle^2} - 3, \tag{38}$$

where $\overline{f}$ is the mean of f. The Kurtosis vanishes for Gaussian f and is positive for flatter distributions, with large tails. The measured values of Kurtosis are approximately 1.67 and 0.52, for the heat flux PDF and the momentum flux PDF, respectively. This is consistent with the more strongly intermittent nature of the observed heat transport. The PDF of the turbulence intensity is similar to that of heat flux. We also note that the PDF of the heat flux is strongly skewed while the PDF of the momentum flux is relatively symmetric. Since turbulence is excited at the center, it allows both outgoing and incoming avalanches. While the heat transport must carry the imposed heat flux (necessarily outward), momentum can propagate both ways, as it is not directly linked to relaxation. Put another way, the heat flux is necessarily and strongly nonlinear in gradient (*i.e.* $Q \sim (1/L_T)^\alpha$, $\alpha > 1$), on account of the gradient dependence of the ITG threshold and intensity. However, the momentum flux nonlinearity is weaker. The observation of inward-propagating momentum avalanches from both codes further supports the scenario that a temperature gradient-driven, nondiffusive momentum flux from the residual stress can produce the intrinsic rotation profile. It is noteworthy that a theory based on analogy to a "heat engine" [142] gives a plausible explanation and predicts a scaling of the intrinsic rotation that is proportional to R/L_T [143] or R/L_p [144]. Turbulence spreading can also play an important role in transport modeling of intrinsic rotation [145].

An interesting observation that emerged from gyrokinetic simulations is the apparent imbalance between pop-

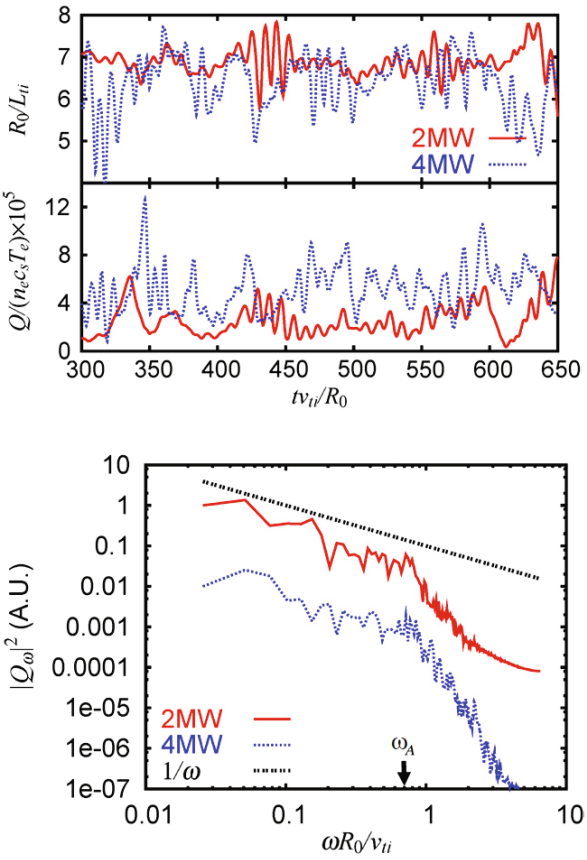

Fig. 47. (Color online) The time histories of the normalized ion temperature gradient R/L_{T_i} and the ion heat flux Q (upper plot), and the power spectrum of Q averaged over source-free regions (lower plot), from a flux-driven ITG turbulence simulation using GT5D code. Note significant deviations of the instantaneous heat flux from the mean value. The power spectra in low frequency region exhibit $1/f$ type spectra. (Reproduced with permission from Ref. [126]. Copyright 2009 IAEA. Vienna.)

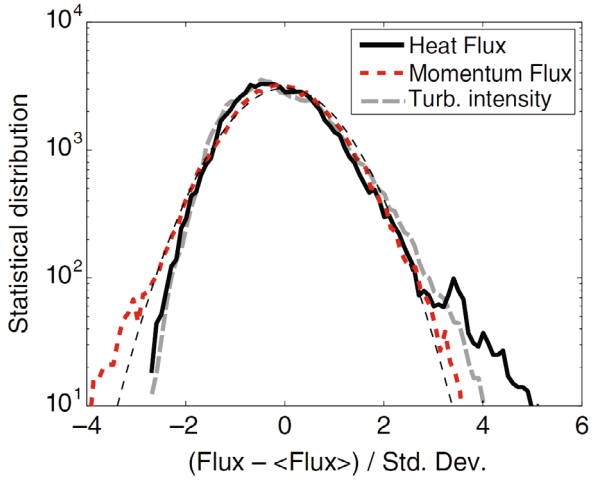

Fig. 48. (Color online) Probability distribution function of heat flux (solid), momentum flux (dotted), and turbulence intensity (dashed) around mid-radius $r/a = 0.5$ in GYSELA simulation with finite rotation. A Gaussian fit is also plotted for comparison. (Reproduced with permission from Ref. [138]. Copyright 2012 IAEA, Vienna.)

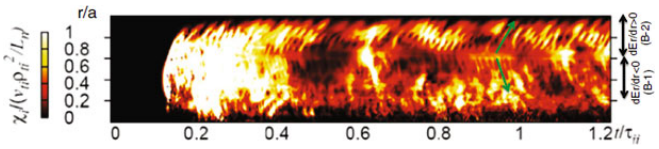

Fig. 49. (Color online) Imbalance between populations of blobs and voids from gyrokinetic simulation. (Reproduced with permission from Ref. [126]. Copyright 2009 IAEA, Vienna.)

ulations of blobs and voids. This appears in Fig. 49, which shows predominantly outward propagating blobs for $E_r' > 0$, with mainly inward propagating voids for $E_r' < 0$. The trend of this imbalance is explained in Fig. 50. The key elements are:

a) Some type of E × B shear stabilization effect, which depends only upon the *magnitude* of the shear $|E_r'|$.

b) The realization that radial force balance relates E_r' to local T_i curvature, *i.e.*, $E_r' \sim T_i''/q$, assuming n is unchanged. Here q is the charge.

Thus, as shown in left panel of Fig. 50, for positive $|E_r'|$, *voids* enhance $|E_r'|$ while blobs weaken $|E_r'|$. Hence, shear stabilization is weaker for blobs, so they dominate the population. In contrast, right panel of Fig. 50 shows that for negative E_r', *voids weaken* $|E_r'|$, while blobs enhance it. Thus, voids dominate for $E_r' < 0$. Note this explanation is based on the assumption of proximity to a *linear* $E \times B$ shear stability boundary. These results are reinforced by more recent GKNET simulations shown in Fig. 51 [147].

A related study using GKNET simulations [148] has demonstrated an approximate balance between outward heat transport events and inward transport events, except for an excess of a few large-scale outward transport events. This suggests that the net outward flux is carried by a few large avalanches, in support of other results (compare Figs. 52 and 53). Figure 52 compares the populations of heat flux events in 'bursty' (*i.e.* active) phases with those in 'quiescent' (*i.e.* inactive) phases. Note for the latter, the populations of positive and negative flux events are rougly equal. However, a clear excess of large flux avalanches (*i.e.* heat 'slugs', or 'blobs') occurs in the bursty phase, during which significant transport occurs. Figure 53 gives more general information concerning the avalanche PDF. The implication of this study is — once again — that heat flux is concentrated in a few large events.

Gyrokinetic studies of avalanches, SOC and turbulence spreading are ongoing. A particular focus is on formation of E × B staircase pattern structures, discussed in

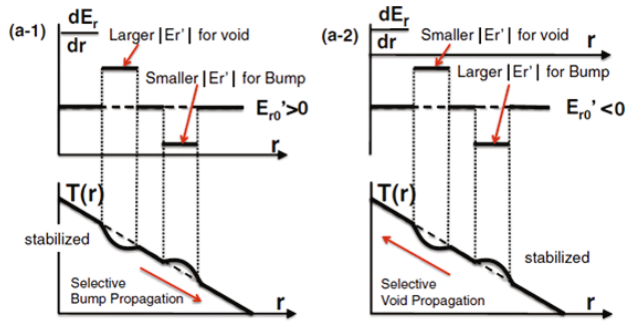

Fig. 50. (Color online) Explanation of the imbalance between populations of blobs and voids. (Reproduced with permission from Ref. [146]. Copyright 2012 by the American Physical Society.)

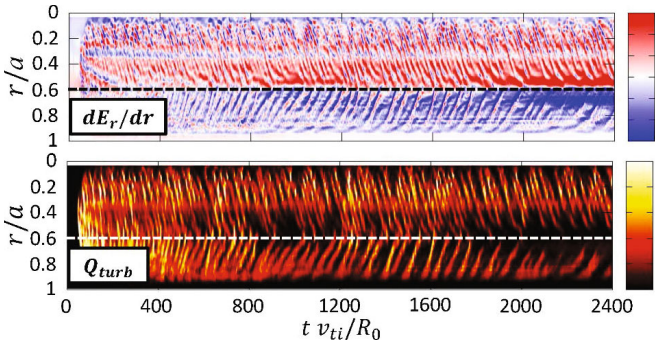

Fig. 51. (Color online) Spatio-temporal evolution of E × B flow shear (upper) and turbulent heat flux (lower) in the case with co-input around $r = 0.6a$ from GKNET simulations. (Reproduced with permission from Ref. [147].)

Sec. IV.

C. Searching for H in L-mode Plasmas

Here, we discuss experimental evidence for avalanching and SOC dynamics. At the outset, it should be stated that studies of these phenomena are part of the larger topic of Nonlocality Phenomena, which has been overviewed by K. Ida *et al.* [150]. Here, we discuss only a few selected aspects of the experimental results to date.

Several studies of the Hurst exponent for edge turbulence in 'boring' plasmas have been carried out, primarily using data from Langmuir probes. The direct imaging of avalanches is beyond current diagnostic capabilities.

Table 2 from Ref. [151] shows results from the analysis for several devices. Note that $H \sim 0.7$ (*i.e.* persistence, as in avalanches) is a general outcome, and that only one device reported $H \sim 0.5$ (this is a small device with a weak magnetic field, and insufficient scale separation between ρ and a). The value of H reported suggests avalanching, as $0.5 < H < 1$ indicates persistence in the dynamics. Figure 54 shows an $I_{\rm sat}$ spectrum ($\langle \tilde{I_{\rm sat}} \rangle_\omega$)

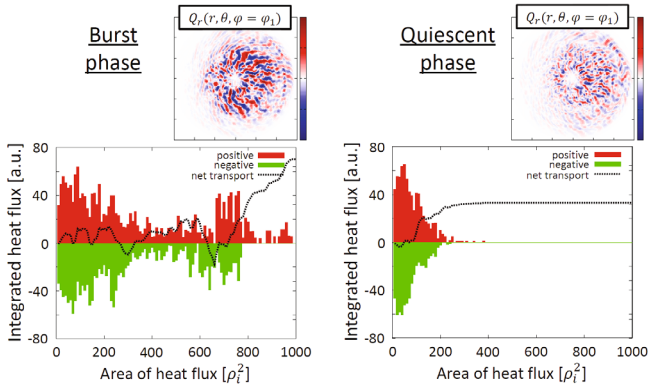

Fig. 52. (Color online) Large transport events are dominant heat carriers? (Reproduced with permission from Ref. [148].)

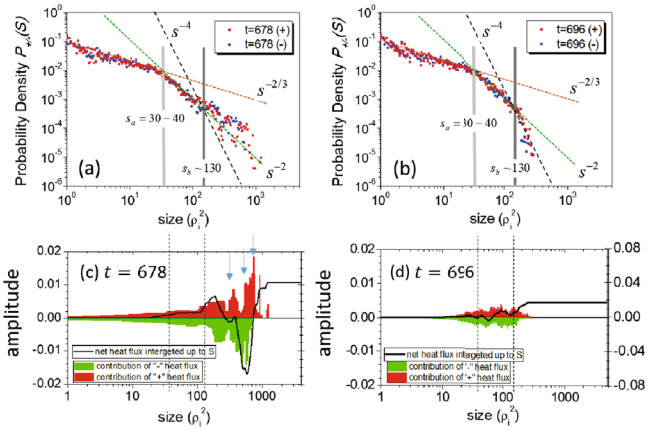

Fig. 53. (Color online) PDFs of transport events at a bursty phase, $t = 678$ (a) and at a quiescent phase, $t = 696$ (b). These are plotted with both positive (+) and negative (−) structures' contributions to heat flux and associated net heat flux at a bursty phase (c) and at a quiescent phase (d). (Reproduced with permission from Ref. [149].)

from W7-AS. Note the familiar structure of an ω^0 range (Noah events), an ω^{-1} range ($1/f$ noise) and an ω^{-4} range, as we have seen already many times in piles, fluid models and full-f, flux-driven toroidal gyrokinetic simulations. Evidence for universality of the $1/f$ range is overwhelming.

We remark, here, that little in the way of experimental studies of flow shear effects on the Hurst exponent or studies of the correlation of trends in confinement with the behavior of H is available. Such results would be of interest in understanding SOC dynamics deeper.

D. Experimental Evidence for Avalanches

Avalanche-like electron heat transport events have been measured on DIII-D tokamak plasmas using electron cyclotron emission (ECE) [152]. The characteristic

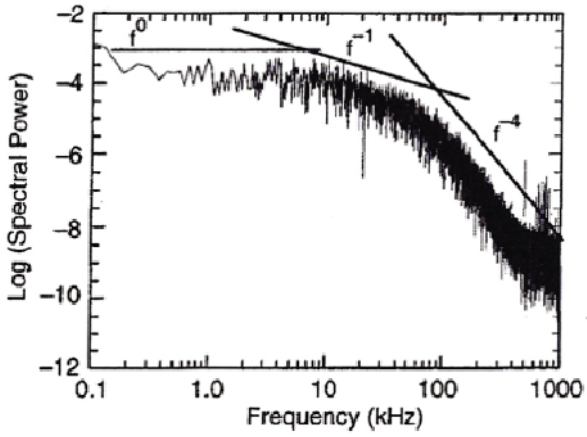

Fig. 54. $I_{\rm sat}$ spectrum from W7-AS. (Reproduced with permission from Ref. [151], AIP Publishing.)

Table 2. $H \approx 0.7$ is a general trend. (Reproduced with permission from Ref. [151], AIP Publishing.)

Device	Number of time series	$\langle H\rangle_{in}$	$\langle H\rangle_{out}$	τ_D (μs)	Self-similarity range (ms)
TJ-I	9	0.64 ± 0.03	0.70 ± 0.04	3.0	0.02 - 1.0
JET limiter	4	···	0.52 ± 0.04	29.0	0.1 - 2.0
JET divertor	4	···	0.63 ± 0.03	19.0	0.1 - 2.0
TJ-IU	21	0.64 ± 0.03	0.67 ± 0.01	6.0	0.1 - 2.0
W7-AS $\iota_a = 0.243$	24	0.62 ± 0.01	0.60 ± 0.04	20.0	1 - 20
W7-AS $\iota_a = 0.355$	29	0.72 ± 0.07	0.66 ± 0.06	19.0	1 - 20
ATF	20	0.71 ± 0.03	0.92 ± 0.07	34.0	1 - 12
RFX	29	0.69 ± 0.04	···	3	0.03 - 3.0
Thorello	10	0.55 ± 0.04	···	6	0.05 - 5.0

velocity estimated from the two-point cross-correlation of electron temperature fluctuations is on the order of 10^2 m/sec in the core and 10^3 m/sec near the edge. This is much faster than the usual gyro-Bohm diffusion over a macroscopic length. In addition, inward propagating avalanches with negative characteristic velocity have been observed near the plasma center [153]. More recently, ECRH has been applied to a KSTAR L-mode plasma with a resonant layer located outside the $q = 2$ flux suface. The spatio-temporal evolution of the electron temperature profile has been measured by the 1D electron cyclotron emission (ECE) diagnostics. The relative electron temperature fluctuations $\delta T_e = (T_e - \langle T_e\rangle)/\langle T_e\rangle$ at different radii are plotted as functions of time in Fig. 55(a). Here, $\langle\cdots\rangle$ is the time average. Figure 55(b) shows the time evolution of δT_e at four different ECE channels. Over a broad radial region, it was observed that bumps with $\delta T_e > 0$ propagate

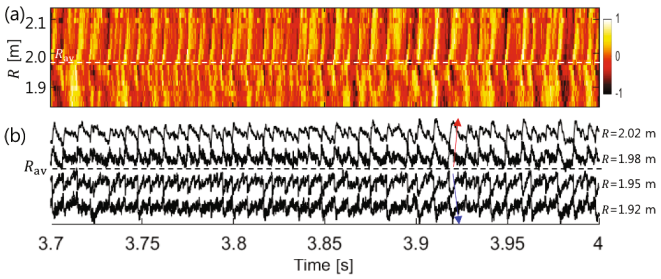

Fig. 55. (Color online) (a) The spatio-temporal pattern of the normalized electron temperature fluctuation in the $z_{\rm ECRH} > z_{q=2}$ period. (b) The rescaled normalized electron temperature fluctuations measured at four different Rs. Bumps ($\delta T_e > 0$) propagate outwards in $R > R_{\rm av}$ (downhill) and voids ($\delta T_e < 0$) propagate inwards in $R < R_{\rm av}$ (uphill). (Reproduced with permission from [154].)

outward while voids with $\delta T_e < 0$ move inward, respectively. This is the first experimental evidence from tokamak plasma core [154] of the joint reflection symmetry (JRS), which is a property expected for a SOC system [109,110]. The radial propagation speed is estimated to be around 30 - 100 m/sec.

Turbulence and transport in tokamak edge near the last closed flux surface (LCFS) is intermittent and often dominated by contributions from blobs [155]. The PDF of fluctuation amplitudes and particle flux near LCFS measured by various diagnostics show a significant deviation from a Gaussian distribution function. The skewness value is negative inside the LCFS, indicating a dominance of voids (negative fluctuations) or inward transport, and positive outside the LCFS, indicating the dominance of peaks (positive fluctuations) or outward transport. This could also be considered an example of JRS, a symptom of SOC. These are evident from measurements on DIII-D plasmas using Langmuir probes and BES [156], and from NSTX using the gas puff imaging (GPI) [157] and Langmuir probes [158]. In addition, edge turbulence in a biasing experiment on TEXTOR also exhibits avalanche behavior [159]. Detailed gyrofluid simulations of blob dynamics at the edge, including SOL region using GEMR code [160] and analyses using a simple $K - \epsilon$ model based on a continuity equation, have been performed [161]. This work unambiguously shows an essential role of turbulence spreading from the unstable edge region to far SOL region, where there are no radial gradients. Furthermore, turbulence spreading persists in more sophisticated global electromagnetic 3-D edge gyrofluid simulations with self-consistent profile evolution [162].

Another ubiquitously observed phenomenon related to avalanches is pulse propagation observed in perturbed transport experiments. Ballistic propagation of heat pulses (either hot or cold) has been observed from various perturbative experiments on tokamak plasmas [38, 163–167]. These also indicate some limitations of local transport paradigm, which relies on the flux-gradient re-

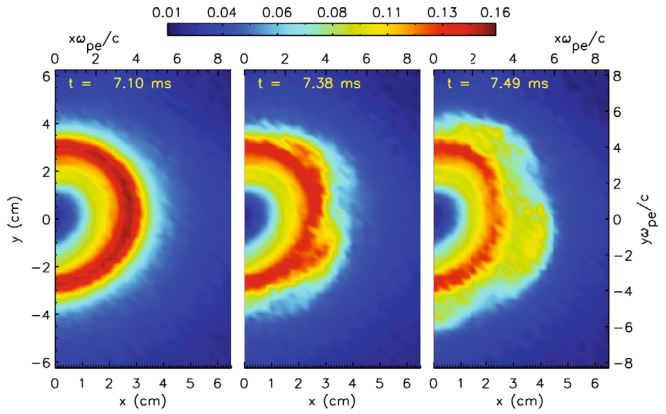

Fig. 56. (Color online) Radial and azimuthal structures of the heated region at three times during one avalanche event: (left panel) before the onset, (middle panel) early stages of profile collapse, and (right panel) late stages of profile collapse. (Reproduced with permission from Ref. [168]. Copyright 2015 by the American Physical Society.)

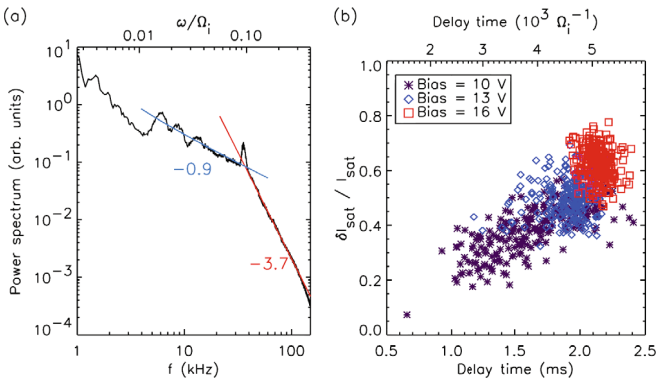

Fig. 57. (Color online) (a) Power spectrum over a time window encompassing 4-6 avalanches and averaged over 500 plasma shots. (b) Statistical behavior of the relative amplitude of a second avalanche and its delay time from an earlier one. Delay time is between the first and second avalanche in each plasma shot, and amplitude is measured relative to the decaying baseline value. Results of three different heating powers are shown. (Reproduced with permission from Ref. [168]. Copyright 2015 by the American Physical Society.)

lation. See review articles for details of this phenomenon [150,165].

Basic experiments, such as those using linear devices, have had little to say about avalanching and SOC, primarily due to constraints on device size and magnetic field do not allow sufficient separation of scales (*i.e.* $\Delta/L_\perp \leq 1$, not $\ll 1$). One study that attempted to address avalanche dynamics was a recent experiment by Compernolle *et al.* on LAPD [168]. This study used a novel heating configuration to excite propagating excitations by driving local gradients until stability thresholds were violated. The excitations then propagated in radius, under the influence of $\mathrm{E}\times\mathrm{B}$ shear. The evolution during an avalanche is shown in Fig. 56. Interestingly, probe ion saturation current spectra again indicate a $\sim 1/f$ range and a $\sim 1/f^4$ range at higher frequencies, though a distinct large event range is absent. This is shown in Fig. 57(a). Figure 57(b) shows a plot of avalanche size vs. delay time between avalanches in the same discharge. A trend of longer delay occuring with larger events is clear. This is reasonable, as longer events will require a longer profile 're-fill time' to build up. The Compernolle *et al.* study [168] does not include statistical analysis. Thus, it leaves open the questions of:

a) Are the transport events under study avalanches or simply large wave packets?

b) Does the experiment achieve a state of overlapping 'avalanche turbulence', as does a stationary, flux-driven system?

Further studies of these and other issues will be of great interest, as would related work on other linear devices.

IV. BRIEF DISCUSSION OF NOTABLE OMISSIONS

This section is necessarily short, and so we must omit or gloss over many interesting and relevant topics. Here, we discuss a few of these, ones we think are most important. These discussions are short and are intended only to serve as guides to further reading and stimuli for further research. Here, we focus on:

i) Kinetics beyond Fokker–Planck

ii) Emergent stationary patterns

iii) Magnetic helicity transport and Taylor Relaxation

1. Kinetics beyond Fokker–Planck

A classic symptom of avalanching is the appearance of a 'fat' or extended tail on the PDF of the flux. Such fat tails are usually power laws (up to a cut-off), in view of mesoscopic scale similarity. Power law tails present a severe challenge to our concept of transport, which is based on Fokker–Planck theory (FPT). Recall that in FPT, the distribution evolves according to a transition probability, as realized by an expansion in the step size (Δx) in phase space, *i.e.*:

$$(1a)\quad f(t+\Delta t) = \int d(\Delta x) T(x,\Delta x,\Delta t) f(x-\Delta x,t)$$

and

$$(1b)\quad \frac{\partial f}{\partial t} = -\frac{\partial}{\partial x}\left\{\frac{\langle \Delta x\rangle f}{\Delta t} - \frac{\partial}{\partial x}\left(\frac{\langle \Delta x\Delta x\rangle f}{2\Delta t}\right)\right\}.$$

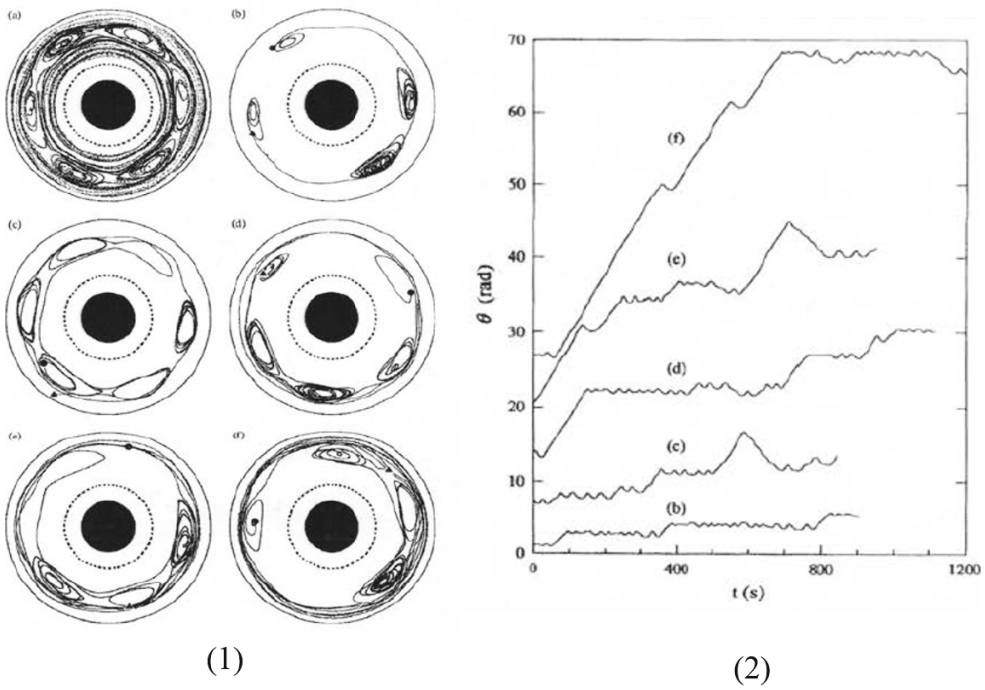

Fig. 58. Vortex array and azimuthal displacement θ. (Reproduced with permission from Ref. [171]. Copyright 1993 by the American Physical Society.)

Here, T is the transition probability of a step of size Δx occuring at location x in time Δt. Equation (1b) is, of course, the time-honoured Fokker–Planck equation. FPT is based on two notable assumptions:

1) The existence of the variance of T — *i.e.* $\langle \Delta x^2 \rangle$ being finite

2) The distribution of time steps Δt being regular.

For (boring) Gaussian distributions, the variance $\langle \Delta x^2 \rangle$ converges. For power laws of the form $P(\Delta x) \sim c/(\Delta x)^{1+\alpha}$, $\langle (\Delta x)^2 \rangle$ diverges (or depends explicitly on its large scale cut-off — *i.e.* as for Bohm scaling) for $\alpha \leq 2$, indicating a breakdown of FPT. This is indeed to be expected for avalanches. Likewise, irregular Δt, suggestive of, say, sticking for a long time at a particular position or an anomalously long time step, also leads to a breakdown. In general terms, transport processes that do not fit nicely into the FPT are 'flights' (especially Levy flights) or 'sticky' random walks, rather than diffusion. These must be described using a generalization of the familiar Gaussian distribution, namely the *Pareto–Levy distribution.*

The beloved Gaussian is only one of an infinite number of stable probability distribution functions and the only case with a finite variance. These are called Pareto–Levy (PL) distributions, after Wilfredo Pareto and Paul Levy. It is more convenient to work with the generating function (*i.e.* essentially, the Fourier transform of the transition probability) rather than the distribution, itself. This may be written (for the time independent, and time dependent cases, respectively) as:

$$(2a) \quad P_\alpha(q) = \exp\left[-c|q|^\alpha\right]$$

and

$$(2b) \quad P_\alpha(q,t) = \exp\left[-ct|q|^\alpha\right].$$

Here α is the Levy index α, with $\alpha = 2$ corresponding to a Gaussian distribution (*i.e.* the Fourier transform of a Gaussian is a Gaussian!). For $\alpha = 2$, $c \to D$ (diffusion coefficient), $P(q,t)$ can be used (straightforwardly) to obtain the familiar Green's function for diffusion. $\alpha = 1$ corresponds to a Cauchy distribution, for which the flux-gradient relation

$$(3a) \quad \Gamma = -D\nabla f$$

becomes the non-local relation:

$$(3b) \quad \Gamma(x) = -\int dx'\, d(x,x')\nabla f(x')$$

$$(3c) \quad d(x,x') = S/[(x-x')^2 + \Delta^2].$$

Note that, here, the Lorentzian kernel $d(x,x')$ replaces the diffusion coefficient. In principle, S can be spatially varying, *i.e.* $S \to S(x')$. The Cauchy flux-gradient relation has been demonstrated to be a good fit to the flux-gradient relation in one system where avalanching occurs [169]. For $|\mathbf{x}| \to \infty$,

$$(4) \quad P_\alpha(x,t) \sim t/|x|^{\alpha+1}$$

so an "accelerating tail" distribution develops. This is so named because it maintains constant P for $|x| \sim t^{1/(\alpha+1)}$.

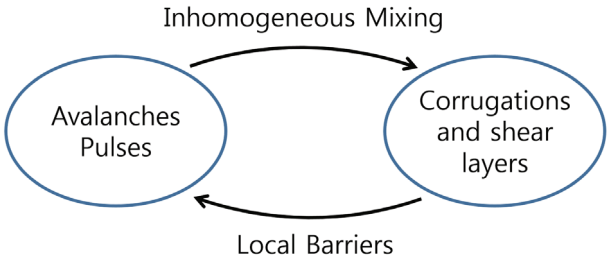

Fig. 59. (Color online) Mesoscopic transport events mix fields inhomogeneously, producing zonal shear barriers and profile corrugations. Local barriers in turn regulate the mesoscale transport.

Table 3. Comparison of FPT and FK

Parameter	Fokker-Planck	Fractional Kinetics
Stochastic variable	Δx	$\Delta x, \Delta t$
Role of time	Fixed clock	Variable clock, PDF steps
Variance	$\langle \lvert x\rvert^2 \rangle \sim t$	$\langle \lvert x\rvert^2 \rangle \sim t^\mu$ where $\mu < 2$
$A(y, \Delta t)$	$\langle\langle(\Delta y)\rangle\rangle$	No simple form
$B(y, \Delta t)$	$\langle\langle(\Delta y)^2\rangle\rangle$	$\frac{\langle\langle \lvert\Delta x\rvert^{\alpha_1}\rangle\rangle}{\Gamma(1+\alpha_1)}$

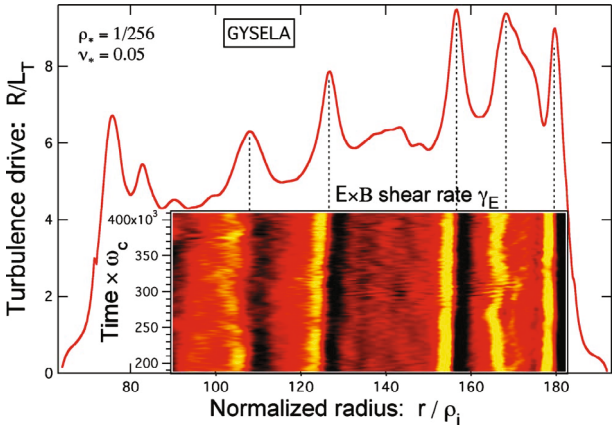

Fig. 60. (Color online) An E × B staircase. Note the regularly spaced corrugations in ∇T_i (*i.e.* local peaks in $1/L_{Ti}$) coincident with E × B shear layers. (Reproduced with permission from Ref. [169]. Copyright 2015 by the American Physical Society.)

The theories of continuous Time Random Walk (CTRW) and Fractional Kinetics (FK) developed by E. Montroll, Y. Klafter, G. Zaskvsky [170] and others, aim to extend the Fokker–Planck approach to Pareto–Levy distributions and so encompass 'fat tail' phenomena, such as avalanching. CTRW theory works by distributing the *time step* Δt according to a fat tailed distribution, allowing prolonged sticking times, longer step intervals, etc., so now $T(x, \Delta x) \to T(x, \Delta x, t, \Delta t)$. A broad distribution of time steps Δt will yield apparently intermittent transport events. Fractional Kinetics (FK) extends the familiar model of smooth infinitesimals Δt, Δx to include rough, fractal distributions, *i.e.*

$$\Delta x \frac{\partial f}{\partial x} \to (\Delta x)^\alpha \frac{\partial^\alpha f}{\partial x^\alpha},$$

like those encountered in turbulence. FK was developed to treat the contribution of accelerator modes to transport in the Standard Map system [170]. The fractal character of the rough distribution implies that the kinetics is *fractional*, as opposed to the familiar diffusive $\langle \delta x^2 \rangle \sim t$, which is a result of smooth, not rough (*i.e.* power law) PDFs.

The technology of CTRW and FK is complicated; a detailed discussion is beyond the scope of this review. Readers are referred to the reviews and books by Klafter and Zaslavsky. Table 3 presents a short summary of a "bottom line" comparison of FPT and FK. There, the exponent μ is set by the critical space–time exponents for the system. Loosely put, A is the counterpart of the drift coefficient and B is the counterpart of diffusion. The scalings of A, B are determined by the scalings of the amplitude and shape of underlying PDF. As always for kinetics, the underlying physical model and distribution of the step determine the outcome.

Amidst this formalism-laden discussion of fractional kinetics, it is natural to ask for some physical insight into what, exactly, is a 'flight' or 'sticky walk'. A classic experiment by Solomon, Weeks and Swinney (SWS) [171] is helpful here. SWS studied test particle dynamics in a rotating laminar flow with a slowly evolving vortex array. The upshot was the observation of strongly super-diffusive behavior, as described in their paper. The vortex array and, most importantly, several realizations of the time evolution of angle θ are shown in Fig. 58[(1),(2)]. The displacement variance scaled as $\langle \delta s^2 \rangle \sim t^{1.6}$, which is super-diffusive. Figure 58(2) shows that this anomalous exponent and scaling results from periods of prolonged sticking of test particles (inactive transport) while orbiting a particular vortex, interspersed by long steps of 'flights' (active transport) between vortices. Flights are analogous to large avalanches, while sticking is analogous to quiet periods, as encountered in simulations. Of course, the step PDF is distorted by sticking and flights, and is strongly non-Gaussian.

CTRW and FK methods have been applied to confinement-related problems [21,172]. Usually, the approach is to compare transport data from simulation to FK predictions made *using properties of the fluctuation field or step PDF from that simulation.* The question of self-consistency — or more precisely, the physics of feedback of the anomalous scaling events on the dynamics — is as yet poorly understood. In particular, the effect of a self-consistent, spatially varying strength field $S = S(x')$ has not been addressed. Some effort to integrate a model of dynamics with one for anomalous kinetics remains a high priority for research on mesoscopic transport events.

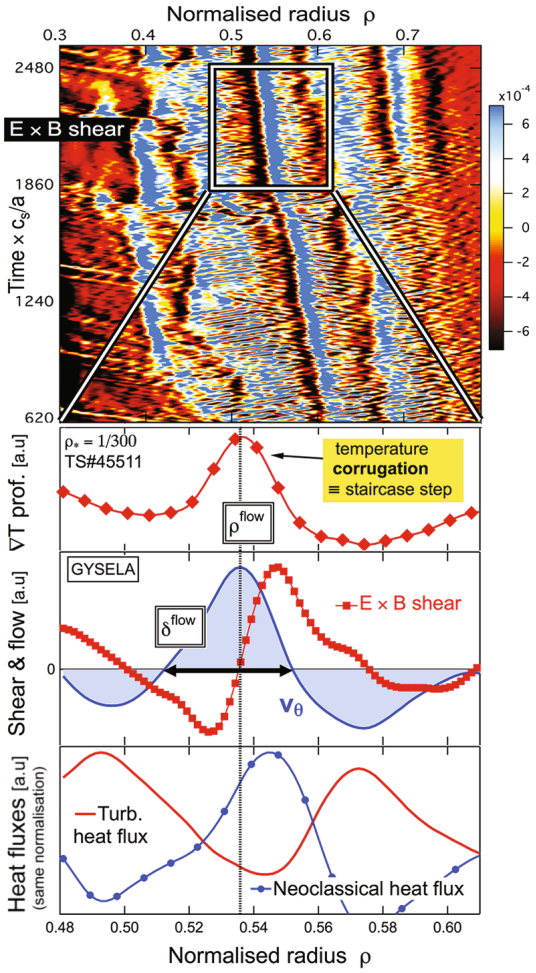

Fig. 61. (Color online) Detail of shear flow–mean profile–transport interplay next to a staircase step [a corrugation]. (Reproduced with permission from Ref. [179]. Copyright 2015 by the American Physical Society.)

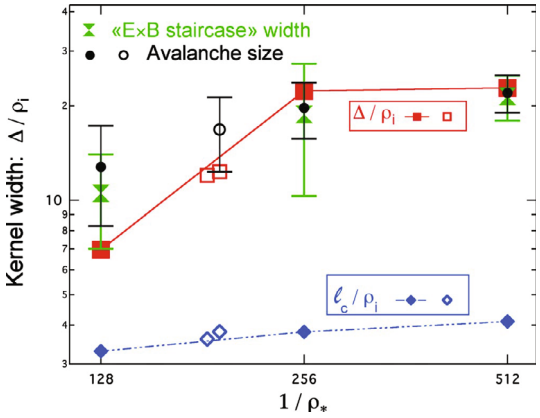

Fig. 62. (Color online) The "influence length" Δ is compared to the turbulence autocorrelation length l_c, the avalanche size and the "E × B staircase" width between the jet-like structures in Fig. 60 (solid symbols, GYSELA; open symbols, XGC1). (Reproduced with permission from Ref. [169]. Copyright 2010 by the American Physical Society.)

2. Quasi-stationary patterns: The E × B Staircase

A. Introduction

Mesoscopic transport events, such as avalanches or turbulence pulses (*i.e.* spreading), necessarily also drive inhomogeneous mixing and transport of potential vorticity [173–175](PV). Potential vorticity may be thought of as effective total charge density for drift wave and QG systems, and so includes a polarization charge contribution. Thus, transport events are strongly coupled to zonal modes [3,176]. Zonal flows are a key element in drift wave turbulence, as they are modes of minimal inertia and damping, and produce no transport ($n = 0$). Thus, zonal modes are a significant energy repository and also a pathway to (very low frequency) dissipation in drift wave turbulence. Avalanches, turbulence pulses and zonal flows are nonlinearly excited mesoscopic structures that co-exist. Zonal flows are more familiar, since they are low frequency and quasi-coherent. Transport events (TE) and zonal flows (ZF) naturally drive and regulate each other. As shown in Fig. 59, TEs drive zonal flows by producing vorticity fluxes and Reynolds forces [177] — and so, PV mixing. But, ZF shears regulate TEs and absorb energy. One is thus strongly motivated to ask: just *how* these two competing secondary structures coexist, and *what types* of *system states result?*

B. Phenomenology: Digital and Analogue

The answer to the question above is still a work in progress. However, one particularly interesting global state of turbulence – shear layer coexistence is the E × B staircase [135,169]. This is a subject of intensive study. The E × B staircase – which resembles the PV staircase well known in geophysical fluids [178] – is a quasi-periodic array of:

i) Domains of active transport with significant levels of turbulence intensity and avalanching, where local profiles relax,

interspersed by:

ii) Zones of reduced transport, where local profiles steepen and shear layers form. These resemble small ITBs.

E × B staircases have been observed in computer simulations, and possibly in one experiments as discussed below. PV staircases have been observed in the atmosphere. Figure 60 shows an E × B staircase as observed in a flux-driven gyrokinetic simulation of ITG turbulence. Figure 61 shows a related space–time image of staircase evolution.

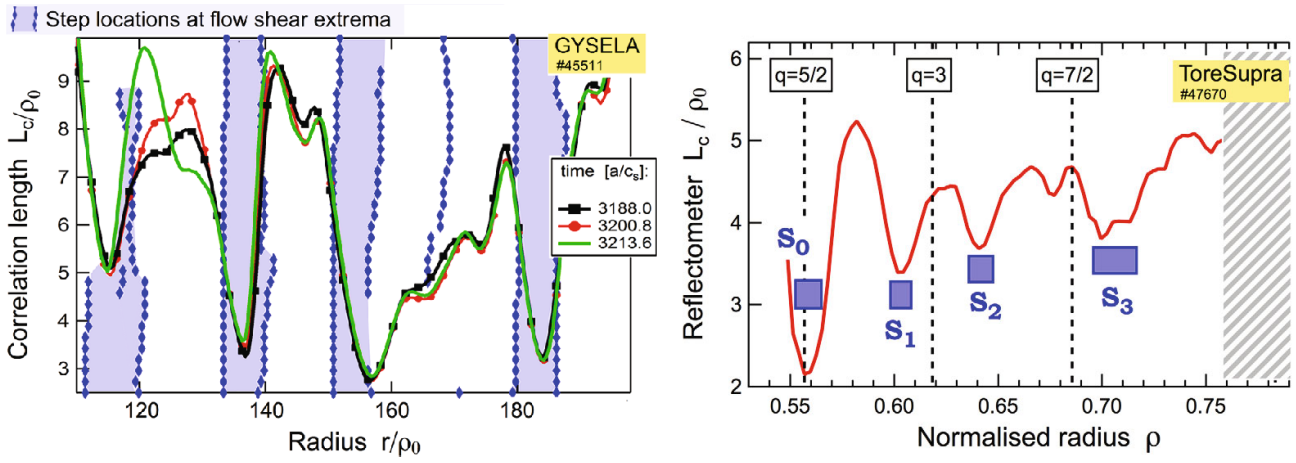

Fig. 63. (Color online) (a) Local minima of the radial correlation length of the turbulent fluctuations at three different times efficiently track the staircase steps in GYSELA. (b) The reflectometer coherence length plotted against radius shows clear experimental evidence of a staircase at locations S_1, S_2 and S_3, possibly also at S_0. (Reproduced with permission from Ref. [179]. Copyright 2015 by the American Physical Society.)

The E × B staircase solves the problem of TE–ZF coexistence by separating these 'phases' of the system into distinct, albeit adjacent, domains. In this sense, the staircase state may be thought of as a spontaneous 'spinodal decomposition' of drift wave turbulence. The spacings between mini-barriers sets the scale of the active domains, and thus the outer scale of the avalanche distribution. The configuration is thus a mesoscopic, self-regulating state. Figure 62 shows the properties of avalanches in an E × B staircase. That study suggested a *non-local kernel* to relate heat flux to gradient, *i.e.*

$$Q = -\chi \nabla T \quad \rightarrow \quad -\int dr' d(r,r') \nabla T(r'), \qquad (39)$$

where

$$d(r,r') \simeq S/[\Delta^2 + (r-r')^2], \qquad (40)$$

i.e. a Cauchy distribution. Figure 62 compares the turbulence correlation length l_c (as l_c/ρ_i) to the influence length Δ (as Δ/ρ_i), the step width in the staircase and the outer scale of the avalanche distribution. Note that $l_c < \Delta$ and $\Delta \sim l_{\text{outer avalanche}} \sim L_{\text{step}}$. Studies indicate that the staircase configuration is not determined by the location of low q resonances.

Quasi-regular mesoscopic zonal patterns that resemble the staircase have been observed in experiment [179]. Results from simulation are compared with experiment in Figs. 63(a) and (b). Note the quasi-regular spacing of local minima in the fluctuation correlation length plot from GYSELA simulations in Fig. 63(a). This is suggestive of a similar quasi-regular spacing of strong E × B flow shears. Figure 63(b), from reflectometry measurements shows a similar (quasi-regular) spacing of coherence minima. Indeed, this similarity is striking! However, the experiments reported in Ref. [179] are unable to distinguish between a staircase (which involves bistability) and a uni-stable quasi-periodic E × B waveform. Further research is needed to address this challenging question.

C. Theory

To understand the physics of the E × B staircase, a theoretical model is required. Here, we discuss two approaches to staircase formation, both of which involve pattern steepening associated with negative diffusion, as in the Cahn–Hilliard equation. These are:

i) A boundary value approach, wherein a turbulence modulation grows, steepens and saturates ultimately forming a staircase pattern. The key element in this approach – first advocated by Balmforth *et al.* [180] in the context of staircases in stratified fluids – is a bistable, gradient-dependent mixing length. This admits a transport bifurcation, which forms an array of local barriers. This pattern constitutes a staircase.

ii) An initial value approach, wherein a gas of heat avalanches described by a Burgers model, forms a train of local 'jams', which steepen to form a staircase structure. The key element, here, is a time delay between perturbations in heat flux and gradient, much like the time delay between traffic flow velocity and density perturbations due to finite driver reaction time [10]. For large reaction time, the effective diffusivity goes negative, resulting in a 'jamming instability'. In this approach, the Burgers model of avalanches is extended to a nonlinear telegraph equation.

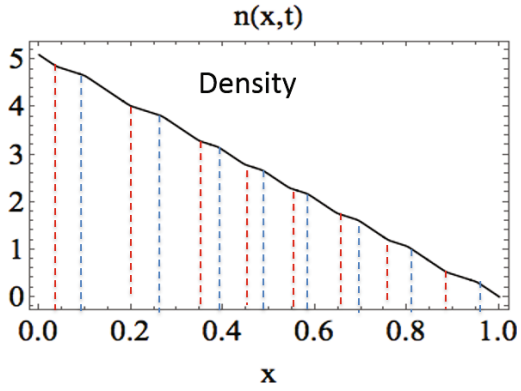

Fig. 64. (Color online) Staircase in mean density profile.

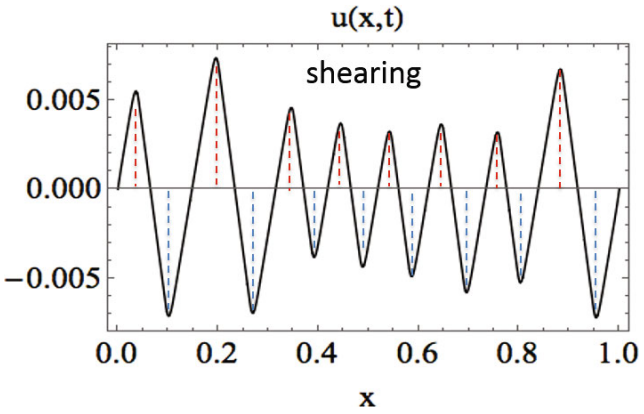

Fig. 65. (Color online) Sequence of mean shear layers related to density staircase.

A simple boundary value approach was implemented for a mean field $K-\epsilon$ type model based on the Hasegawa–Wakatani system [181, 182]. The model evolves mean density n, mean vorticity u and turbulence potential enstrophy ε while conserving total potential enstrophy between mean and fluctuations. Mean fluxes are computed using a gradient-dependent mixing length

$$l_{\rm mix} = l_0/[1 + l_0^2[\partial_x(n-u)]^2/\varepsilon], \qquad (41)$$

which is based on the relative size of the Rhines scale [183] and the characteristic turbulence scale absent sharp gradients. Bistability and inhomogeneous mixing enter via the gradient dependency of $l_{\rm mix}$. Solution of the model yields a staircase in density (Fig. 64), a sequence of sharp shear layers (Fig. 65) and localized zones of turbulence activity coincident with minima in the driving gradient (here, ∇n), as shown in Fig. 66. Note that this exceedingly simple model, which contains nothing more than modulation steepening due to bistability of the mixing process, easily recovers the essential feature of the staircase — namely decomposition of the system into domains of turbulence activity interwoven with mini-barriers. Note also that the staircase is a global state.

Several other interesting features of the staircase are

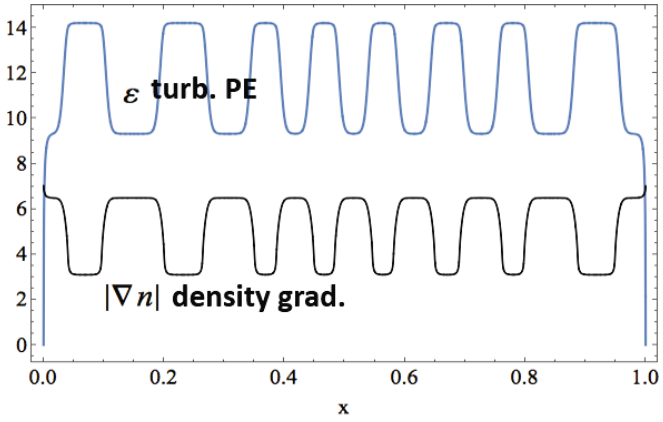

Fig. 66. (Color online) Turbulent potential enstrophy plotted vs density. Note ε peaks where ∇n has a minimum.

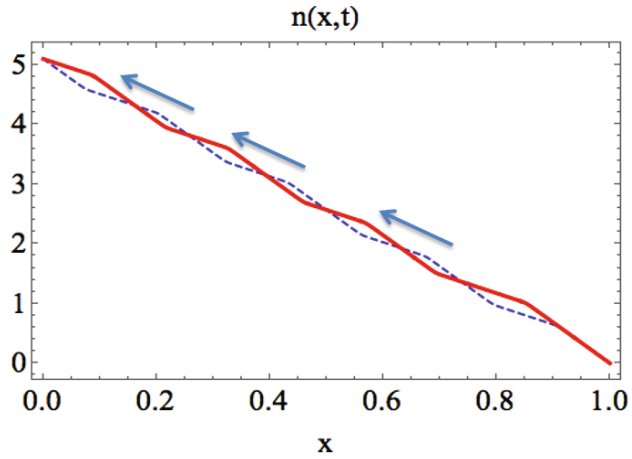

Fig. 67. (Color online) Escalator motion of staircase. (Reproduced with permission from Ref. [181]. Copyright 2016 by the American Physical Society.)

revealed by model studies. These are:

i) Staircases are dynamic - mini-barriers can migrate upward in an 'escalator' pattern. See Fig. 67.

ii) Steps can merge, as do domains in Cahn–Hilliard systems. The number of steps in the staircase tends to decrease over time.

iii) The simultaneous migration and merger of steps can lead to the emergence of a macroscopic barrier, as shown in Fig. 68. In this case, the barrier is an ETB.

iv) Staircases persist for flux-driven systems.

Two additional findings merit special mention. The first is related to the role of turbulence spreading in the model, which is represented by a turbulent diffusion of potential enstrophy. Figure 69 shows that weak spreading leads to a strongly corrugated ('rough') pattern, while strong spreading washes out all but one step.

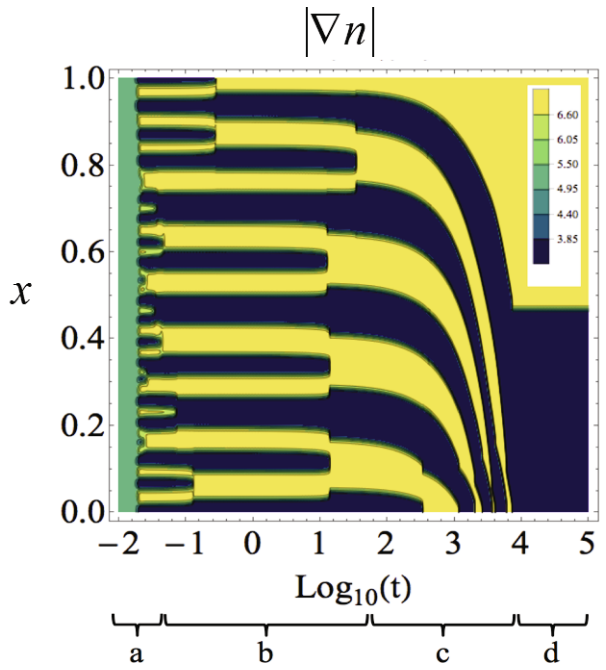

Fig. 68. (Color online) Staircase condenses to form a macro-barrier. (Reproduced with permission from Ref. [181]. Copyright 2016 by the American Physical Society.)

So, for turbulence spreading (TS), we can indeed say a little TS smooths over the roughness, but too much TS washes out the interesting structure. A second important result from the model concerns feedback loops. Interestingly, the Rhines scale feedback mechanism yields staircase formation, while the familiar E × B shear channel does not [184]. This suggests that it is, indeed, the ∇n dependence of $l_{\rm mix}$ that is central to the formation of a staircase. This result is consistent with reports from simulation studies [185]. Further work is required to understand this somewhat counter-intuitive finding.

Another approach to the question of how staircases are formed is based on the idea of jam formation in the gas of heat avalanches [113, 114, 186]. The basic concept is derived from the theory of 1-D traffic flow, for which it is well known that finite-driver reaction time can induce negative effective diffusivity in the concentration of vehicles, causing coagulation and jamming. This, then, drives us to revisit the basic continuum model of avalanching.

The mean field Burgers model of avalanching discussed in Sec. III.1 posits that a slug or avalanche of heat δT evolves according to

$$(2a) \quad \partial_t \delta T = -\partial_x Q,$$

where:

$$(2b) \quad Q = Q_0[\delta T] = (\lambda/2)\delta T^2 - \chi_2 \partial_x \delta T + \chi_4 \partial_x^3 \delta T.$$

Here, a hyper-diffusion has been added, to ensure numerical stability. In this model, any excursion δT from the SOC state directly implies a heat flux $Q_0[\delta T]$. However, any effective 'inertia' in the heat flow will force a time delay, during which the instantaneous heat flux Q relaxes to the value $Q_0[\delta T]$, the mean field value. Thus, Q evolves according to

$$\partial_t Q = -\frac{1}{\tau}\left(Q - Q_0[\delta T]\right),$$

where $\tau = \tau(Q_0, \delta T)$ is the heat flux relaxation time, which causes the time lag between δT and Q. This delay is analogous to the time delay between the instantaneous flux and the quasilinear prediction thereof. Thus, we can expect τ to be comparable to the long wavelength temperature autocorrelation time. As $\tau = \tau(\delta T, Q_0)$, it can be large near criticality, symptomatic of critical slowing down. As a consequence of this reconsideration, the Burgers model of avalanches now becomes a *nonlinear telegraph* model, *i.e.*

$$(3) \quad \partial_t \delta T + \lambda \delta T \partial_x \delta T = \chi_2 \partial_x^2 \delta T - \chi_4 \partial_x^4 \delta T - \tau \delta_t^2 \delta T.$$

To develop intuition for this model, it is useful to systematically revisit the analogy between traffic flow and heat avalanche dynamics. This is set forth in Table 4. One consequence of finite relaxation time is that now

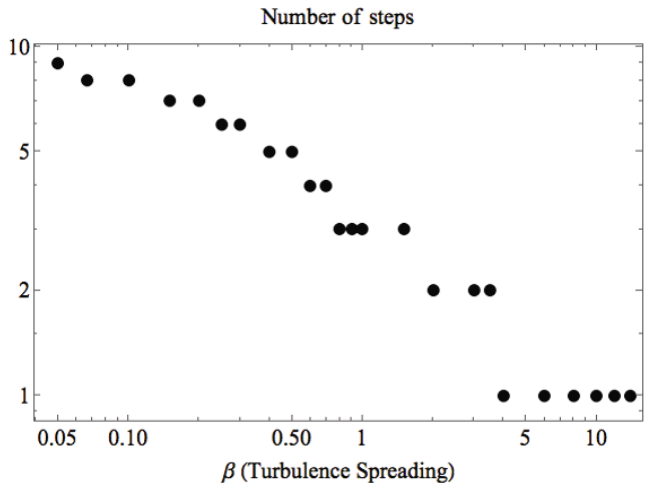

Fig. 69. Increasing spreading washes out the staircase. (Reproduced with permission from Ref. [182], AIP Publishing.)

Table 4. A useful analogy of heat avalanche dynamics and traffic flow dynamics.

heat avalanche dynamics	traffic flow dynamics
temp. deviation from marginal profile	local car density
heat flux	traffic flow
mean SOC flux (ala joint reflection symmetry)	equilibrium, steady traffic flow
heat flux relaxaxtion time	driver's response time

- driver's response can induce traffic jam
- jam in avalanche → profile corrugation → staircase?!?
- Key: instantaneous flux vs. mean flux

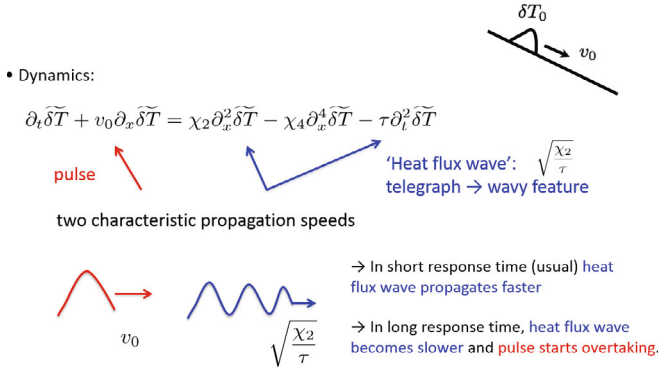

Fig. 70. (Color online) Physics of pulse dynamics.

there are *two* characteristic speeds associated with a heat pulse. One is $v_0 \sim \lambda \delta T_0$, the natural propagation speed of a pulse of size δT_0. The second is $v_{\rm ph} \sim (\chi_2/\tau)^{1/2}$, the phase speed defined by the linear telegraph dynamics of Eq. (3). Indeed, the nonlinear telegraph equation simultaneously manifests two characters of the temperature response, a 'pulse feature', with $v_0 \sim \lambda \delta T_0$ and a 'wavy feature' with $v_{\rm ph} \sim (\chi_2/\tau)^{1/2}$. For a short reaction time, the flux wave propagates faster. For longer reaction times and/or larger pulses, $v_0 \to v_{\rm ph}$, so the pulse speed overtakes the wave speed. At that point, the effective diffusivity in the linearized telegraph equation

$$(4) \quad \partial_t \delta\tilde{T} + v_0 \partial_x \delta\tilde{T} = \chi_2 \partial_x^2 \delta\tilde{T} - \tau \partial_t^2 \delta\tilde{T} - \chi_4 \partial_x^4 \delta\tilde{T} = (\chi_2 - v_0^2 \tau) \partial_x^2 \delta T - \chi_4 \partial_x^4 \delta T. \quad (42)$$

$\chi_{\rm eff} \sim \chi_2 - v_0^2 \tau < 0$, signifying the onset of clustering instability. In this view, we see the heat flux 'jamiton' [187], which is formed as a secondary mode in the gas of primary avalanches. The physics of pulse dynamics is summarized in Fig. 70. A detailed analysis of pulse jamming instability and its regulation by E × B shearing in the nonlinear telegraph model predicts a saturated pulse size $\delta T/T \sim (v_{{\rm Th}i}\rho_i)^{-1}(\chi_4/\tau)^{1/2}$ and a characteristic scale $\Delta \sim (v_{{\rm Th}i}/\lambda T_i)^{1/2}(\rho_i \sqrt{\chi_2 \tau})^{1/2}$. Here Δ defines the effective 'step size' of the staircase — *i.e.* the spacing between jams. Note that Δ is the geometric mean of ρ_i (which defines the correlation scale) and the (Neoclassical) diffusion length in one relaxation time τ. For standard parameters, $\Delta \sim 10\Delta_c$, where Δ_c is the turbulence correlation length.

Further work on the theory of jamming should focus on improving our understanding of $\tau(Q_0, \delta T)$ and especially its behavior near criticality.

D. Where does the staircase lead?

The E × B staircase is of fundamental interest since it is at least one *concrete* realization of the outcome when transport events and zonal flows compete on mesoscales.

Fig. 71. (Color online) Possible replacement of a single ITB layer with a sequence of smaller steps.

This issue is central to the question of the degree of, and the underlying physics of, gyro-Bohm breaking. The staircase resolves the competition by decomposing the drift wave turbulence into active zones interspersed by mini-barriers. The size of the active zones sets an upper bound on the effective mixing length for the system. The staircase is a mesoscopic, not a local, configuration and structure. It suggests the possibility to replace a single ITB layer in the profile with a sequence of smaller steps, as sketched in Fig. 71. The E × B staircase merits further consideration as a regime of enhanced confinement. The structure of the staircase in the presence of sheared mean rotation, flat q, *etc.* is unknown and this question merits further study. Multi-field staircase problems (say in T_e, n, $V_{\rm E}$, *etc.*) also pose important questions. And the study of the staircase has, once again, forced a reconsideration of E × B shear and shear suppression, by reminding us of the role of *vorticity gradients* in regulating turbulence [184].

Stepping back a bit, one must admit that we have only scratched the surface of possible mesoscopic states. The staircase is one possibility, but there is every reason to suspect there are more. Mapping the space of possible states and understanding the selection rules for transitions between them remain tasks for the future.

3. Avalanches and Taylor Relaxation

Nearly all of this review has focused on self-organization by electrostatic mechanisms and its mesoscopic consequences. However, electromagnetic processes can also drive avalanches. A particularly important electromagnetic process is the transport of magnetic helicity, that occurs during Taylor Relaxation.

Taylor Relaxation (TR) is the most fundamental idea in magnetic self-organization [188]. TR is based on the hypothesis that global magnetic helicity is a rugged quantity, as compared to magnetic energy, and so can constrain the relaxation and decay of the latter due to turbulence and resistivity. Viewed as a spectral transport process, TR is closely related to the coexistence of a forward cascade of energy [189] with an inverse cascade [190, 191] of magnetic helicity in 3-D MHD turbulence. Viewed in real space, TR may be viewed as a process of mean field transport of magnetic helicity. In particular, conservation of magnetic helicity implies that the mean EMF associated with TR must have the form $\sim \boldsymbol{\nabla} \cdot \boldsymbol{\Gamma}_{\rm H}$,

where $\mathbf{\Gamma}_{\rm H}$ is the helicity flux. Then, imposing the second requirement that $\mathbf{\Gamma}_{\rm H}$ also dissipate magnetic energy forces $\mathbf{\Gamma}_{\rm H} \sim -\mu \mathbf{\nabla} J_{\|}$, where $J_{\|} = \mathbf{J} \cdot \mathbf{B}/B^2$ and μ is a hyper-resistivity [192]. Thus, TR is linked to a magnetic helicity flux driven by the current gradient.

Of course, this is a minimal mean field model based on a Fickian transport approach. It begs the question of whether the theory can be formulated more generally, in terms of a continuum SOC picture. This is answered in the affirmative in Ref. [193], which applies the joint reflection symmetry principle to the transport of magnetic helicity. A generalized Ohm's law, which includes the effect of mesoscopic current fluctuations, is derived and the type of wave propagation phenomena it supports are analyzed. Super-diffusive helicity pulses – akin to avalanches – are predicted.

As yet, the statistical properties of Taylor Relaxation in a Reversed Field Pinch have not been analyzed. This task is complicated by the fact that the dominant modes in most RFP's are global $m = 1$ tearing modes. Thus, the RFP turbulence does not exhibit so convenient a separation of scales as the tokamak does.

A turbulence spreading process is at work in the RFP, however, and contributes to the homogenization of the parallel current profile, *i.e.* to TR. This process works by interaction of $m = 1$, n modes with a driven mode $m = 0$, $n = 1$, situated at the reversal surface [194]. Scattering of $m = 1$ modes off the $m = 0$ drives the $m = 1$ spectrum to higher n, and thus lower resonant q, and larger radius. In this way the region of $m = 1$ activity expands, as in turbulence spreading! Moreover, this spreading process is crucial to $J_{\|}$ flattening and relaxation. And the nonlinear interactions of neighboring $m = 1$ modes ($m = 1$, n; $m = 1$, $n+1$) drive reconnection at the reversal surface which 'locks in' the kinking-driven reversal of B_T.

This process of spreading of the $m = 1$ excitation region can be treated as a front propagation problem [195]. However, this process is quite different from the others discussed in this paper, since *it drives a local front by the nonlinear scattering of global modes*! It is a prime example of the importance of the dual k-space, real-space character of non-linear dynamics in confined magnetized plasma. And it is also a splendid example that shows that the RFP plasma continues to surprise us and hold our interest [196].

Finally, transport of energetic particles by avalanches is a subject of both scientific and practical importance in MFE. Unfortunately, we ran out of energy to discuss that subject and refer to the progress described in Refs. [172,197–199]

V. CONCLUSIONS

This short review has discussed the physics of turbulence spreading and avalanching in magnetized plasmas. Both are examples of mesoscopic non-linear phenomena, which tend to delocalize and loosen the coupling among:

$$\begin{matrix}\text{fluctuations} \\ \text{and turbulence}\end{matrix} \left\{ \begin{matrix}\text{intensity,} \\ \text{phase}\end{matrix} \right\} \leftrightarrow \text{profiles} \leftrightarrow \text{fluxes},$$

thus necessitating an approach to transport that differs from the traditional quasilinear/Fickian approach. Coming to grips with turbulence spreading and avalanching requires confronting strongly non-Gaussian statistics, again at variance with the traditional quasi-Gaussian view. In this conclusion, we summarize the present understanding of turbulence spreading and avalanching, and their application to MFE phenomenology. A possible unifying synthesis of spreading and avalanching is then proposed, and future research directions are discussed.

Turbulence spreading refers to the entrainment of laminar or low-fluctuation intensity regions by a high intensity region. The prototypical spreading problem is that of determining the evolution of a localized turbulent spot or slug. Turbulence spreading is due to wave emission and propagation, and spatial scattering due to coupling through advective nonlinearity. It is a phenomenon of inhomogeneous turbulence, outside the usual realm of the classic K41 paradigm. The effect of spreading is to decouple the turbulence intensity profile from the spatial profiles of growth and excitation. A mean field phenomenology of spreading has been developed and tested semi-quantitatively. This approach is based on reaction–diffusion equations, with nonlinear (*i.e.* intensity-dependent) diffusion of intensity. An important specific case, here, is that of the Fisher equation with nonlinear diffusion. This formulation leads to the description of spreading as a turbulence intensity front, characterized by its speed and thickness. Not surprisingly, typical spreading speeds scale as $v \sim (\gamma D_{\rm GB})^{1/2}$, where the growth rate γ need not be large, and a gyro-Bohm local diffusivity is assumed. This yields $v \sim v_*$, the characteristic speed of drift wave turbulence. Note that the speed scaling reduces the sensitivity of the front – the nonlinear observable – to the details of the linear growth. $v \sim v_*$ is the maximum speed in drift wave theory and is sufficient for relevance to most fast transients. Other theoretical work has related spreading to turbulence closures via a two-scale Direct Interaction Approximation approach [43].

Avalanches are extended propagating 'transport events', which resemble landslides or bores on the driving profile. Like a bore – the forward face of which is roughened by turbulent breaking while it propagates – turbulence is intrinsic to avalanches, so avalanches also drive turbulence spreading. However, as avalanches are transport events, profile relaxation occurs, also. Avalanches are often described as sequences of, or bursts of, correlated overturning of cells or eddies. Like spreading, which works to relax *envelope* inhomogeneity, we see that avalanching is a multi-scale phenomenon. Essen-

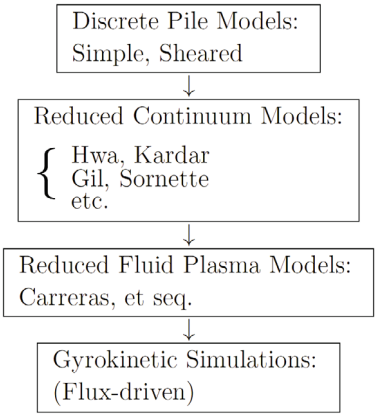

Fig. 72. The range of models that exhibit avalanching.

tial to the notion of 'correlated overturning,' or, 'firing sequences' is a scale separation between the basic cell size and the avalanche size. Of course, the latter must in turn be smaller than the system size. Avalanches are statistical phenomena and are characterized by a broad power law frequency spectrum of flux or overturnings, scaling as $\sim 1/\omega$. Avalanche populations scale inversely with their sizes, following (approximately) Zipf's law, *i.e.* $N_\Delta \sim 1/\Delta$, where Δ is the avalanche size and N_Δ is the population of scale Δ. Of course, avalanches are embedded in the theory of self-organized criticality, as the collective excitations that allow relaxation to the self-organized state. However, avalanches themselves are more general, more relevant and more broadly applicable than is the SOC paradigm.

A wide range of models manifest avalanching. They range from simple sandpiles to sheared sandpiles to simple continuum models, and all the way through the well-known hierarchy of plasma models, up to 3-D toroidal gyrokinetic simulations. This range of models is shown in Fig. 72. In all cases, avalanches are prominent and intrinsic to the relevant case of *flux-driven* evolution, in which the driving profile gradient evolves self-consistently. Artificially or unphysically constraining profile evolution destroys avalanche dynamics. Flux-driven simulations have observed avalanching and the characteristic $1/f$ spectrum of the flux. Blob and void populations were identified and studied. Avalanches were shown to carry a significant part (*i.e.* approaching ∼50%) of the heat flux. Indeed, one result indicated that the largest avalanches dominate the total transport. Avalanching was compared and contrasted to other off-diagonal flux contributions. While the PDF of the driving flux exhibited a power law tail, the off-diagonal flux distribution remained near Gaussian. *Taken together, these studies of avalanching in flux-driven transport strongly call into question local, Fickian formulations of turbulent transport.*

A key issue in avalanching is the character of the transport and how to calculate it. Studies of avalanching systems indicate that the Levy exponent is closer to unity – as for a Cauchy distribution – than to two, as for a Gaussian diffusive process. Moreover, a power law distribution of avalanche sizes $\sim 1/\Delta^{1+\alpha}$, where $\alpha \leq 2$, will not have a finite second moment, thus rendering the standard Fokker–Planck approach to the theory of transport invalid. Methods, such as the theory of Continuous Time Random Walk (CTRW) and Fractional Kinetic (FK) models, rectify this problem at a basic level, but have yet to come to grips with the space–time structure of transport events in realistic systems. Moreover, CTRW and FK calculations require an input step PDF, and as yet we have little intuition concerning the relation of this PDF structure to physical variables. All of these issues point toward the conclusion that prediction and modelling remain a major challenge.

Concepts and theory of turbulence spreading and avalanching have illuminated many difficult problems in magnetic confinement physics. These include but are not limited to:

i) *Non-locality and fast transients*
Fast spreading pulses may explan cold pulse events, and avalanching implies the non-local influence of gradients on flux.

ii) *The shortfall problem and edge-core coupling*
Extending the pioneering intuition of B.B. Kadomtsev, turbulence spreading has been shown to result in inward propagation of turbulence from regions of strongly excitation at the boundary. This process can resolve the 'short-fall problem', *i.e.* the failure of local gyrokinetic simulations to accurately predict turbulence and transport in 'no man's land' - the region between the core (with stiff profiles) and the edge pedestal.

iii) *Gyro-Bohm breaking and scale selection*
Turbulence spreading pulses have been suggested as a means to induce fluctuation and transport non-locality, and explain deviations from local (*i.e.* gyro-Bohm) scaling trends. Likewise, avalanching, with a broad, self-similar scale distribution, will naturally cause breaking of gyro-Bohm scaling. Moreover, absent other physics considerations (such as staircase formation), an avalanche ensemble will *not* be amenable to characterization by the familiar intellectual crutch ($\Delta \sim (\rho_i L_\perp)^{1/2}$) for dealing with mesoscales. More generally, bursty avalanching is a natural way to address the apparent intermittency of plasma turbulence.

iv) *Transport in 3-D systems, with magnetic islands*
Recent experiments strongly suggest that turbulence spreading can invade and redistribute turbulence energy in regions with magnetic islands. This is of great potential importance to the physics of 3-D systems and NTM evolution.

Two frequently asked questions about spreading and avalanching are:

i) What, exactly, is the difference between turbulence spreading and avalanching?

ii) What, exactly, is an avalanche?

These two questions have been answered to the best of our current understanding in this paper. However, these questions trigger two more questions:

i) Is there a *simple* model within which to synthesize the two physical processes? What are the consequences of their interaction?

ii) How would one construct a *systematic theory* of the two, starting from the gyrokinetic equation?

Here, we outline answers to this second pair of questions.

Regarding a synthesis, the most straightforward approach is to introduce spreading into the Gil–Sornette model discussed in Sec. III.1. Recall that in the Gil–Sornette model, an activity or fluctuation intensity field S is evolved along with an occupation or density field h. Thus, one could envision an extension of the form:

$$
\begin{aligned}
&(a) \quad \frac{\partial S}{\partial t} = \chi\left\{\mu S + \beta S^3 - S^5\right\} - \partial_x \Gamma_S \\
&(b) \quad \Gamma_S = f(S, \partial S/\partial x) \\
&i.e. \qquad = -D_E S \frac{\partial S}{\partial x} \\
&(c) \quad \frac{\partial h}{\partial t} = -\frac{\partial}{\partial x} F\left(S, \frac{\partial h}{\partial x}\right) + \Phi \\
&(d) \quad F\left(S, \frac{\partial h}{\partial x}\right) = -\alpha S^2 \frac{\partial h}{\partial x} - D_0 \frac{\partial h}{\partial x}
\end{aligned}
$$

Here, D_0 accounts for background diffusion, representative of collisional transport. Spreading enters via the $-\partial_x \Gamma_S$ contribution to $\partial_t S$, with $\Gamma_S = -D_E S \partial_x S$ or some other nonlinear function of S. D_E is the eddy diffusivity constant for turbulence scattering. Γ_S need not be local. Clearly, a very imporant parameter of this extended model is the effective Prandtl number α/D_E, which describes the ratio of spreading to transport. The extended Gil–Sornette model (EGSM) supports both spreading (direct spatial coupling of excitation) as well as avalanching (coupling of excitation through the profile). One can hypothesize that an effect of spreading will be to smooth profiles, much like collisional diffusion does. Given that usually $D_E \gg D_0$, this effect will be significant. Moreover, spreading can induce local oscillator firing directly, without profile coupling. It seems unlikely that spreading will alter the large avalanches, *i.e.* those with scale $l > l_s$, where l_s is the 'spreading length', set by Γ_S. However, mesoscale and barrier dynamics will likely change. Future investigation of the EGSM promises to be interesting.

A rigorous theory of avalanching that begins from gyrokinetics is challenging. A promising road forward might be to study the combined evolution of the mean distribution function $\langle f \rangle$ by quasi-linear or other similar methods, together with the evolution of the phase space density fluctuation intensity evolution $\langle \delta f^2 \rangle$. The latter, of course, determines the phase space fluxes (*i.e.* $\langle \tilde{v}_r \delta f \rangle$) via quasi-neutrality, *etc.* Note here that $\langle \delta f^2 \rangle$ is the intensity, *not* the two-point correlator $\langle \delta f(1) \delta f(2) \rangle$. Thus, we are concerned with evolution of the pair centroid, not the relative phase space position. Hence $\langle \delta f^2 \rangle$ evolves via nonlinear diffusion but *not* relative diffusion. The phase space intensity scattering will naturally couple mean field relaxation over a range of the spreading length l_s, thus leading to "correlated overturning" and avalanching. In this approach, the 'correlation' in 'correlated overturning' is induced by spreading as well as by profile evolution. For a complete theory, it should be possible, though challenging, to combine the intensity $\langle \delta f^2 \rangle$ evolution for mesoscales with the correlation function $\langle \delta f(1) \delta f(2) \rangle$ evolution for microscales and phase space density granulations. This would evolve both the amplitude and shape of the correlation function.

Future works on spreading and avalanching promise to be numerous and interesting. In addition to extensions of applications to fusion phenomenology and the theoretical work discussed above, several issues stand out. These include:

i) How can we get a sense of the flux PDF, and its dependence on physical parameters? This is essential to the use of CTRW and FK approaches to actually predict transport.

ii) How does turbulence spreading behave in a bistable system? Recent experiments have indicated the presence of 'global hysteresis' in core transport (*i.e.* without an ITB). This is suggestive of bistability, which will have implications for spreading [42].

iii) How can we build a model of turbulence and transport as an ensemble of interacting fronts, rather than weakly interacting linear waves, as in quasi-linear theory? A front seems to be a more appropriate way to envision a dissipative, localized nonlinear excitation than does a 'wave'.

iv) How do we self-consistently treat zonal flow effects on spreading and avalanches? The E × B staircase is one such paradigm, where – much like a spinodal decomposition – the system solves the problem of coexistence by separation into domains or phases of avalanching and turbulence (staircase steps) kept apart by profile corrugations and shear layers (*i.e.* staircase jumps). The E × B staircase is one solution to the coexistence problem. What is the broader picture?

v) How do resonant particles modify spreading and avalanching? This is especially interesting for resonant interactions with Kubo number $\to 1$. Do energetic particle avalanches have unique physics?

vi) How does phase dynamics and evolution enter and affect avalanching and spreading? Do local domains of phase correlated modes fire during an avalanche?

Many more possibilities exist. There is little doubt that the study of mesoscopic transport events will continue be at the center of the action in MFE theory, because these events and processes ultimately select the scales for anomalous transport.

ACKNOWLEDGMENTS

We would like to acknowledge useful discussions with A. Ashourvan, S. Cappello, B. A. Carreras, L. Chen, M. J. Choi, B. Compernolle, P. Davidson, G. Dif-Pradalier, X. T. Ding, X. Fan, X. Garbet, N. Goldenfeld, D. Guo, W. X. Guo, Z. B. Guo, O. D. Gurcan, R. Hajjar, R. Heinonen, P. Hennequin, C. Hidalgo, R. Hong, D. W. Hughes, T. Hwa, K. Ida, S. Inagaki, K. Itoh, S-I. Itoh, H. G. Jhang, R. Ke, S. Keating, E-J. Kim, S. S. Kim, Y. Kosuga, S. Ku, J. M. Kwon, J. C. Li, Z. Lin, T. Long, R. Ma, V. Naulin, D. E. Newman, Y. Pomeau, T. Rhee, Y. Sarazin, B. D. Scott, Z. B. Shi, H. J. Sun, R. D. Sydora, K. Thompson, L. Villard, L. Wang, W. X. Wang, Z. H. Wang, W. Xiao, Y. Xu, M. Yagi, W. R. Young, S. Yi, Y. Zhang and F. Zonca. We have also benefitted from the Festival de Theorie 2003, 2005 and 2017 where many of the subjects addressed in this review were discussed. We would also like to thank Mr. G. J. Choi for his dedicated work in preparing this manuscript.

This work was supported by the Ministry of Science, ICT and Future Planning of the Republic of Korea under the Korean ITER project contract, and National R&D Program through the National Research Foundation of Korea (NRF) funded by the Ministry of Science, ICT & Future Planning (No. 2014M1A7A1A03045368), by the U.S. Department of Energy, Office of Science, Office of Fusion Energy Sciences under Award Number DE-FG02-04ER54738, and by the Center for Fusion Science, Southwest Institute of Physics, China. PD thanks SWIP for hospitality during the completion of a portion of this work.

REFERENCES

[1] F. Wagner *et al.*, Phys. Rev. Lett. **49**, 1408 (1982).
[2] P. A. Davidson, J. Turb. **1**, N6 (2000).
[3] P. H. Diamond, S-I. Itoh, K. Itoh and T. S. Hahm, Plasma Phys. Control. Fusion **47**, R35 (2005).
[4] Z. B. Guo *et al.*, submitted (2018).
[5] G. I. Barenblatt, *Similarity, Self-similarity, and Intermediate Asymptotics* (New York and London: Consultant Bureau, 1979).
[6] L. G. Loitsyansky, Centr. Aero. Hydrodyn. Inst. Moscow, Rep. no. **440**(Trans. NACA Tech. Memo. 1079) (1939).
[7] L. D. Landau and E. M. Lifshitz, *Fluid Mechanics*, 1st ed. (Oxford: Pergamon, 1959), p. 141.
[8] Y. Pomeau, Phys. D: Nonlinear Phenom. **23**, 3 (1986).
[9] Y. Pomeau, C. R. Mecanique **343**, 210 (2015).
[10] G. B. Whitham, *Linear and Nonlinear Waves* (Wiley-Interscience, New York, 1999).
[11] S. M. Kaye *et al.*, Nucl. Fusion **47**, 499 (2007).
[12] R. Nazikian, K. Shinohara, G. J. Kramer, E. Valeo, K. Hill, T. S. Hahm, G. Rewoldt, S. Ide, Y. Koide, Y. Oyama, H. Shirai and W. Tang, Phys. Rev. Lett. **94**, 135002 (2005).
[13] X. Garbet, L. Laurent, A. Samain and J. Chinardet, Nucl. Fusion **34**, 963 (1994).
[14] T. S. Hahm, P. H. Diamond, Z. Lin, K. Itoh and S-I. Itoh, Plasma Phys. Control. Fusion **46**, A323 (2004).
[15] E-J. Kim, P. H. Diamond, M. Malkov, T. S. Hahm, K. Itoh, S-I. Itoh, S. Champeaux, I. Gruzinov, O. Gurcan, C. Holland, M. N. Rosenbluth and A. Smolyakov, Nucl. Fusion **43**, 961 (2003).
[16] O. Gurcan, P. H. Diamond, T. S. Hahm and Z. Lin, Phys. Plasmas **12**, 032303 (2005).
[17] H. Sugama and M. Wakatani, J. Phys. Soc. Jpn. **61**, 3166 (1992).
[18] P. H. Diamond, V. B. Lebedev, D. E. Newman, B. A. Carreras, T. S. Hahm, W. M. Tang, G. Rewoldt and K. Avinash, Phys. Rev. Lett. **78**, 1472 (1997).
[19] D. E. Newman, B. A. Carreras, D. Lopez-Bruna, P. H. Diamond and V. B. Lebedev, Phys. Plasmas **5**, 938 (1998).
[20] M. A. Malkov, P. H. Diamond and M. N. Rosenbluth, Phys. Plasmas **8**, 5073 (2001).
[21] D. del-Castillo-Negrete, Phys. Plasmas **13**, 082308 (2006).
[22] T. S. Hahm, P. H. Diamond, Z. Lin, G. Rewoldt, O. Gurcan and S. Ethier, Phys. Plasmas **12**, 090903 (2005).
[23] H. P. Furth, J. Kileen and M. N. Rosenbluth, Phys. Fluids **6**, 459 (1963).
[24] R. D. Sydora, V. K. Decyk and J. M. Dawson, Plasma Phys. Control. Fusion **38**, A281 (1996).
[25] Z. Lin, S. Ethier, T. S. Hahm and W. M. Tang, Phys. Rev. Lett. **88**, 195004 (2002).
[26] V. B. Lebedev and P. H. Diamond, Phys. Plasmas **4**, 1087 (1997).
[27] S-I. Itoh and K. Itoh, J. Phys. Soc. Japan **69**, 408 (2000).
[28] Y. Sarazin, X. Garbet, Ph. Ghendrih and S. Benkadda, Phys. Plasmas **7**, 1085 (2000).
[29] X. Garbet, Y. Sarazin, F. Imbeaux, P. Ghendrih, C. Bourdelle, O. D. Gurcan and P. H. Diamond, Phys. Plasmas **14**, 122305 (2007).
[30] L. Villard, S. J. Allfrey, A. Bottino, M. Brunetti, G. L. Falchetto, V. Grandgirard, R. Hatzky, J. Nuhrenberg, A. G. Peeters, O. Sauter, S. Sorge and J. Vaclavik, Nucl. Fusion **44**, 172 (2004).
[31] L. Chen, R. B. White and F. Zonca, Phys. Rev. Lett. **92**, 075004 (2004).
[32] L. Chen, Z. Lin and R. B. White, Phys. Plasmas **7**, 3129 (2000).
[33] X. Garbet, private communication (2002).

[34] B. B. Kadomtsev, *Plasma Turbulence* (Academic, New York, 1965).
[35] R. A. Fisher, Ann. Eugenics **7**, 353 (1937).
[36] A. Kolmogoroff, I. Petrovsky and N. Piscounoff, Clin. Cancer Res. **1**, 1 (1937).
[37] V. Naulin, A. H. Nielsen and J. Juul Rasmussen, Phys. Plasmas **12**, 122306 (2005).
[38] J. Juul Rasmussen, V. Naulin, P. Mantica, J. S. Lonnroth, V. Parail and JET-EFDA Contributors, in *Proceedings of the 33rd EPS Conference on Plasma Physics*, (Rome, 19-23 June 2006 ECA), Vol. 301, p. 1076.
[39] Z. H. Wang, P. H. Diamond, O. D. Gurcan, X. Garbet and X. G. Wang, Nucl. Fusion **51**, 073009 (2011).
[40] Z. B. Guo and P. H. Diamond, Phys. Plasmas **24**, 100705 (2017).
[41] S. Inagaki *et al.* and the LHD Experiment Group, Nucl. Fusion **53**, 113006 (2013).
[42] R. Heinonen and P. H. Diamond, submitted (2018).
[43] O. D. Gurcan, P. H. Diamond and T. S. Hahm, Phys. Plasmas **13**, 052306 (2006).
[44] R. V. Budny *et al.*, Phys. Plasmas **7**, 5038 (2000).
[45] G. R. McKee *et al.*, Nucl. Fusion **41**, 1235 (2001).
[46] P. Hennequin, R. Sabot, C. Honore, G. T. Hoang, X. Garbet, A. Truc, C. Fenzi and A. Quemeneur, Plasma Phys. Control. Fusion **46**, B121 (2004).
[47] Z. Lin, T. S. Hahm, W. W. Lee, W. M. Tang and R. B. White, Science **281**, 1835 (1998).
[48] X. Garbet, Y. Idomura, L. Villard and T. H. Watanabe, Nucl. Fusion **50**, 043002 (2010).
[49] E. A. Frieman and L. Chen, Phys. Fluids **25**, 502 (1982).
[50] T. S. Hahm, Phys. Fluids **31**, 2670 (1988).
[51] S. E. Parker, H. E. Mynick, M. Artun, J. C. Cummings, V. Decyk, J. V. Kepner, W. W. Lee and W. M. Tang, Phys. Plasmas **3**, 1959 (1996).
[52] Y. Kishimoto, T. Tajima, W. Horton, M. J. LeBrun and J. Y. Kim, Phys. Plasmas **3**, 1289 (1996).
[53] W. W. Lee and R. Santoro, Phys. Plasmas **4**, 169 (1997).
[54] Y. Idomura, M. Wakatani and S. Tokuda, Phys. Plasmas **7**, 3551 (2000).
[55] Z. Lin and T. S. Hahm, Phys. Plasmas **11**, 1099 (2004).
[56] A. M. Dimits *et al.*, Phys. Plasmas **7**, 969 (2000).
[57] B. F. McMillan, X. Lapillonne, S. Brunner, L. Villard, S. Jolliet, A. Bottino, T. Gorler and F. Jenko, Phys. Rev. Lett. **105**, 155001 (2010).
[58] S. Jolliet, A. Bottino, P. Angelino, R. Hatzky, T. M. Tran, B. F. McMillan, O. Sauter, K. Appert, Y. Idomura and L. Villard, Comp. Phys. Comm. **177**, 409 (2007).
[59] T. Gorler, Ph. D. Thesis, Universitat Ulm, 2009.
[60] J. Candy and R. E. Waltz, J. Comput. Phys. **186**, 545 (2003).
[61] M. Kotschenreuther, G. Rewoldt and W.M. Tang, Comput. Phys. Commun. **88**, 128 (1995).
[62] J. Candy, R. E. Waltz and W. Dorland, Phys. Plasmas **11**, L25 (2004).
[63] Z. Lin, S. Ethier, T. S. Hahm and W. M. Tang, Plasma Sci. Technol. **14**, 1125 (2012).
[64] R. E. Waltz and J. Candy, Phys. Plasmas **12**, 072303 (2005).
[65] J. M. Kwon, S. Yi, T. Rhee, P. H. Diamond, K. Miki, T. S. Hahm, J. Y. Kim, O. D. Gurcan and C. McDevitt, Nucl. Fusion **52**, 013004 (2012).
[66] S. Yi, J. M. Kwon, P. H. Diamond and T. S. Hahm, Phys. Plasmas **21**, 092509 (2014).
[67] S. Yi, J. M. Kwon, P. H. Diamond and T. S. Hahm, Nucl. Fusion **55**, 092002 (2015).
[68] P. Mantica *et al.*, Phys. Rev. Lett. **107**, 135004 (2011).
[69] J. W. Hughes, D. A. Mossessian, A. E. Hubbard, B. LaBombard and E. S. Marmar, Phys. Plasmas **9**, 3019 (2002).
[70] J. G. Cordey *et al.*, Plasma Phys. Control. Fusion **36**, A267 (1994).
[71] S. V. Neudatchin, T. Takizuka, H. Shirai, T. Fujita, A. Isayama, Y. Kamada, Y. Koide, T. Suzuki and S. Takeji, Plasma Phys. Control. Fusion **44**, A383 (2002).
[72] B. B. Kadomtsev, Plasma Phys. Control. Fusion **34**, 1931 (1992).
[73] Z. Lin, T. S. Hahm, W. W. Lee, W. M. Tang and P. H. Diamond, Phys. Rev. Lett. **83**, 3645 (1999).
[74] B. LaBombard *et al.* and the Alcator Group, Nucl. Fusion **44**, 1047 (2004).
[75] G. Rewoldt and W. M. Tang, Phys. Fluids B **2**, 318 (1990).
[76] K. H. Burrell, Phys. Plasmas **4**, 1499 (1997).
[77] W. X. Wang, T. S. Hahm, W. W. Lee, G. Rewoldt, J. Manickam and W. M. Tang, Phys. Plasmas **14**, 072306 (2007).
[78] T. S. Hahm and K. H. Burrell, Phys. Plasmas **2**, 1648 (1995).
[79] M. Yagi, T. Ueda, S-I. Itoh, M. Azumi, K. Itoh, P. H. Diamond and T. S. Hahm, Plasma Phys. Control. Fusion **48**, A409 (2006).
[80] W. Deng and Z. Lin, Phys. Plasmas **16**, 102503 (2009).
[81] C. H. Ma, X. Q. Xu, P. W. Xi and T. Y. Xia, Phys. Plasmas **22**, 010702 (2015).
[82] A. Ishizawa and N. Nakajima, Phys. Plasmas **14**, 040702 (2007).
[83] A. Ishizawa and N. Nakajima, Nucl. Fusion **49**, 055015 (2009).
[84] E. Poli, A. Bottino and A. G. Peeters, Nucl. Fusion **49**, 075010 (2009).
[85] E. Poli, A. Bottino, W. A. Hornsby, A. G. Peeters, T. Ribeiro, B. D. Scott and M. Siccinio, Plasma Phys. Control. Fusion **52**, 124021 (2010).
[86] K. Ida *et al.* and LHD Experimental Group, Phys. Rev. Lett. **88**, 015002 (2001).
[87] M. J. Choi, J. Kim, J-M. Kwon, H. K. Park, Y. In, W. Lee, K. D. Lee, G. S. Yun, J. Lee, M. Kim, W-H. Ko, J. H. Lee, Y. S. Park, Y-S. Na, N. C. Luhmann Jr. and B. H. Park, Nucl. Fusion **57**, 126058 (2017).
[88] K. Ida, T. Kobayashi, M. Ono, T. E. Evans, G. R. McKee and M. E. Austin, Phys. Rev. Lett. **120**, 245001 (2018).
[89] M. Jiang, Y. Xu, W. Chen, X. T. Ding, Z. B. Shi, W. L. Zhong, X. Q. Ji, P. W. Shi, J. Q. Li, Z. C. Yang, B. S. Yuan, Y. Liu, Q. W. Yang, M. Xu and HL-2A team, submitted to Phys. Rev. Lett. (2018).
[90] E. J. Synakowski *et al.*, Nucl. Fusion **39**, 1733 (1999).
[91] E. Mazzucato *et al.*, Phys. Rev. Lett. **77**, 3145 (1996).
[92] G. R. McKee, R. J. Fonck, D. K. Gupta, D. J. Schlossberg, M. W. Shafer, R. L. Boivin, W. Solomon, Plasma Fusion Res. **2**, S1025 (2007).
[93] T. Estrada, C. Hidalgo and T. Happel, Nucl. Fusion **51**,

032001 (2011).
[94] P.H. Diamond *et al., presented in 6th Asia-Pacific Transport Working Group Meeting* (Seoul, Korea, 2016)
[95] G. K. Zipf, *Human Behavior and the Principle of Least Effort* (Cambridge, Massachusetts: Addison-Wesley, 1949).
[96] H. E. Hurst, Trans. Am. Soc. Civil Eng. **116**, 770 (1951).
[97] H. E. Hurst, Proc. Inst. ivil Eng., Part 1, 519 (1956).
[98] H. E. Hurst, R. P. Black and Y. M. Simaika, *Long-Term Storage, and Experimental Study* (London, Constable, 1965).
[99] B. B. Mandelbrot, *The Fractal Geometry of Nature*, (Freeman, New York, 1983).
[100] P. Bak, C. Tang and K. Wiesenfeld, Phys. Rev. Lett. **59**, 381 (1987).
[101] P.H. Diamond *et al., presented in 9th Festival de Theorie* (Aix-en-Provence, France, 2017)
[102] B. B. Mandelbrot and J. R. Wallis, Water Resources Res. **4**, 909 (1968).
[103] G. Boffetta, A. Mazzino and A. Vulpiani, J. Phys. A **41**, 363001 (2008)
[104] E. W. Montroll and G. H. Weiss, J. Math. Phys. **6**, 167 (1965).
[105] L. P. Kadanoff, S. R. Nagel, L. Wu and S. Zhou, Phys. Rev. A **39**, 6524 (1989).
[106] D. E. Newman, B. A. Carreras, P. H. Diamond and T. S. Hahm, Phys. Plasmas **3**, 1858 (1996).
[107] I. Gruzinov, P. H. Diamond and M. N. Rosenbluth, Phys. Rev. Lett. **89**, 255001 (2002).
[108] I. Gruzinov, P. H. Diamond and M. N. Rosenbluth, Phys. Plasmas **10**, 569 (2003).
[109] T. Hwa and M. Kardar, Phys. Rev. A **45**, 7002 (1992).
[110] P. H. Diamond and T. S. Hahm, Phys. Plasmas **2**, 3640 (1995).
[111] D. Shvarts, U. Alon, D. Ofer, R. L. McCrory and C. P. Verdon, Phys. Plasmas **2**, 2465 (1995).
[112] S. Chandrasekhar, Rev. Mod. Phys. **15**, 1 (1943).
[113] Y. Kosuga, P. H. Diamond, G. Dif-Pradalier and O. D. Gurcan, Phys. Plasmas **21**, 055701 (2014).
[114] Y. Kosuga, P. H. Diamond and O. D. Gurcan, Phys. Rev. Lett. **110**, 105002 (2013).
[115] L. Gil and D. Sornette, Phys. Rev. Lett. **76**, 3991 (1996).
[116] K. Barada, T. L. Rhodes, K. H. Burrell, L. Zeng, L. Bardoczi, Xi Chen, C. M. Muscatello and W. A. Peebles, Phys. Rev. Lett. **120**, 135002 (2018).
[117] V. B. Lebedev and P. H. Diamond, Phys. Plasmas **4**, 1087 (1997).
[118] T. Rhee, J. M. Kwon, P. H. Diamond and W. W. Xiao, Phys. Plasmas **19**, 022505 (2012).
[119] B. A. Carreras, D. Newman, E. Lynch and P. H. Diamond, Phys. Plasmas **3**, 2903 (1996).
[120] X. Garbet and R. E. Waltz, Phys. Plasmas **5**, 2836 (1998).
[121] X. Garbet, Y. Sarazin, P. Beyer, P. Ghendrih, R. E. Waltz, M. Ottaviani and S. Benkadda, Nucl. Fusion **39**, 2063 (1999).
[122] Y. Sarazin and Ph. Ghendrih, Phys. Plasmas **5**, 4214 (1998).
[123] P. Beyer, S. Benkadda, X. Garbet and P. H. Diamond, Phys. Rev. Lett. **85**, 4892 (2000).
[124] E-J. Kim and P. H. Diamond, Phys. Rev. Lett. **22**, 225002 (2002).
[125] L. Dan, Private Communications (2000).
[126] Y. Idomura, H. Urano, N. Aiba and S. Tokuda, Nucl. Fusion **49**, 065029 (2009).
[127] V. Grandgirard *et al.*, Plasma Phys. Control. Fusion **49**, B173 (2007).
[128] J. A. Heikkinen, S. J. Janhunen, T. P. Kiviniemi and F. Ogando, J. Comp. Phys. **227**, 5582 (2008).
[129] C. S. Chang, S. Ku, P. H. Diamond, Z. Lin, S. Parker, T. S. Hahm and N. Samatova, Phys. Plasmas **16**, 056108 (2009).
[130] Y. Sarazin *et al.*, Nucl. Fusion **51**, 103023 (2011).
[131] Y. Sarazin, V. Grandgirard, J. Abiteboul, S. Allfrey, X. Garbet, Ph. Ghendrih, G. Latu, A. Strugarek and G. Dif-Pradalier, Nucl. Fusion **50**, 054004 (2010).
[132] E. Mazzucato and R. Nazikian, Phys. Rev. Lett. **71**, 1840 (1993).
[133] R. J. Fonck, G. Cosby, R. D. Durst, S. F. Paul, N. Bretz, S. Scott, E. Synakowski and G. Taylor, Phys. Rev. Lett. **70**, 3736 (1993).
[134] P. Hennequin *et al.* and the ASDEX Upgrade Team, in *42nd EPS Conference on Plasma Physics, I1* (2015), p. 102.
[135] G. Dif-Pradalier, G. Hornung, X. Garbet, Ph. Ghendrih, V. Grandgirard, G. Latu and Y. Sarazin, Nucl. Fusion **57**, 066026 (2017).
[136] Y. Xiao and Z. Lin, Phys. Rev. Lett. **103**, 085004 (2009).
[137] L. Qi, J. M. Kwon, T. S. Hahm and S. Yi, Nucl. Fusion **57**, 124002 (2017).
[138] S. Ku *et al.*, Nucl. Fusion **52**, 063013 (2012).
[139] P. H. Diamond, C. J. McDevitt, O. D. Gurcan, T. S. Hahm and V. Naulin, Phys. Plasmas **15**, 012303 (2008).
[140] P. H. Diamond, C. J. McDevitt, O. D. Gurcan, T. S. Hahm, W. X. Wang, E. S. Yoon, I. Holod, Z. Lin, V. Naulin and R. Singh, Nucl. Fusion **49**, 045002 (2009).
[141] O. D. Gurcan, P. H. Diamond and T. S. Hahm, Phys. Plasmas **14**, 055902 (2007).
[142] Y. Kosuga, P. H. Diamond and O. D. Gurcan, Phys. Plasmas **17**, 102313 (2010).
[143] J. E. Rice *et al.*, Phys. Rev. Lett. **106**, 215001 (2011).
[144] W. M. Solomon *et al.*, Phys. Plasmas **17**, 056108 (2010).
[145] F. Hariri, V. Naulin, J. Juul Rasmussen, G. S. Xu and N. Yan, Phys. Plasmas **23**, 052512 (2016).
[146] M. Kikuchi and M. Azumi, Rev. Mod. Phys. **84**, 1807 (2012).
[147] K. Imadera, J. Q. Li and Y. Kishimoto, in *Proc. 25th Int. Conf. on Fusion Energy* (2016), p. TH/P3-3.
[148] Y. Kishimoto, K. Imadera and W. Wang, Private Communications (2017)
[149] W. Wang, Y. Kishimoto and K. Imadera, Private Communications (to be submitted).
[150] K. Ida *et al.*, Nucl. Fusion **55**, 013022 (2015).
[151] B. A. Carreras *et al.*, Phys. Plasmas **5**, 3632 (1998).
[152] P. A. Politzer, Phys. Rev. Lett **84**, 1192 (2000).
[153] P. A. Politzer, M. E. Austin, M. Gilmore, G. R. McKee, T. L. Rhodes, C. X. Yu, E. J. Doyle, T. E. Evans and R. A. Moyere, Phys. Plasmas **9**, 1962 (2002).
[154] M. J. Choi, M. H. Woo, Jae-Min Kwon, S. Ko, Hogun Jhang, H. K. Park, T. S. Hahm, J. Lee, M. Kim, G. S. Yun, arXiv:1806.04947v2 (2018).
[155] S. J. Zweben *et al.*, Phys. Plasmas **9**, 1981 (2002).
[156] J. A. Boedo *et al.*, Phys. Plasmas **10**, 1670 (2003).

[157] S. J. Zweben *et al.* and the NSTX Team, Nucl. Fusion **44**, 134 (2004).
[158] J. A. Boedo *et al.* and NSTX Team, Phys. Plasmas **21**, 042309 (2014).
[159] Y. H. Xu, S. Jachmich, R. R. Weynants, A. Huber, B. Unterberg and U. Samm, Phys. Plasmas **11**, 5413 (2004).
[160] B. D. Scott, Contrib. Plasma Phys. **46**, 714 (2006).
[161] P. Manz, T. T. Ribeiro, B. D. Scott, G. Birkenmeier, D. Carralero, G. Fuchert, S. H. Muller, H. W. Muller, U. Stroth and E. Wolfrum, Phys. Plasmas **22**, 022308 (2015).
[162] B. D. Scott, Phys. Plasmas **12**, 082305 (2005).
[163] K. W. Gentle, R. V. Bravenec, G. Cima, H. Gasquet, G. A. Hallock, P. E. Phillips, D. W. Ross, W. L. Rowan, A. J. Wootton, T. P. Crowley, J. Heard, A. Ouroua, P. M. Schoch and C. Watts, Phys. Plasmas **2**, 2292 (1995).
[164] K. W. Gentle, W. L. Rowan, R. V. Bravenec, G. Cima, T. P. Crowley, H. Gasquet, G. A. Hallock, J. Heard, A. Ouroua, P. E. Phillips, D. W. Ross, P. M. Schoch and C. Watts, Phys. Rev. Lett. **74**, 3620 (1995).
[165] J. D. Callen and M. W. Kissick, Plasma Phys. Control. Fusion **39**, B173 (1997).
[166] B. P. van Milligen *et al.*, Nucl. Fusion **42**, 787 (2002).
[167] P. Mantica *et al.* and JET EFDA Contributors, in *Proceedings of the 19th International Conference on Fusion Energy, Lyon, 2002* (IAEA, Vienna, 2002), p. EX/P1-04.
[168] B. Van Compernolle, G. J. Morales, J. E. Maggs and R. D. Sydora, Phys. Rev. E **91**, 031102 (2015).
[169] G. Dif-Pradalier, P. H. Diamond, V. Grandgirard, Y. Sarazin, J. Abiteboul, X. Garbet, Ph. Ghendrih, A. Strugarek, S. Ku and C. S. Chang, Phys. Rev. E **82**, 025401(R) (2010).
[170] G. M. Zaslavsky, *Hamiltonian Chaos and Fractal Dynamics* (Oxford University Press, 2005).
[171] T. H. Solomon, E. R. Weeks and H. L. Swinney, Phys. Rev. Lett. **71**, 3975 (1993).
[172] G. M. Zaslavsky, M. Edelman, H. Weitzner, B. Carreras, G. McKee, R. Bravenec and R. Fonck, Phys. Plasmas **7**, 3691 (2000).
[173] G. K. Vallis, *Atmospheric and Oceanic Fluid Dynamics* (Cambridge University Press, 2006).
[174] G. K. Batchelor, H. K. Moffatt and M. G. Worster, *Perspectives in Fluid Dynamics* (Cambridge University Press, 2002).
[175] R. B. Wood and M. E. McIntyre, J. Atmospheric Sci. **67**, 1261 (2010).
[176] O. D. Gurcan and P. H. Diamond, J. Phys. A **48**, 293001 (2015).
[177] G. I. Taylor, Philos. Trans. Royal Soc. A **215**, 1 (1915).
[178] D. G. Dritschel and M. E. McIntyre, J. Atmospheric Sci. **65**, 855 (2008).
[179] G. Dif-Pradalier *et al.*, Phys. Rev. Lett. **114**, 085004 (2015).
[180] N. J. Balmforth, S. G. L. Smith and W. R. Young, J. Fluid Mech. **355**, 329 (1998).
[181] A. Ashourvan and P. H. Diamond, Phys. Rev. E **94**, 051202(R) (2016).
[182] A. Ashourvan and P. H. Diamond, Phys. Plasmas **24**, 012305 (2017).
[183] P. B. Rhines, J. Fluid Mech. **69**, 417 (1975).
[184] W. X. Guo *et al.*, *presented in 8th Asia-Pacific Transport Working Group Meeting* (Leshan, China, 2018).
[185] G. Dif-Pradalier *et al.*, *presented in 8th Asia-Pacific Transport Working Group Meeting* (Leshan, China, 2018).
[186] O. D. Gurcan, P. H. Diamond, X. Garbet, V. Berionni, G. Dif-Pradalier, P. Hennequin, P. Morel, Y. Kosuga and L. Vermare, Phys. Plasmas **20**, 022307 (2013).
[187] M. R. Flynn, A. R. Kasimov, J. C. Nave, R. R. Rosales and B. Seibold, Phys. Rev. E **79**, 056113 (2009).
[188] J. B. Taylor, Rev. Mod. Phys. **58**, 741 (1986).
[189] S. Galtier, *Introduction to Modern Magnetohydrodynamics* (Cambridge University Press, 2016).
[190] U. Frisch, M. Lesieur and P. L. Sulem, Phys. Rev. Lett. **37**, 895 (1976).
[191] A. Pouquet, U. Frisch and J. Leorat, J. Fluid Mech. **77**, 321 (1976).
[192] A. H. Boozer, J. Plasma Phys. **35**, 133 (1986).
[193] P. H. Diamond and M. Malkov, Phys. Plasmas **10**, 2322 (2003).
[194] J. A. Holmes, B. A. Carreras, P. H. Diamond and V. E. Lynch, Phys. Fluids **31**, 1166 (1988).
[195] I. H. Hutchinson, M. Malacarne, P. Noonan and D. Brotherton-Ratcliffe, Nucl. Fusion **24**, 59 (1984).
[196] R. Lorenzini *et al.* and RFX-mod team and collaborators, Nat. Phys. **5**, 570 (2009).
[197] F. Zonca, S. Briguglio, L. Chen, G. Fogaccia, T. S. Hahm, A. V. Milovanov and G. Vlad, Plasma Phys. Control. Fusion **48**, B15 (2006).
[198] Z. Guo, L. Chen and F. Zonca, Phys. Rev. Lett. **103**, 055002 (2009).
[199] F. Zonca, L. Chen, S. Briguglio, G. Fogaccia, A. V. Milovanov, Z Qiu, G. Vlad and X. Wang, Plasma Phys. Control. Fusion **57**, 014024 (2015).